Rare events in many-body systems: reactive paths and reaction constants for structural transitions

Massimiliano Picciani

▶ **To cite this version:**

Massimiliano Picciani. Rare events in many-body systems: reactive paths and reaction constants for structural transitions. Statistical Mechanics [cond-mat.stat-mech]. Université Pierre et Marie Curie - Paris VI, 2012. English. NNT : . tel-00706510

HAL Id: tel-00706510

https://theses.hal.science/tel-00706510

Submitted on 10 Jun 2012

HAL is a multi-disciplinary open access archive for the deposit and dissemination of scientific research documents, whether they are published or not. The documents may come from teaching and research institutions in France or abroad, or from public or private research centers.

L'archive ouverte pluridisciplinaire **HAL**, est destinée au dépôt et à la diffusion de documents scientifiques de niveau recherche, publiés ou non, émanant des établissements d'enseignement et de recherche français ou étrangers, des laboratoires publics ou privés.

POLITECNICO DI MILANO
UNIVERSITÉ PARIS VI - PIERRE ET MARIE CURIE

DOTTORATO IN SCIENZA E TECNOLOGIE DELLE RADIAZIONI
ECOLE DOCTORALE DE PHYSIQUE DE LA RÉGION PARISIENNE

P H D T H E S I S

Massimiliano Picciani

Rare events in many-body systems: reactive paths and reaction constants for structural transitions

prepared at CEA Saclay
Service de Recherches en Métallurgie Physique
defended on January 30, 2012

Jury :

Reviewers :	Jean-Louis Barrat	-	Université Joseph Fourier - Grenoble
	Florent Calvo	-	Université Claude Bernard - Lyon 1
Examinator :	Rodolphe Vuilleumier	-	ENS Paris
Examinator :	Frédéric van Wijland	-	Université Denis Diderot - Paris VII
PhD Advisors:	Jorge Kurchan	-	ESPCI
PhD Advisor:	Roberto Piazza	-	Politecnico di Milano
CEA Supervisor:	Manuel Athenes	-	CEA Saclay

Contents

1 Introduction **1**

2 Transition current sampling **7**

2.1 Probability currents and reaction paths 8

2.1.1 Probability distributions for stochastic systems 8

2.1.2 Transition probability currents 10

2.2 Probability currents as vectorial averages 15

2.3 A numerical strategy for sampling transition currents 18

2.3.1 Diffusion Monte Carlo 18

2.3.2 Algorithm for Transition Current Sampling 21

2.4 Numerical applications 23

2.4.1 Underdamped Langevin dynamics for 1-d potential 23

2.4.2 LJ_{38} cluster 27

2.5 Conclusions 37

3 Lyapunov-biased Transition Path Sampling **43**

3.1 Introduction 43

3.2 Lyapunov Exponents in dynamical systems 45

3.2.1 Continuous time dynamics 45

3.2.2 Discrete dynamics and numerical applications: state of the art . . . 46

3.2.3 Hamiltonian dynamics 49

3.2.4 Maximum local Lyapunov numbers 51

3.2.5 Lyapunov indicator for dynamical trajectories 53

3.3 Transition path sampling with a Lyapunov bias 54

3.3.1 General theory for deterministic TPS 54

3.3.2 Lyapunov biased TPS: shooting and shifting algorithms 56

3.4 Reaction-rate constants calculation 61

3.4.1 Rate constants theory 61

3.4.2 Rate constants with biased sampling and *waste-recycling* 63

3.4.3 Unbiasing rate constants: the MBAR algorithm 64

3.5 Numerical results: LJ_{38} 66

3.5.1 LJ_{38} cluster 66

3.5.2 FCC-ICO reactive paths 67

3.5.3 FCC-ICO reaction constants 72

3.6 Conclusion 79

4 Rate constants for point defect migration in α-Fe **83**
4.1 Thermally activated processes in nuclear materials . . . 84
4.1.1 Numerical methods for irradiated materials study . . . 85
4.2 Vacancy and vacancy clusters migration mechanisms . . . 86
4.3 Reaction rate theory for point defects migration . . . 86
4.3.1 Thermodynamics of Point Defect Formation . . . 87
4.3.2 Microscopic description of diffusion . . . 90
4.3.3 Jump frequency . . . 92
4.3.4 Diffusion coefficient . . . 95
4.4 Migration rate estimates with LyTPS . . . 95
4.4.1 Vacancy migration in α-Iron crystal with LyTPS . . . 96
4.4.2 Divacancy migration in α-Iron crystal . . . 100
4.5 Resistivity recovery experiments . . . 102
4.6 Conclusion . . . 107

5 Conclusion and perspectives **109**

A Hamiltonian dynamics **113**

B Quantum Mechanic analogies **117**
B.1 Schrödinger equation and random walk . . . 117
B.2 Quantum mechanic formulation of Fokker Planck equation . . . 118
B.3 Instanton . . . 119

C Chaos and importance sampling **121**
C.1 The "Lyapunov-weighted dynamics" . . . 121
C.2 Lyapunov exponents and Kolmogorov entropy . . . 122

D Lanczos diagonalization algorithm **125**

E Optimal estimators in MBAR method **129**

F Reaction rate constants theory **133**
F.1 Phenomenological approach . . . 133
F.1.1 A simple model for systems with two stable basins and a metastable transition state . . . 135
F.2 Transition State Theory . . . 136
F.2.1 Separation of time scales . . . 137
F.2.2 Reactive flux method . . . 138
F.2.3 Kramers rate theory . . . 141

F.2.4 One-dimensional TST 142
F.2.5 Multidimensional TST 142

G Embedded Atom Model potentials **145**

Bibliography **147**

Chapter 1

Introduction

In several domains, like material sciences, chemistry and even biology, the evolution of multi-particle systems is often governed by thermally activated processes having a dramatic effect on the structure. These physical events consists of passages between different stable configurations of the system, separated by energetic or entropic barriers. As they usually occur with a very low probability, they are indicated as *rare events*; their frequency, described by the reaction rates, fully determines the global kinetics of the system via its master equations. Examples of physical phenomena controlled by such rare events are protein folding in biology, defect diffusion and crystal nucleation in condensed matter physics and cluster rearrangement in chemistry.

Rare events are characterized by the fact that the typical time needed for them to start is very large, while their duration is rather short, e.g. of the order of the picoseconds in dense molecular systems. This separation of time-scale is the very definition of metastability; its origin may be energetic or, more likely in high dimensional systems, at least partly entropic, when it is related to pathways hard to find. Both features (energetic and entropic) are investigated once one resorts to a free energy description of the activation barrier, able to take into account temperature effects. There are two main issues in the study of rare events: the determination of reactive paths and the computation of reaction rates.

First, reactive paths linking the initial state to the final one have to be found. This problem is intimately related to the exploration of the free energy landscape of a multiparticle system. The determination of reactive paths is connected to the topology of the energy landscape underlying the system dynamics, and requires the localization of transition regions separating stable states. These regions have often a complex conformation, being constituted not only by simple barriers, but by a sequence of saddle point and intermediate metastable basins. This implies, in turn, the problem of the construction in many body systems of reaction coordinates able to accurately discriminate different stable and unstable configurations. Indeed, handling and visualizing systems with a large number of degrees of freedom requires the elaboration of collective coordinates, i.e. a few variable given by functions of the total number of configurational degrees of freedom. Very well-known examples of collective variables are the bond-orientational order parameters,

that are a function of the distances between all particles composing the system. However, the degree of coarse-graining (i.e. the reduction of the number of configurational variables used to describe the system) related to these reaction coordinates needs to be not too strong, in order to avoid a loss of information on the system structure, and subsequently a wrong representation of the energy landscape: in some cases, for example in the study of crystalline symmetries, order parameters take values that do not correspond one-to-one to the different states of the system. This problem worsens when a precise description of the position of transition states in phase space is needed in order to compute quantities like reaction rate (see below), as using inadequate reaction coordinates can induce poor numerical estimations.

The exploration of energy landscapes of complex systems is, for these reasons, a very broad research field, and several exploration techniques have been proposed in the past. The main distinction can be made between zero and finite temperature methods, implying the exploration of the potential energy surface the first, and of the free energy surface the second. Obviously, the latter is more indicated to a proper study of thermally activated events. The first category contains for instance several eigenvector-following methods: in these techniques, saddle points are searched following the unstable direction of the potential energy surface indicated by its negative curvature. In other words, this requires the determination of the matrix of second derivatives of the potential energy - the hessian matrix - that presents a spectra with (some) negative eigenvalues corresponding to unstable directions on saddle points. Thus, a preliminary step prior to calculating finite-temperature reaction paths using these sampling techniques may consist in locating the saddle points of the energy and the corresponding energy minima using one of the eigenvector following methods described in the literature (e.g. the activation-relaxation technique, [9] Optim [11] or the dimer method [12]). A limitation of these methods is that energy saddles only correspond directly to the actual barriers for the dynamics if the temperature is very low, otherwise the entropic contribution to the dynamics becomes relevant.

Conversely, finite temperature methods consist in a large variety of free energy exploring algorithms [2, 71], like histogram methods, biased sampling, umbrella sampling, Wang-Landau, adiabatic switch, or metadynamics [6], that are also very often used to study nonequilibrium problems.

A different approach is followed by methods involving the direct sampling of path ensembles, rather than phase space configurations, and has been developed during the last decade. [2] The strategy is to restrict paths to the subset of reactive paths, those that interpolate between reactant and product basins. Examples of such methods are transition path sampling, [3, 4] transition interface sampling [5]. Another family of methods such as forward flux sampling [7] simulate the evolution in time of the system, and include some form of bias that guarantees that the reaction is observed.

Another approach that may be used to explore the *free-energy* barriers between basins [14, 13] is inspired by Supersymmetric Quantum Mechanics, which has been used in the context of field theory to derive and generalize Morse Theory, precisely the analysis of the saddle points of a function. Transposing this formalism to statistical physics yields a family of generalized Langevin dynamics, converging to barriers and reaction paths of different kinds, rather than to the equilibrium basins. The resulting method involves the evolution in phase space of a population of independent trajectories that are replicated or eliminated according to the value of their Lyapunov exponent.[14]

Indeed, the relation between reactive paths, diverging trajectories and instability in dynamical systems is deeply exploited in this work for the determination of the first ones. The theoretical basis of this relationship is given by the Lyapunov instability theory, that provides observables, called Lyapunov exponents, enabling to quantify the degree of chaoticity on a dynamic system. Chaoticity can be indeed related to the potential energy surface conformation via the spectra of the hessian matrix (this point will be explained in detail in Chapter 3) and transition regions are indeed regions of unstable dynamics. Hence, the determination of diverging trajectories helps in finding barriers separating stable states.

The second issue in rare events studies concerns the determination of the frequency at which these events happen. This frequency is usually indicated as reaction rate, and is indeed a way to quantify "how rare" these events are. A large variety of approaches have been proposed in the past in order to obtain a theoretical description of reaction rates, the most important being the transition state theory elaborated by Eyring, Kramers and others, as well as the "mean first passage time" approach [17]. The fundamental hypothesis for reaction rate theories is again the presence of a well defined separation of time scales: the time that one has to wait in order to see a rare event happening is much larger than the time needed to the system to relax in a given state. The computation of reaction rates is usually related to intermediate time scales between these two times.

Even though physical times of activated events can be achieved in computer simulation using molecular dynamics, monitoring rare fluctuations is computationally expensive and still remains a challenge because of the long waiting time for the event to occur. Therefore, evaluating the frequency of rare events from numerical simulations can also be very time consuming, as the probability of observing one of these passages is very low: for instance, the migration of a vacancy in α-Iron at 500K typically happens every microsecond, while the usual time steps for molecular dynamics is of the order of a few femtoseconds.

To overcome this problem, several alternative strategies have been developed over the past years in order to accelerate the dynamics, and enhance the probability of observing infrequent events during a short simulation, based on importance sampling (see for general reference [71]). A common idea behind these techniques is to bias the dynamics of the system in order to enhance the occurrence of reactions, or to use previous knowledge of the

outcome of the reaction and to fix the endpoint of the trajectory. In order to implement this, in many cases one needs again to know an order parameter able to discriminate between the reactant basin, the saddle regions and the product basin.

Transition path sampling [4] (TPS), already mentioned above, allows to estimate the frequency of rare events by means of path ensemble averages: reaction rates for appropriate time scales are indeed evaluated from the ratio of the number of reactive trajectories on the total amount of paths sampled. However, a sufficient number of reactive paths has to be observed, in order to obtain reliable statistics.

In this PhD thesis, both problems of characterizing reactive paths and evaluating associated reaction constants have been addressed. The first study, focused on the characterization of reactive paths, is presented in details in Chapter 2, and consists of a method called transition current sampling (TCS), derived from a reformulation of the Lyapunov-weighted dynamics of Tailleur and Kurchan [15]. This method is based on the numerical simulation of the probability currents flowing between stable and metastable states, and derives from the SuperSymmetric Langevin dynamics mentioned above. The theory guarantees that by selecting trajectories having larger Lyapunov exponents, the bias is just what is needed so that the population describes the evolution of the *transition current*, rather than the evolution of configurations,[15] as it would in an unbiased case. The advantage is that the convergence of the current distribution is much faster than the typical passage time. The method and its validation have been published as "Simulating structural transitions in transition current sampling: the example of LJ 38", in Journal of Chemical Physics.

The second study is motivated by the necessity of computing reaction constants. This was difficult to achieve within the transition current sampling approach, as TCS is based on the numerical simulation of probability currents, rather than probability distribution. Therefore we elaborated a new approach connected to TCS, that consists in exploiting the advantageous features of a transition path sampling in terms of the computation of reaction constant, but introducing at the same time a bias based again on Lyapunov exponents. This bias can subsequently be removed in the evaluation of reaction rates resorting to an adequate unbiasing statistical tool, the MBAR method. This second work, named local Lyapunov biased transition path sampling (LyTPS) is presented in Chapter 3, and has been submitted to the Journal of Chemical Physics as "Calculation of reaction constants using transition path sampling with a local Lyapunov bias".

This last method is finally applied to the study of thermally activated events occurring in materials of nuclear interest. In particular, the focus was set on post-irradiation point defect migration in crystals, namely vacancies and divacancies, where the migration mechanism and the involved time scales allow a description based on rare events theory. We employed the method developed in Chapter 3 to compute migration rates and give an estimate of migration entropies. The results obtained are reported in Chapter 4, and

have been presented in a proceedings of the conference MRS fall meeting 2011. Migration rates computed are subsequently employed in order to simulate resistivity recovery, and numerical results are furthermore compared with experiments.

Chapter 2

Transition current sampling

Contents

2.1 Probability currents and reaction paths 8
2.1.1 Probability distributions for stochastic systems 8
2.1.2 Transition probability currents 10
2.2 Probability currents as vectorial averages 15
2.3 A numerical strategy for sampling transition currents 18
2.3.1 Diffusion Monte Carlo 18
2.3.2 Algorithm for Transition Current Sampling 21
2.4 Numerical applications 23
2.4.1 Underdamped Langevin dynamics for 1-d potential 23
2.4.2 LJ_{38} cluster 27
2.5 Conclusions 37

Rare events as described in the introduction are intimately connected to the determination of reactive paths in phase space. These reactive paths indicate, indeed, the transformation undergone by the system to pass from the initial to the final state, crossing the transition region. Reaction paths and probabilities are inferred, in a usual Monte Carlo or Molecular Dynamic simulation, directly from the evolution of the positions of the particles. The process becomes time-consuming in many interesting cases in which the transition probabilities are small.

A radically different approach consists of setting up a computation scheme where the object whose time evolution is simulated is the probability current linking stable or metastable states, the *transition current*, that passes through saddles or transition regions of the system. The relevant timescale for such a computation is the one needed for the transition probability *rate* to reach a stationary level, and this is usually substantially shorter than the passage time of an individual system.

This method has been first developed by Tailleur and Kurchan [15] a few years ago, resorting to the quantum mechanics theory of SuperSymmetry. In this PhD thesis, their work has been rederived in a completely classical way, and further applied to a complex many body system in order to validate it.

In this chapter we present a derivation of the probability current dynamics without resorting to quantum theory (section 2.1.2). Extending the more concise demonstration of Ref. [16], we will show how to reproduce the evolution in the phase space of the 'transition' probability current between equilibrium basins, thus achieving a *probability current sampling* of the system dynamics. As the transition current evolves in time, it explores the different barriers, indicating which states are reached after different passage times. Starting from an initial equilibrium configuration, far from equilibrium phenomena are easily sampled, as the simulated current is an intrinsically out of equilibrium quantity [14]. In Sec. 2.3.2, we discuss the actual population dynamic algorithm that may be used to simulate the probability current.

Finally, in order to assess the performances of transition current sampling, we present in section 2.4 the 'benchmark' case of 38 particles interacting via the Lennard-Jones potential ('LJ_{38}' cluster), and we show how this method may be used to explore the reactions that take place between different phases, recovering efficiently known results and uncovering new ones with small computational effort.

The main achievements of this first work are presented in the article published in *J. Chem. Phys.* **135** 034108 (2011). Herein, we also give in more details explanations that were omitted in [88] for brevity reasons.

2.1 Probability currents and reaction paths

2.1.1 Probability distributions for stochastic systems

Let us consider a many-body 3-dimensional system, whose N identical particles of positions $\{q_i\}_{i=1,\dots,3N}$ in phase space interact via a configurational potential $V\left(\{q_i\}_{i=1,\dots,3N}\right)$. The system is coupled to a thermal bath at temperature T, and evolves in a $6N$-dimensional phases space - accounting for both positions q_i and momenta p_i - according to the Langevin dynamics described by the following equations:

$$\dot{q}_i = {m_i}^{-1} p_i \tag{2.1a}$$

$$\dot{p}_i = -\frac{\partial V}{\partial q_i} - \gamma p_i + \sqrt{2 m_i \gamma k_B T}\,\eta_i \tag{2.1b}$$

where m_i are the masses related to the i-th particle, γ is the friction parameter and the η_i are independent gaussian white noises of unit variance and zero average.

We briefly sketch here passages from the Langevin equation of motion to a probabilistic description of a stochastic process. The probability distribution of the positions $\mathbf{q} \equiv (q_1, \cdots q_{3N})$ and momenta $\mathbf{p} \equiv (p_1, \cdots p_{3N})$ of the system particles at time t is defined as

$$P(\mathbf{q}, \mathbf{p}, t) = \langle \delta(\mathbf{p} - \dot{\mathbf{q}}(t)) \delta(\mathbf{q} - \mathbf{q}(t)) \rangle \tag{2.2}$$

where the average $\langle ... \rangle$ is taken over the equilibrium ensemble. As the Langevin dynamics is a Markovian process, P obeys a (Smoluchowski) equation [51]

$$P(\mathbf{q},\mathbf{p},t) = \int d\mathbf{p}' d\mathbf{q}' P(\mathbf{q}',\mathbf{p}',t-dt) T(\mathbf{q}',\mathbf{p}'|\mathbf{q},\mathbf{p};dt) \tag{2.3}$$

where $T(\mathbf{q}',\mathbf{p}'|\mathbf{q},\mathbf{p};dt)$ is the transition probability to go from state $(\mathbf{q}',\mathbf{p}')$ at time t to $(\mathbf{q},\mathbf{p})$ in a time interval dt is such that $\gamma dt << 1$

For concision, we indicate a state in phase space as $\mathbf{x} = (\mathbf{q},\mathbf{p})$. The transition probability can be written with the Kramers-Moyal expansion [1] as

$$T(\mathbf{x}'|\mathbf{x};dt) = [1 + \sum_n \sum_i \frac{1}{n!} \frac{-\partial^n}{\partial x_{i_1} \cdots \partial x_{i_1}} M^{(n)}_{i_1,\cdots,i_n}(\mathbf{x};dt)]\delta(\mathbf{x}'-\mathbf{x}) \tag{2.4}$$

where we introduced n-th order momenta

$$M^{(n)}_{i_1,\cdots,i_n}(\mathbf{x};dt) = \int d\mathbf{y}(y_{i_1}-x_{i_1})\cdots(y_{i_n}-x_{i_n})T(\mathbf{y}|\mathbf{x};dt). \tag{2.5}$$

Eq. (2.4) This is indeed an expansion in Taylor series of $\delta\mathbf{q} = \mathbf{q}-\mathbf{q}'$ and $\delta\mathbf{p} = \mathbf{p}-\mathbf{p}'$, for a small dt. Inserting Eq. (2.4) in Eq. (2.3) and taking the limit $dt \to 0$, Eq. (2.3) becomes

$$\frac{\partial P(\mathbf{x},t)}{\partial t} = \sum_i \sum_n \frac{-\partial^n}{\partial x_{i_1} \cdots \partial x_{i_1}} D^{(n)}_{i_1,\cdots,i_n}(\mathbf{x},t) P(\mathbf{x},t) \tag{2.6}$$

where coefficients D are related to moments M as

$$M^{(n)}_{i_1,\cdots,i_n}(\mathbf{x};dt)/n! = D^{(n)}_{i_1,\cdots,i_n}(\mathbf{x},t)dt + \mathcal{O}(dt^2). \tag{2.7}$$

Coefficients $D^{(n)}$ can be explicitly computed by taking for the transition probability T in the computation of moments M the expression

$$\begin{aligned} T(\mathbf{q}',\mathbf{p}'|\mathbf{q},\mathbf{p};dt) =& \delta\left(\mathbf{q}-\mathbf{q}'-\mathbf{p}dt\right)\cdot \\ & \delta\left(\mathbf{p}-\mathbf{p}'+\frac{\partial V}{\partial q_i}dt + \gamma\mathbf{p}dt - \int \sqrt{2m_i\gamma k_B T}\eta_i(\tau)d\tau\right) \end{aligned} \tag{2.8}$$

and $D^{(n)}$ vanish for $n \geq 3$.

Computing coefficients $D^{(n)}$ in Eq. (2.6) leads to the Kramers-Klein equation [1]

$$\frac{\partial P}{\partial t} = \sum_i \left[\frac{\partial}{\partial p_i}\left(m_i\gamma k_B T \frac{\partial}{\partial p_i} + \gamma p_i + \frac{\partial V}{\partial q_i}\right) - \frac{\partial}{\partial q_i}p_i\right] P \tag{2.9}$$

that is widely used to describe the time evolution of the probability distribution P for systems in weak or intermediate friction regime.

In the limit of large friction $\gamma \to \infty$, where inertia can be neglected, the system dynamics in Eq. (2.1) reduces to a standard overdamped Langevin dynamics

$$\gamma\dot{q}_i = -\frac{1}{m_i}\frac{\partial V}{\partial q_i} + \sqrt{\frac{2\gamma k_B T}{m_i}}\eta_i\ , \tag{2.10}$$

The system state is now described only by positions $\mathbf{q}$, and the probability $P(\mathbf{q},t)$ of being at position $\mathbf{q} \equiv (q_1, \cdots q_{3N})$ then evolves with the Fokker-Planck equation [1]

$$\frac{\partial P}{\partial t} = \sum_i \frac{1}{m_i \gamma} \frac{\partial}{\partial q_i} \left(k_B T \frac{\partial}{\partial q_i} + \frac{\partial V}{\partial q_i} \right) P \equiv -\hat{H}_{FP} P \,, \tag{2.11}$$

where we have introduced the Fokker-Planck operator $\hat{H}_{FP}$.

2.1.2 Transition probability currents

Reading P as a probability density naturally leads to interpret Eqns. (2.11) and (2.9) as *continuity equations*: it is therefore possible to define a *probability current* J as a flux of probability flowing between configurations of the system. This current has the outstanding property of being significantly nonzero on transition regions like saddles, or metastable basins located along the transition path between stable configurations. Probability currents are then suitable to indicate the conformation of reactive paths in phase-space. We present herein first the expression of the probability current for a system with overdumped Langevin dynamics, i.e. whose probability distribution evolves accordingly to the Fokker-Planck equation (Eq. (2.11)); then we express J in the case of a Langevin dynamics with inertia, using Kramers equation (Eq. (2.9)).

Extending further the work of Ref. [14], we derive herein the evolution equation for the associated probability currents, starting from the evolution equation for the corresponding probability density.

2.1.2.1 Overdamped Langevin dynamics

We define the probability current for the Fokker-Planck equation as

$$J_i \equiv -\frac{1}{\gamma m_i} \left(k_B T \frac{\partial}{\partial q_i} + \frac{\partial V}{\partial q_i} \right) P \tag{2.12}$$

in order to write Eq. (2.11) as a continuity equation for the probability density:

$$\frac{\partial P}{\partial t} + \sum_i \frac{\partial J_i}{\partial q_i} = 0 \,. \tag{2.13}$$

For systems with separation of time scales, the dynamics can be split into two regimes. Starting from an arbitrary probability distribution, $P(\mathbf{q};t)$ relaxes *rapidly* into a sum of contributions centered on the metastable states. At *much longer times*, the rare transitions between the metastable states make $P(\mathbf{q};t)$ relax to the equilibrium distribution. Two time scales can also be identified for the dynamics of the probability current. While the probability density rapidly relaxes into the metastable states, the probability current converges *on the same time scale* to the most probable transition paths between the metastable

states. Then, the late time relaxation towards equilibrium corresponds to a progressive vanishing of the current, when forward and backward flux between each metastable state balance [14]. Note that the same line of reasoning holds for non-equilibrium systems in which the forces do not derive from a global potential. In such systems, the probability current never vanishes and converges instead to its steady-state value.

If one were able to simulate the evolution of the probability current, one would thus have all the knowledge relevant for the transitions between metastable states, while only having to simulate the system for relatively short time-scales (similar to the equilibration time within a metastable state). As mentioned in the introduction, simulating directly the transition current is the goal of this paper and we now derive a self-consistent evolution equation for J_i.

Let us define the *current operator* $\hat{J}_i$:

$$\hat{J}_i \equiv \frac{1}{\gamma m_i}\left(k_B T \frac{\partial}{\partial q_i} + \frac{\partial V}{\partial q_i}\right) , \tag{2.14}$$

so that the probability current and the Fokker-Planck operator becomes

$$J_i = \hat{J}_i P \tag{2.15a}$$

$$\hat{H}_{FP} = -\sum_j \frac{\partial}{\partial q_j}\hat{J}_j . \tag{2.15b}$$

The evolution of the probability current is then given by

$$\dot{J}_i = \hat{J}_i \dot{P} = -\hat{J}_i \hat{H}_{FP} P = -\sum_j \hat{J}_i \frac{\partial}{\partial q_j}\hat{J}_j P . \tag{2.16}$$

where we have assumed that H_{FP} does not depend explicitly on time. Straightforward algebra shows that $\hat{J}_i \frac{\partial}{\partial q_j} = \frac{\partial}{\partial q_j}\hat{J}_i - \frac{\partial^2 V}{\partial q_i \partial q_j}$ and $\hat{J}_i \hat{J}_j = \hat{J}_j \hat{J}_i$ which turns equation (2.16) into

$$\dot{J}_i = -\sum_j \left(\frac{\partial}{\partial q_j}\hat{J}_j \hat{J}_i - \frac{\partial^2 V}{\partial q_i \partial q_j}\hat{J}_j\right) P . \tag{2.17}$$

Using the expressions (2.15a) and (2.15b) for the currents and the Fokker-Planck operator we obtain

$$\dot{J}_i = -H_{FP} J_i - \sum_j \frac{\partial^2 V}{\partial q_i \partial q_j} J_j . \tag{2.18}$$

Note that the equations (2.15a) and (2.17) are not self-contained: the knowledge of $P(\mathbf{r})$ is required to compute J_i. On the contrary, (2.18) depends exclusively on the current, and can readily be used to simulate J_i, without having to compute $P(\mathbf{r})$ beforehand. The only condition is that the current distribution at the initial time J_i^0 indeed derives from a probability distribution, i.e. is of the form:

$$J_i^0 \equiv -\frac{1}{\gamma m_i}\left(k_B T \frac{\partial}{\partial q_i} + \frac{\partial V}{\partial q_i}\right) P^0 = -\frac{k_B T}{\gamma m_i} e^{-\frac{1}{k_B T}V} \frac{\partial}{\partial q_i}\left[e^{\frac{1}{k_B T}V} P^0\right] \tag{2.19}$$

This means that the initial current distribution should be such that the quantity A_i

$$A_i = m_i e^{\frac{1}{k_B T} V} J_i^0 \tag{2.20}$$

is a gradient, $\frac{\partial A_i}{\partial q_j} = \frac{\partial A_j}{\partial q_i}$. A particularly simple initial condition is obtained if one assumes that P^0 is Gibbsean $P^0 \propto e^{-\frac{1}{k_B T} V}$ in a region Ω, and zero elsewhere. Then, from Eq. (2.19), J_i^0 is zero everywhere except on the surface of Ω, where it takes the form of a vector normal to the surface of Ω, and with amplitude proportional to the Gibbs weight.

The evolution of current distribution given by Equation (2.18), starting from an appropriate initial current J^0 converges to the stationary distribution of currents between metastable states *on the same time scale* as the usual Langevin equation converges to metastable-state. It is thus not necessary to wait for rare events to identify the transition path between the metastable states, an important improvement over standard MD methods. If there are several metastable states and transitions with different rates, the current distribution at longer times concentrates on the paths between regions that have not yet mutually equilibrated, and vanishes in transitions between states that have had the time to mutually equilibrate.

2.1.2.2 Langevin dynamics with inertia

In many physical situations inertia plays an important role and one cannot rely on overdamped Langevin equations [17]. Taking also into account degrees of freedom related to momenta is therefore necessary: we derive therefore an expression for the probability current starting from the Kramers equation.

As in the overdamped case, this can be written as a conservation equation where the probability current *in phase space* is given by

$$J_{q_i} = \frac{p_i}{m_i} P(\mathbf{q}, \mathbf{p}; t) \tag{2.21a}$$

$$J_{p_i} = -\left(m_i \gamma k_B T \frac{\partial}{\partial p_i} + \gamma p_i + \frac{\partial V}{\partial q_i} \right) P(\mathbf{q}, \mathbf{p}; t) \tag{2.21b}$$

Once again, the current contains all the information about transitions between metastable states. There is however a conceptual difference: the presence of inertia makes it inherently difficult (and indeed, useless), to compute (2.21) as it stands. The reason is that the *phase-space* current

$$J_{q_i} = \frac{p_i}{m_i} P_{\text{eq}} \qquad J_{p_i} = -\frac{\partial V}{\partial q_i} P_{\text{eq}} \, . \tag{2.22}$$

is non-zero even in canonical equilibrium. For example, in a harmonic oscillator $H = \frac{1}{2}\left[\frac{p^2}{m} + q^2\right]$, the phase-space current in equilibrium reads

$$J_{q_i} = \frac{p_i}{m_i} P_{\text{eq}} \qquad J_{p_i} = -q_i P_{\text{eq}} \, . \tag{2.23}$$

and turns clockwise in circles around the origin.

For this reason, the part of the current that corresponds to transitions between metastable states is screened by the large contributions of the currents within metastable states. The probability current (2.21a) and (2.21b) does not really represent the transition paths between metastable states.

We can however define a *transition current* [13]

$$J^{\mathrm{t}}_{q_i} = J_{q_i} + k_B T \frac{\partial P}{\partial p_i} \tag{2.24a}$$

$$J^{\mathrm{t}}_{p_i} = J_{p_i} - k_B T \frac{\partial P}{\partial q_i}, \tag{2.24b}$$

which has two interesting properties. Firstly, this current differs from the probability current by a divergenceless term and thus also satisfies the continuity equation $\dot{P} + \nabla \cdot \mathbf{J}^{\mathrm{t}} = 0$. Fluxes out of a closed surface surrounding a metastable state are then the same for the probability and transition currents. The latter current thus contains the relevant information about, for instance, transition rates. Secondly, the transition current vanishes in equilibrium, as can be checked by comparing (2.22) and (2.24). This current thus contains only the information relevant for the transitions between metastable states and is *not* screened by the large 'equilibrium' currents within them.

Using algebra similar to that of the overdamped case, we show that the reduced current evolves with

$$\frac{\partial \mathbf{J^t}}{\partial t} = -H_K \mathbf{J}^{\mathrm{t}} - \mathbf{M} \cdot \mathbf{J}^{\mathrm{t}} \qquad with \qquad \mathbf{J^t} = \begin{pmatrix} J^t_{q_i} \\ J^t_{p_i} \end{pmatrix} \tag{2.25}$$

where the $6N \times 6N$ matrix $\mathbf{M}$ is given by

$$\mathbf{M} = \begin{pmatrix} 0 & -\frac{1}{m_i}\delta_{ij} \\ \frac{\partial^2 V}{\partial q_i \partial q_j} & \gamma \delta_{ij} \end{pmatrix}. \tag{2.26}$$

Again, (2.25) is a self-consistent equation for the transition current and we shall now show how it can be simulated.

The derivation of the time evolution equation (2.25) for the transition current in the underdamped (i.e., Kramers) case of section is the following.

The classical Kramers probability current $\mathbf{J}$, presented in equations (2.24) , can indeed be written, as in the Fokker-Planck case (Eq. (2.15a)), in the operatorial form $\mathbf{J}(\mathbf{r}, \mathbf{p}, t) = \hat{\mathbf{J}} P(\mathbf{r}, \mathbf{p}, t)$, where the components of the current Kramers operator are

$$\hat{J}_{q_i} = \frac{p_i}{m_i} \tag{2.27a}$$

$$\hat{J}_{p_i} = -\left(m_i \beta^{-1} \gamma \frac{\partial}{\partial p_i} + \gamma p_i + \frac{\partial V}{\partial q_i} \right) \tag{2.27b}$$

In equations (2.24), a *transition current* $\mathbf{J}^t$ has been introduced, which can be expressed in turn with operators as

$$\mathbf{J}^t = \hat{\mathbf{J}}^t P = \left(\hat{\mathbf{J}} + \hat{\mathbf{T}}\right) P \tag{2.28}$$

where $\hat{\mathbf{J}}$ is the Kramers current operator reported above, giving the usual *phase-space* current $\mathbf{J}$, and the 'transition' operator

$$\begin{aligned} \hat{\mathbf{T}}_{q_i} &= \frac{1}{\beta}\frac{\partial}{\partial p_i} \\ \hat{\mathbf{T}}_{p_i} &= -\frac{1}{\beta}\frac{\partial}{\partial q_i} \end{aligned} \tag{2.29}$$

$\hat{\mathbf{T}}P$ is a divergenceless term. As already remarked in section 2.1.2.2, the transition current still satisfies the continuity equation

$$\frac{\partial P}{\partial t} = -\nabla_{\mathbf{q},\mathbf{p}} \cdot \mathbf{J}^t \tag{2.30}$$

thanks to the divergenceless of $\hat{\mathbf{T}}P$. We have introduced here the phase-space divergence $\nabla_{\mathbf{q},\mathbf{p}} \equiv (\nabla_{\mathbf{q}}, \nabla_{\mathbf{p}})$

As in section 2.1.2.1, we proceed now in deriving explicitly the time evolution equation of $\mathbf{J}^t$. Multiplying both sides of the continuity equation above (indeed identical to the Kramers equation (2.9)) by the transition current operator leads to

$$\hat{\mathbf{J}}^{\mathbf{t}}\frac{\partial P}{\partial t} = -\hat{\mathbf{J}}^{\mathbf{t}}\nabla_{\mathbf{q},\mathbf{p}} \cdot \hat{\mathbf{J}}^{\mathbf{t}} P \tag{2.31}$$

On the l.h.s. the transition current operator can be commuted with the time derivative. The r.h.s. of (2.31) can be rewritten with commutators as

$$\hat{\mathbf{J}}^t \nabla_{\mathbf{q},\mathbf{p}} \cdot \hat{\mathbf{J}}^t = \nabla_{\mathbf{q},\mathbf{p}} \cdot \hat{\mathbf{J}} \left(\hat{\mathbf{J}} + \hat{\mathbf{T}}\right) + \left[\hat{\mathbf{J}}, \nabla_{\mathbf{q},\mathbf{p}} \cdot \hat{\mathbf{J}}\right] + \left[\hat{\mathbf{T}}, \nabla_{\mathbf{q},\mathbf{p}} \cdot \hat{\mathbf{J}}\right] \tag{2.32}$$

using (2.31) and the zero divergence property of $\hat{\mathbf{T}}$.

Resorting to definitions of the current operator $\hat{\mathbf{J}}$ and the transition operator $\hat{\mathbf{T}}$ given in (2.27a), (2.27b) and (2.29), explicit expressions for commutators in (2.32) can be recovered with straightforward algebra: the term $\left[\hat{\mathbf{J}}, \nabla_{\mathbf{q},\mathbf{p}} \cdot \hat{\mathbf{J}}\right]$ gives

$$\left[\hat{J}_{q_a}, \nabla_{\mathbf{q},\mathbf{p}} \cdot \hat{\mathbf{J}}\right] P = -\sum_i \delta_{ia} \left(J_{p_i} - \frac{\gamma}{\beta}\partial_{p_i}\right) P \tag{2.33a}$$

$$\left[\hat{J}_{p_a}, \nabla_{\mathbf{q},\mathbf{p}} \cdot \hat{\mathbf{J}}\right] P = \sum_i \delta_{ia} \left(\gamma J_{p_i} - \frac{\gamma}{\beta m_i}\partial_{q_i}\right) P - \sum_i \frac{1}{m_i}\frac{\partial^2 V}{\partial q_i \partial q_a} p_i P \tag{2.33b}$$

while $\left[\hat{\mathbf{T}}, \nabla_{\mathbf{q},\mathbf{p}} \cdot \hat{\mathbf{J}}\right]$ can be expressed as

$$\left[\hat{T}_{q_a}, \nabla_{\mathbf{q},\mathbf{p}} \cdot \hat{\mathbf{J}}\right] P = \sum_i \beta^{-1} \delta_{ia} \left(\partial_{q_i} + \gamma \partial_{p_i}\right) P \tag{2.34a}$$

$$\left[\hat{T}_{p_a}, \nabla_{\mathbf{q},\mathbf{p}} \cdot \hat{\mathbf{J}}\right] P = \sum_i \beta^{-1} \frac{\partial^2 V}{\partial q_i \partial q_a} \partial_{p_i} P \tag{2.34b}$$

Inserting now (2.33) and (2.34) in the r.h.s. of Eq. (2.31) yields

$$(\hat{J}_{q_a} + \hat{T}_{q_a})(\nabla_{\mathbf{q},\mathbf{p}} \cdot \hat{\mathbf{J}})P = (\nabla_{\mathbf{q},\mathbf{p}} \cdot \hat{\mathbf{J}})J^t_{q_a} - \sum_i \delta_{ia}(J_{p_a} - \gamma(\beta)^{-1}\partial_{p_i}P) + \sum_i \beta^{-1}\delta_{ia}(\partial_{q_i} + \gamma\partial_{p_i})P \tag{2.35a}$$

$$(\hat{J}_{p_a} + \hat{T}_{p_a})(\nabla_{\mathbf{q},\mathbf{p}} \cdot \hat{\mathbf{J}})P = (\nabla_{\mathbf{q},\mathbf{p}} \cdot \hat{\mathbf{J}})J^t_{p_a} + \sum_i \delta_{ia}(\gamma J_{p_a} - \frac{\gamma}{\beta}\partial_{q_i}P + \frac{\partial^2 V}{\partial q_i \partial q_a}J_{q_i}) + \frac{1}{\beta}\frac{\partial^2 V}{\partial q_i \partial q_a}\partial_{p_i}P \tag{2.35b}$$

that can be recasted as

$$\hat{\mathbf{J}}^{\mathbf{t}}(\nabla_{\mathbf{q},\mathbf{p}} \cdot \hat{\mathbf{J}})P = (\nabla_{\mathbf{q},\mathbf{p}} \cdot \hat{\mathbf{J}})\hat{\mathbf{J}}^{\mathbf{t}}P + \begin{pmatrix} 0 & -\frac{\delta_{ia}}{m_i} \\ \frac{\partial^2 V}{\partial q_i \partial q_a} & \gamma\delta_{ia} \end{pmatrix} \begin{pmatrix} J_{q_a} + \beta^{-1}\partial_{p_a}P \\ J_{p_a} - \beta^{-1}\partial_{q_a}P \end{pmatrix} \tag{2.36}$$

leading to equation (2.25).

2.2 Probability currents as vectorial averages

The probability densities $P(\mathbf{q}, t)$ (for overdumped Langevin) and $P(\mathbf{q}, \mathbf{p}, \mathbf{t})$ (for underdumped Langevin) are scalar fields, usually obtained numerically by simulating many copies of the system, evolving their positions and velocities with the corresponding Langevin equations (2.1) and (2.10), and constructing histograms. On the contrary, the probability currents are vector fields, hence cannot be obtained in the same way: they also require vectorial degrees of freedom. We herein present a population dynamics that can be used to construct the evolution of the transition current in section 2.2; the corresponding numerical algorithm will be detailed in section 2.3.2.

In order to proceed further for a numerical strategy to sample the probability current, we note that Tanase-Nicola and Kurchan have shown in [16] that the probability current for an overdumped stochastic dynamics in Eq. (2.12) can be written as a vectorial average

$$\mathbf{J} = \int \prod_{i=1}^{3N} \mathrm{d}u_i \; \mathbf{u} \; F(\mathbf{q}, \mathbf{u}, t). \tag{2.37}$$

over some vectors $\mathbf{u}$ that are introduced with the aim of expressing the vectorial degrees of freedom of $\mathbf{J}$. Vectors $\mathbf{u}$ are indeed additional degrees of freedom that will be used to embed the probability current in a larger phase space, and then traced away by integration in Eq. (2.37) to recover $\mathbf{J}$. The joint probability function $F(\mathbf{q}, \mathbf{u}, t)$ couples the distribution of the positions of the system particles with the corresponding vectors $\mathbf{u}$.

Following [14], we first show that the expression (2.37) for the probability current satisfies the probability current evolution equation (2.25) and gives the evolution equation

for F. Indeed, plugging Eq. (2.37) into Eq. (2.25), the lhs of Eq. (2.25) reads

$$\frac{\partial J_a}{\partial t} = \int \prod_{i=1}^{3N} \mathrm{d}u_i \; u_a \; \frac{\partial F(\mathbf{q},\mathbf{u},t)}{\partial t} \tag{2.38}$$

and for the rhs

$$-H_{FP}J_a - \sum_j \frac{\partial^2 V}{\partial q_i \partial q_a} J_j = -\int \prod_{i=1}^{3N} du_i u_a H_{FP} F - \sum_j \frac{\partial^2 V}{\partial q_i \partial q_a} \int \prod_{i=1}^{3N} du_i u_j F(\mathbf{q},\mathbf{u},t) \tag{2.39}$$

We bring the sum over the hessian elements inside the integration on $\mathbf{u}$ writing the last term of Eq. (2.39) as

$$\sum_j \frac{\partial^2 V}{\partial q_i \partial q_a} \int \prod_{i=1}^{3N} \mathrm{d}u_i \; u_j F(\mathbf{q},\mathbf{u},t) = \int \prod_{i=1}^{3N} \mathrm{d}u_i u_a \sum_{ij} \frac{\partial}{\partial u_i} \frac{\partial^2 V}{\partial q_i \partial q_i} u_j F(\mathbf{q},\mathbf{u},t) \tag{2.40}$$

This last passage can be verified by integrating by parts the rhs of Eq. (2.40) with respect to u_a.

From Eqs. (2.38) and (2.39) we thus obtain an evolution equation for the joint probability function

$$\frac{\partial F(\mathbf{q},\mathbf{u},t)}{\partial t} = -H_{FP}F(\mathbf{q},\mathbf{u},t) + \sum_{ij} \frac{\partial}{\partial u_i} \left(\frac{\partial^2 V}{\partial q_i \partial q_i} u_j F(\mathbf{q},\mathbf{u},t) \right) \tag{2.41}$$

Note that the time evolution of F has to take into account the evolution dynamics of both distributions of $\mathbf{q}$ and $\mathbf{u}$. Eq. (2.41) could therefore be derived as well using the following *euristic* considerations [21].

Whenever the dynamics of a given system is due to two processes acting simultaneously, and determining each one a small effect over a sufficiently small time interval (let say of the order of the time step for a molecular dynamics simulation), the joint probability distribution tanking account for these two processes can be recovered in numerical simulations by alternating their effects: if the corresponding time evolutions are identified by two operators $\hat{H}_1$ and $\hat{H}_2$, the time evolution of the joint probability distribution F can be written for each process as $\frac{dF}{dt} = -H_1 F$ and $\frac{dF}{dt} = -H_2 F$, and then recomposed adding the two effects as $\frac{dF}{dt} = -\left(H_1 + H_2\right) F$.

Going back to the Eq. (2.48) , as already mentioned the joint probability function F represents indeed two distinct processes: the stochastic dynamics of the system particles in phase space, that follows Langevin dynamics of Eq. (2.1) , and the evolution of the small vectors $\mathbf{u}$, that act indeed subsequently as a two-step processes.

The Langevin dynamics gives a partial contribution to the joint probability function F exactly deriving from the Fokker-Planck equation:

$$\frac{\partial F}{\partial t} = -\hat{H}_{FP}F \tag{2.42}$$

while the dependence on the current vectorial degrees of freedom, represented by the vectors $\mathbf{u}$, depends on the evolution dynamic of these vectors, that we impose to be

$$\dot{u}_i = -\sum_{j=1}^{N} \frac{\partial^2 V}{\partial q_i \partial q_j} u_j \tag{2.43}$$

Eq. (2.43) directly links the time evolution of the $\mathbf{u}$ vectors with the local conformation of the potential energy surface. We recall now that a generic distribution $P(\mathbf{x}, t)$ carried by a flow $\dot{x}_i = g_i(\mathbf{x})$ evolves as the advective derivative $\dot{P} = \sum_i \frac{\partial}{\partial x_i}(g_i P)$. The dynamics of the vectors in Eq. (2.43) gives therefore a contribution to the total joint probability function $F(\mathbf{q}, \mathbf{u}, t)$ of the type

$$\frac{\partial F}{\partial t} = \sum_{i,j}^{N} \frac{\partial}{\partial u_i} \left(\frac{\partial^2 V}{\partial q_i \partial q_j} u_j F \right) \tag{2.44}$$

Thus, summing up this contribution (2.44) to the Fokker-Planck contribution of Eq.(2.42), one gets the full expression for the evolution of F:

$$\frac{\partial F}{\partial t} = -H_{FP} F + \sum_{i,j}^{N} \frac{\partial}{\partial u_i} \left(\frac{\partial^2 V}{\partial q_i \partial q_j} u_j F \right) \tag{2.45}$$

that is exactly Eq. (2.41), and therefore satisfies the evolution equation of the probability current (2.25).

Finally, note that vectors $\mathbf{u}$ can be replaced by the normalized vectors $\mathbf{v} = \frac{\mathbf{u}}{|\mathbf{u}|}$ such that the diffusion dynamics becomes

$$\dot{v}_i = -\sum_{j}^{N} \frac{\partial^2 V}{\partial q_i \partial q_j} v_j + v_i \sum_{k,l}^{N} v_k v_l \frac{\partial^2 V}{\partial q_k \partial q_l} \tag{2.46}$$

that recasts the evolution equation for the joint probability function as

$$\frac{\partial F}{\partial t} = -H_{FP} F + \sum_{i,j}^{N} \frac{\partial}{\partial v_i} \left(\frac{\partial^2 V}{\partial q_i \partial q_j} v_j - v_i \sum_{k,l}^{N} v_k v_l \frac{\partial^2 V}{\partial q_k \partial q_l} \right) F - \sum_{k,l}^{N} v_k v_l \frac{\partial^2 V}{\partial q_k \partial q_l} F \tag{2.47}$$

where the third term in the rhs of Eq. (2.47) is a reaction term, that can be read as a 'cloning' step of copying and destroying particle, see below.

The very same derivation can be applied to transition currents $\mathbf{J^t}$ in the case of underdamped Langevin dynamics, where the probability distribution P follows the Kramers equation (2.9). The explicit construction of the dynamics has been already presented in a previous paper of Tailleur, Tanase and Kurchan [13]. The derivation proceeds in the same way as for the overdumped case: the 'reduced' probability current of Eq. (2.25) is now expressed as

$$\mathbf{J}^{\mathrm{t}} = \int \prod_{i=1}^{6N} \mathrm{d}u_i \; \mathbf{u} \; F(\mathbf{q}, \mathbf{p}, \mathbf{u}). \tag{2.48}$$

where momenta are explicitly taken into account. Using Eq. (2.48) in Eq. (2.25) one finds for the joint probability function $F(\mathbf{q}, \mathbf{p}, \mathbf{u})$ the evolution equation

$$\frac{\partial F}{\partial t} = -H_K F - \sum_{i=1}^{6N} \frac{\partial}{\partial u_i} \left[-\sum_j M_{ij} u_j + u_i (\mathbf{u}^\dagger \mathbf{M} \mathbf{u}) \right] F - \mathbf{u}^\dagger \mathbf{M} \mathbf{u} F \tag{2.49}$$

The first term of the r.h.s. comes from the Langevin dynamics (2.1), the second one from the evolution of the vector (2.50) and the last one from the birth-death events. The transition current is then given by (2.48). On can indeed check that taking the time derivative of the r.h.s of (2.48) and using (2.49), one recovers the evolution of the transition current (2.25) (see also [14, 13] for a description resorting to quantum SuperSymmetry). As in the Fokker-Planck case, Eq. (2.49) implies for the additional vectors $\mathbf{u}$ a dynamics

$$\dot{\mathbf{u}} = -\mathbf{M} \cdot \mathbf{u} + \mathbf{u} (\mathbf{u}^\dagger \mathbf{M} \mathbf{u}) \tag{2.50}$$

Finally, note that the use of vectors $\mathbf{u}$ to sample transition currents has lead to call this phase space sampling as *Lyapunov Weighted Dynamics* [15]. We explain in Appendix C the reasons of such a denomination.

2.3 A numerical strategy for sampling transition currents

For systems with many degrees of freedom, the direct resolution of the partial differential equation (2.25) yielding the evolution of $\mathbf{J}^t$ is not achievable numerically. In the same way as the Langevin dynamics (2.1) represents an alternative to the resolution of the Kramers equation, we can use a stochastic dynamics that simulates numerically the current evolution (2.25).

The probability currents presented in Eqs. (2.16) and (2.25) are simulated by implementing a Diffusion Monte Carlo algorithm [15]. We here explain why this algorithm is used, giving a short introduction to its basis and meaning, and give a general description of how Diffusion Monte Carlo algorithms work for a phase space sampling of many-body system [19]. A precise description of how this method is practically implemented to simulate the evolution of the probability currents of sections 2.1.2.1 and 2.1.2.2 follows.

2.3.1 Diffusion Monte Carlo

Diffusion Monte Carlo (DMC) belongs to the wider class of the Quantum Monte Carlo sampling methods. These algorithms were initally devoted to the computation of electronic ground-state energies of molecules or other quantum systems. The idea of using a random walk process to simulate a probability distribution for a quantum system was first proposed by Anderson [50], that stressed the similarities of the Schrödinger equation with

a diffusion-reaction process, once imaginary time was considered. The formal analogies between the classical probability density distributions satisfying Fokker-Planck/Kramers of Eqns. (2.11)-(2.9) and quantum mechanics wave functions (see Appendix B) are indeed useful to understand the main reasons that led to the use of DMC in a purely classical statistical mechanics framework, as the transition probability current one. Indeed, the evolution equation of the probability currents (2.25), as well as the joint probability distribution F (2.41), are diffusion-reaction equations, and therefore can be simulated with a DMC scheme.

Let us now give some basic informations on Quantum Monte Carlo sampling schemes. The exact ground energy state $|\psi_g\rangle$ for a quantum system can be determined starting from a known trial state $|\psi_T\rangle$, having energy E_T, by successive applications, say L times, of an hamiltonian-derived operator $G(H)$ such that

$$\lim_{L\to\infty} G(H)^L \, |\psi_T\rangle \sim |\psi_g\rangle \, . \tag{2.51}$$

Taking for G the form

$$G(H) = e^{-t(H-E_t)} \tag{2.52}$$

defines a Diffusion Monte Carlo scheme: as it can be seen, this choice for the hamiltonian-derived operator recalls the same time evolution dynamics for the probability reported in Appendix B (see Eq. (B.5)).

In a Monte Carlo approach, the L successive applications of G are achieved using probabilistic rules: different states are generated using a transition probability $P_{i\to j}$; at each step, a quantity w_{ij} is associated to the generated states. The probability of find a given configuration i_L after L steps, i.e. at a time $t = L\tau$, starting from an initial configuration i_0 is in fact

$$P_{i_L} = \lim_{L\to\infty} \sum_{i_0,\dots,i_L} P\left[i_0 \to \cdots \to i_L\right] \prod_{k=0}^{L-1} w_{i_k i_{k+1}} \tag{2.53}$$

Expression (2.53) has been shown to be a generalized version of Feynman-Kac formulae [20]. This mechanism is achieved using N_c copies of the system, also called *clones*, that act as N_c walkers exploring the phase space. The m-th clone is denoted at time t by a corresponding set of coordinates $\mathbf{X}_t^m$. A control parameter κ is used to divide the simulation in time intervals of length $\Delta t = \kappa\delta t$. First, a walkers displacement is achieved letting the clones propagate with a common molecular dynamics algorithm, for instance using a leap-frog discretized Langevin dynamics [23], with time steps δt, for a duration $\kappa\delta t$: this is the *propagation step*.

Subsequently, a branching or "birth-death" process, associated to the quantities w_{ij} is introduced: the current configuration is destroyed or copied a number of times proportional to its own local weight, depending on w_{ij}. To this aim, at times $n\Delta t$, clones undergo a

selection step: a stochastic procedure decides whether a particular clone is duplicated or deleted [93] based on its probability weight. The normalized probability weight ρ_n^m, related to the *m-th* clone at time $n\Delta t$, are computed from the quantities $w(\mathbf{X}^m_{n\Delta t})$ for each walker as

$$\rho_n^m = \frac{w(\mathbf{X}^m_{n\Delta t})}{\sum_{m=1}^{N_c} w(\mathbf{X}^m_{n\Delta t})}$$

In practice, it amounts to either keeping the clone coordinates unchanged before the subsequent propagation or replacing them with coordinates of another clone. Note that even though the clone evolve independently during the propagation step, their dynamics are intercorrelated because the deleted clones are replaced by the duplicated ones at the selection steps.

With this approach, the number of configuration would be no longer constant, but would diverge or vanish as the simulation has led towards phase space regions with respectively too large or too small weights: a purely diffusive MC scheme has indeed be shown to be divergent [10]. For these reason, a further step to control the total amount of configurations is required, consisting in a random deletion/duplication step, in order to keep the total number of configurations approximately constant and ensure the numerical stability of the method.

A stratified resampling scheme [25] is used to decide whether to duplicate or delete each clone, while keeping the total clones population constant. At time $(n-1)\Delta t + \kappa\delta t$, the stratified resampling reallocate the coordinates of all the clones $\left\{\mathbf{X}^m_{(n-1)\Delta t+\kappa\delta t}\right\}_{1\leq m\leq N^c}$ as follows [93]

$$\widetilde{\mathbf{X}}^m_{n\Delta t} = \sum_{j=1}^{N_c} \mathbf{1}_{\left\{N^c \sum_{l=1}^{j-1} \rho_n^l + U_n^m < m < N^c \sum_{l=1}^{j} \rho_n^l + U_n^m\right\}} \mathbf{X}^j_{(n-1)\Delta t+\kappa\delta t}$$

where $\mathbf{1}$ denotes a uniform distribution on the interval indicated in the subscript, and the U_n^m denote N^c independent random variables distributed according to the uniform law on $(0,1]$ generated at time $n\Delta t$.

When the probability weights are all equal, we have $\rho_n^m = 1/N^c$ and $j-1$ can be substituted for $N^c \sum_{l=1}^{j-1} \rho_n^l$ in (2.3.1). As a result, the clones are left unchanged through stratified resampling. Conversely, when the clone weights take distinct values in Eq. (2.3.1), clones with small weights are likely to be replaced by those with large weights. The parameter κ which controls the coupling between propagation and selection is tuned in practice to ensure ergodicity in phase space.

Note that this stochastic reconfiguration step introduces a finite bias, and has to be accurately performed. However, this resampling strategy is advantageous in computer simulations: indeed, for numerical purposes, it is evident that this last step avoids spending large simulation times in phase space regions having small weights, thus increases the sampling efficiency, and focusing the sampling mainly on interesting configurations. Finally,

there exists other selection schemes in the literature, like multinomial resampling or residual resampling. Their numerical efficiency were assessed on a simple benchmark study and were found to be better than the one of the simple stratified resampling scheme herein considered [93]. These more elaborated schemes have not been tested in this study.

2.3.2 Algorithm for Transition Current Sampling

We here present the implementation of the population dynamics of the clones and then discuss the construction of the transition current. In practice, the coupling between the vectorial and phase space degrees of freedom is obtained by the following population dynamics. The $\mathcal{N}$ copies of the system (called 'clones'), identified by positions and velocities $\mathbf{q}$ and $\mathbf{p}$, all carry a $6N$ dimensional unitary vector $\mathbf{u}$. The dynamics of each clone is then as follows: [13]

- $\mathbf{q}$ and $\mathbf{p}$ evolve with the standard Langevin dynamics with inertia (2.1)
- vectors $\mathbf{u}$ evolve with Eq. (2.50)
- each clone has a *birth-death rate* $\alpha = -\mathbf{u}^\dagger \mathbf{M} \mathbf{u}$. This is the only way the vector $\mathbf{u}$ influences the dynamics.

The distribution of clones in phase space then correctly samples $F(\mathbf{q}, \mathbf{p}, \mathbf{u})$, reproducing Eq. (2.49) [18].

The DMC scheme presented above is readily applied to the specific case of transition currents, once the $m-th$ clone is identified by $\mathbf{X}_t^m = \{\mathbf{q}^m(t), \mathbf{p}^m(t), \mathbf{u}^m(t)\}$ and quantities $w(\mathbf{X}_{n\Delta t}^m)$ are taken to be

$$w(\mathbf{X}_{n\Delta t}^m) = ||\mathbf{X}_t^m|| \tag{2.54}$$

where the seminorm $||\mathbf{X}_t^m|| = \left(\sum_{i=1}^{6N} u_i^2(t)\right)^{1/2}$ indeed corresponds to the norm of the $\mathbf{u}$ vector, associated to each clone at a given time step. The probability weight hence reads

$$\rho_n^m = \frac{||\mathbf{X}_{n\Delta t}^m||}{\sum_{m=1}^{N_c} ||\mathbf{X}_{n\Delta t}^m||} \tag{2.55}$$

Moreover, after the selection and before the new propagation, each vector $\mathbf{u}(t)$ is renormalized to one, in order to follow Eq. (2.50) The coordinates $\{\mathbf{X}_{n\Delta t}^m\}_{1\leq m\leq N^c}$ of the clones passing the selection step are then rescaled as $\left\{\widetilde{\mathbf{X}}_{n\Delta t}^m\right\}_{1\leq m\leq N^c}$

$$\mathbf{X}_{n\Delta t}^m = \{\widetilde{\mathbf{q}}^m(n\Delta t), \widetilde{\mathbf{p}}^m(n\Delta t), \widetilde{\mathbf{u}}^m(n\Delta t)/||\widetilde{\mathbf{u}}^m(n\Delta t)||\}\,. \tag{2.56}$$

The algorithm deriving from all these considerations in the following: we start with $\mathcal{N}_c$ clones whose positions and vectors are arbitrarily chosen. At every time step, the dynamics is:

1. All the vectors $\mathbf{u}^m$ are rescaled to have a unitary norm.

2. The positions and velocities of the clones are propagated using a leap-frog discretized Langevin dynamics. [23, 24]

3. The vectors $\mathbf{u}^m$ evolve with the (leap-frog discretized version of) the following dynamics:
$$\dot{u}_i^m = -M_{ij} u_j^m \tag{2.57}$$
Note that at after this step, the vectors are no more of unitary norm.

4. For each clone one records $w_m = ||\mathbf{u}^m(t+\delta t)||$.

5. We associate to each clone m a probability weight $\rho_m = \mathcal{N}_c w_m / \sum_i w_i$ and a random number ε_m chosen uniformly in $[0,1)$. The clone is then replaced by y_m copies, with
$$y_m = \lfloor \rho_m + \varepsilon_m \rfloor \tag{2.58}$$
where $\lfloor x \rfloor$ is the integer part of x: if $y_m > 1$, $y_m - 1$ new copies of the m-th clone are made. If $y_m = 0$, the clone is deleted and if $y_m = 1$, nothing happens. The population size is thus increased by $y_m - 1$ if $y_m > 1$ or decreased by 1 if $y_m = 0$.

6. After the step 5, the population is rescaled from its current size $\mathcal{N}_c^e = \sum_{m=1}^{\mathcal{N}_c} y_m$ to its initial size $\mathcal{N}_c$, by uniformly pruning/replicating the clones.

Steps 1 to 3 correspond to the propagation step of independent clones, whereas steps 4 to 6 correspond to selection steps. In particular, the steps 4 and 5 correctly represents the cloning rate $\alpha = -\mathbf{u}^\dagger \mathbf{M} \mathbf{u}$ of the previous subsection since $\frac{\mathrm{d}}{\mathrm{d}t}||\mathbf{u}^m(t)|| = -\mathbf{u}^{m\dagger}\mathbf{M}\mathbf{u}^m$, so that $||\mathbf{u}^m(t+\delta t)|| \simeq \exp(-\delta t \mathbf{u}^{m\dagger}\mathbf{M}\mathbf{u}^m)$.

The rescaling of the population at the step 6 can be done in many ways. For instance, one can pick a new clone at random $\mathcal{N}_c$ times among the $\mathcal{N}_c^e$ clones obtained at the end of the step 5. We used an alternative approach that is less costly in terms of data manipulations: if $\mathcal{N}_c^e > \mathcal{N}_c$, we kill $\mathcal{N}_c^e - \mathcal{N}_c$ clones chosen uniformly at random among the $\mathcal{N}_c^e$ obtained at the end of the step 5. Conversely, if $\mathcal{N}_c^e < \mathcal{N}_c$, we choose uniformly at random $\mathcal{N}_c - \mathcal{N}_c^e$ clones and duplicate them. Note that even though the clones evolve independently during the propagation step, their dynamics are correlated because the deleted clones are replaced by the duplicated ones at the selection steps. When the probability weights of the clones are all equal, we have $\rho_m = 1$ and $y_m = 1$. As a result, the population is left unchanged. Conversely, when the clone weights take distinct values, clones with small weights are likely to be replaced by those with large weights.

There are many ways of implementing the resampling of the population (steps 5-6), well documented in the literature on Diffusion Monte Carlo. [93, 25] In particular, it could be advantageous to do the resampling only every n time steps, where n is tuned to ensure

ergodicity in phase space, i.e. to achieve enhanced sampling towards the unstable regions where saddles are located.

Since the clones move in phase space with a Langevin dynamics, it can be surprising that they converge rapidly to the reaction paths, i.e. that they explore efficiently the transition states. This can however be understood by noting that their dynamics (without taking the averages (2.48)) is the so-called *Lyapunov Weighted Dynamics* [15] which is used to bias the Langevin dynamics in favor of chaotic trajectories. The clones will then tend to 'reproduce' favorably in the neighborhood of saddles, which are particularly chaotic regions of phase space, and to die in wells. This generates an 'evolutionary pressure' that helps the clone escape from metastable states and find the reaction paths.

As mentioned before, this dynamics does not provide *directly* the transition current and one still has to construct the averages (2.48). This can be difficult and clever methods to do so were discussed in the literature, for instance by Mossa and Clementi who studied the folding of chain of aminoacids. [28] The difficulty is connected to the well-known sign problem: large population of clones with arrows pointing in opposite directions cancel in the average but can numerically screen smaller asymmetric distribution that contains the information relevant for the transition current. One can however show that if one starts from a population of clones uniformly spread over a reaction path separating two metastable states and pointing in the same direction, the time taken for the sign problem to occur is of the order of the tunneling time through the barrier (see below Section 2.4.1). In the following we will always simulate much shorter times and omit the averaging steps to simply look at the distribution of clones. This distribution often suffices to locate the reaction paths. To extract further information, for instance regarding the reaction rates, we would need to do the averages, as was done in [28].

2.4 Numerical applications

2.4.1 Underdamped Langevin dynamics for 1-d potential

We first present an application of transition current sampling in a simple one dimensional system. The aim of this first study is to allow us to discuss several aspects of the clone dynamics, namely the metastability, the finiteness of the clone population and the role of the initial condition. Moreover, this one dimensional model shows that it is possible to characterize reaction paths doing simulations of the stochastic dynamics of the clones without explicitly making the averages (2.48) that would yield the transition current, as argued in section 2.3.2.

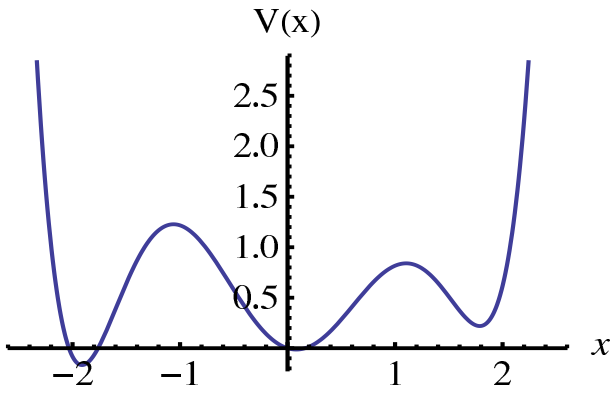

Figure 2.1: Plot of the potential $V(x) = x(-39 + 240x + 15x^2 - 138x^3 + 20x^5)/120$.

We consider a system undergoing an underdamped Langevin dynamics

$$\dot{x} = p/m \tag{2.59}$$

$$\dot{p} = -\gamma p - V'(x) + \sqrt{2\gamma kTm}\,\eta \tag{2.60}$$

where $V(x)$ is a potential with two barriers, plotted in figure 2.1. We ran the clone dynamics for 2000 clones starting in the left well and carried out the averages (2.48).

To do so, we constructed an approximate density from the positions and vectors (x^i, p^i, u_x^i, u_v^i) of each of the $\mathcal{N}_c = 2000$ clones:

$$\mathcal{F}_{\text{num}}(x, p, u_x, u_v) = \frac{1}{\mathcal{N}_c} \sum_{i=1}^{\mathcal{N}_c} \delta(x - x^i)\delta(p - p^i)\delta(u_x - u_x^i)\delta(u_p - u_p^i) \tag{2.61}$$

In principle, the δ should be Dirac functions but for practical purposes we replaced the one acting on the phase space coordinate by the bell-shaped function

$$\delta_n(x, p) = \frac{1}{Z} \exp\left(-\frac{1}{1 - \frac{x^2+p^2}{w^2}}\right) \tag{2.62}$$

if $x^2 + p^2 < w^2$ and

$$\delta_n(x, p) = 0 \tag{2.63}$$

otherwise, where $w = 0.1$ and Z is a normalization constant. Finally, using (2.61) and (2.62) in (2.48), we construct the transition current from the numerical data by computing

$$\mathbf{J}^{\mathbf{T}}(x, p) = \frac{1}{\mathcal{N}_c} \sum_{i=1}^{\mathcal{N}_c} \mathbf{u}^i\, \delta_n(x - x_i, p - p_i) \tag{2.64}$$

on a grid every $dx = dy = 0.15$ and plot the resulting vector if its norm is larger than 10^{-3}. For visualization purposes, we plot in the figures the vectors 5 times longer than they really are.

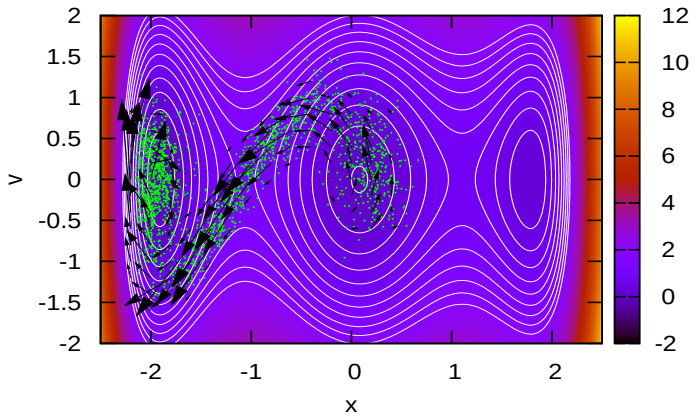

Figure 2.2: The green crosses are the position of the 2000 clones after a time $t = 400$. The black arrows correspond to the averages (2.64) and indeed point tangentially to the reaction path. The color code and contour lines corresponds to the value of the Hamiltonian $H(x, v) = p^2/2m + V(x)$

We started a simulation with 2000 clones in the left well, around $x = m_1 \simeq -1.9$, with unitary vectors (u_x, u_y) pointing at random. The temperature is set to $kT = 0.09$ and the friction to $\gamma = 1.5$ so that the mean first passage time τ_e across the barrier is (see [17] and Appendix F)

$$\tau_e^{-1} = k_{L\to C} \simeq \frac{2\pi}{\sqrt{\gamma^2/4 + |V''(M_1)|} - \gamma/2}\sqrt{\frac{|V''(M_1)|}{V''(m_1)}}e^{\frac{V(M_1)-V(m_1)}{kT}} \simeq 10^7 \qquad (2.65)$$

where M_1 is the first maximum of the potential $M_1 \simeq -1$. The results of the simulation after a time $t = 400$ are plotted in figure 2.2. The clones have already populated the barrier. Note that with standard Langevin MD simulations of the same duration, the probability that none of the 2000 clones has crossed the barrier is more than 90%. As can be seen, the averages (2.64) along the reaction path are non-zero and result in vectors tangent to the reaction path, pointing toward the left well.

At later times, two processes take place, roughly on the same time scale. Firstly, more and more clones come back from the central well to the left one. Their vectors $\mathbf{u}$ are always tangent to their trajectories, but can be pointing toward the left or the central well with equal probability. Indeed, if $(q(t), p(t), \mathbf{u}(t))$ is a possible trajectory of the system, then so is $(q(t), p(t), -\mathbf{u}(t))$. As a result, the averages (2.64) may cancel out at large times, when the subpopulations of clones whose vectors $\mathbf{u}$ point toward the central and the left wells balance. This is how numerically the transition current is supposed to vanish at large time

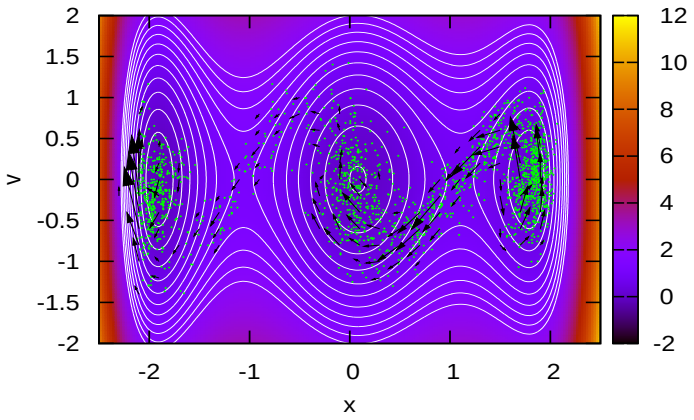

Figure 2.3: $t = 997$ the clones populate both barriers. The arrows average out along the reaction path between the left and central wells which have equilibrated, whereas the transition current is still present between the central and right wells

(another possibility being that all the clones leave a region of phase-space, because of finite population-size effects).

Secondly, some clones reach the barrier leading to the right well and duplicate, which results in populating the second reaction path. Since the clones did not have time to fall in the right well and cross back the barrier towards the central well with vectors $\mathbf{u}$ pointing in the opposite direction, the average (2.64) does not cancel along this reaction path.

Both effects can be seen in Fig. 2.3 and 2.4 : the clones populate both barriers; the average (2.64) cancels out over the first barrier but not yet over the second one. This shows that the clone dynamics do locate the barriers and remain on the reaction paths even though the transition current may average out when the two wells separating a barrier equilibrate. This enables us to follow the same approach to more complex systems.

Note that if one wishes to study quantitatively the transition current, two modifications would need to be done to our algorithm. First, the initial condition should not be taken at random but constructed as proposed in section 2.1.2.1. Second, rather than simulating all the clones in parallel while maintaining their population constant, it may be advantageous to run them sequentially, starting one run for every offspring of every clones, as is done for instance with the 'Go with the winner' methods. [49] The constrain on the total population being fixed indeed affects the metastability of the clone dynamics and increases finite size effects. For instance, if there are $\mathcal{N}_1$ and $\mathcal{N}_2$ clones on the same reaction path, with vectors pointing in opposite directions, both populations grow exponentially with the

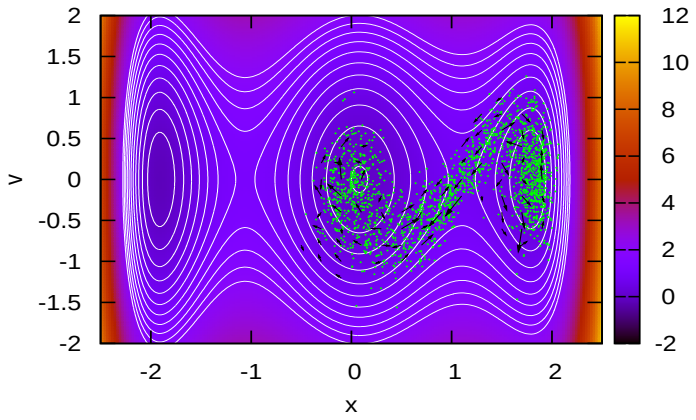

Figure 2.4: At $t = 1590$ the clones only populate the reaction path between the central and right wells. Since the simulation had enough time to equilibrate the involved wells, the average (2.48) cancels out.

same rate. Now, if the total population is kept constant, then the smallest sub-population disappears on average exponentially fast. Using a 'Go with the winner' method would palliate this drawback but would result in additional computational costs difficult to estimate beforehand.

2.4.2 LJ_{38} cluster

We now turn to the study of transitions between metastable states in the 38-atom Lennard-Jones cluster, a benchmark model system that has been extensively investigated in the past. [26, 27, 30, 31, 23] This system has a complex potential energy landscape organized around two main basins: a deep and narrow funnel contains the global energy minimum, a face-centered-cubic truncated octahedron configuration (FCC), while a separate, wider, funnel leads to a large number of incomplete Mackay icosahedral structures (ICO) of slightly higher energies.

Although the lowest potential energy minimum corresponds to the FCC structure, the greater configurational entropy associated to the large number of local minima in the icosahedral funnel make this second configuration much more stable at higher temperatures. As temperature increases, this system thus undergoes the finite-size counterpart of several phase transitions. First, a solid-solid transition occurs at $T_{ss} = 0.12\frac{\varepsilon}{k_B}$ when the octahedral FCC structure gives place to the icosahedral ones. At a slightly higher temperature, $T_{sl} = 0.18\frac{\varepsilon}{k_B}$, the outer layer of the cluster melts, while the core remains of icosahedral

structure. [32] This 'liquid-like' structure, also referred to as anti-Mackay in the literature, then completely melts around $T_{sl} = 0.35\frac{\varepsilon}{k_B}$ [32].

The numerical study of this system is challenging: global optimization algorithms have failed to find its global energy minimum for a long time [2] and direct Monte Carlo sampling fails to equilibrate the two funnels. The study of the equilibrium thermodynamics of this system required more elaborate algorithms such as parallel tempering, [30, 31, 32] basin-sampling techniques, [33] Wang-Landau approaches [34] or path-sampling methods [23, 35, 36].

More recently, the dynamical transitions between the two basins has been studied following various approaches. The interconversion rates between the FCC and ICO structures have been computed using Discrete Path Sampling. [37, 38, 39] This elaborate algorithm relies on the localization of minima and saddles of the potential energy landscape, using eigenvector following, and then on graph transformation [41] to compute the overall transition rate between two regions of phase space. To the best of our knowledge, this is the most successful approach as far as computing reaction rates in LJ_{38} is concerned. [41] However, the numerical methods involved are quite elaborate, require considerable expertise and have a number of drawbacks, all deriving from the fact that it is based on the harmonic superposition approximation and the theory of thermally activated processes. It thus requires any intermediate minima between the two basins to be equilibrated and this is only possible for small enough systems at low temperatures. [37] More importantly, when the difficulty in going from one basin to the other is due to entropic problems, as is the case for instance in hourglass shaped billiards, then the knowledge of minima and saddles of the potential energy landscape is not sufficient.

Another attempt to study the transitions between the two funnels of LJ_{38} relies on the use of transition path sampling. [35] Because of the number of metastable states separating the two main basins, the traditional shooting and shifting algorithm failed here, despite previous success for smaller LJ clusters. [42] The authors thus developed a two-ended approach which manages to successfully locate reaction paths between the two basins: they started from a straight trial trajectory linking the two minima, and obtained convergence towards trajectories of energies similar to those obtained in the Discrete Path Sampling approach. [35] Although the authors point out the lack of ergodicity in the sampling within their approach and the sensitivity on the 'discretization' of the trajectories, this is nevertheless a progress and the main drawback remains the high computational cost (the work needed 10^5 hours of cpu time) to obtain such converged trajectories. In contrast, the simulations we present below required less than 10^2 hours of cpu time.

2.4.2.1 The LJ_{38} cluster and bond-orientational order parameters

Before presenting our simulations results, we give some technical details on the LJ_{38} system and on the visualization of the different metastable states. The Lennard-Jones potential is given by the expression

$$V\left(\left\{\mathbf{q}^j\right\}_{j=1,\dots,N}\right) = 4\varepsilon \sum_{j<k}\left[\left(\frac{\sigma}{r_{jk}}\right)^{12} - \left(\frac{\sigma}{r_{jk}}\right)^{6}\right] \tag{2.66}$$

where $\mathbf{q}^j = (q_x^j, q_y^j, q_z^j)$ is the position of the j-th atom, $r_{jk} = \left|\mathbf{q}^j - \mathbf{q}^k\right|$ is the distance between atoms j and k, ε is the pair well depth and $2^{1/6}\sigma$ is the equilibrium pair separation. In addition, all the particles are confined by a trapping potential that prevents evaporation of the clusters at finite temperature (i.e. particles going to infinity). If the distance between the position $\mathbf{q}$ of a particle and the center of the trap $\mathbf{q_c}$ exceeds 2.25σ, then the particle feels a potential $|\mathbf{q}-\mathbf{q_c}|^3$. LJ reduced units of length, energy and mass ($\sigma = 1, \varepsilon = 1, m = 1$) will be used in the sequel so that the time unit $t = \sigma\sqrt{m/\varepsilon}$ is set to 1.

Rather than listing the 228 degrees of freedom of the atomic cluster, configurations are traditionally described using the Q_l bond-orientational order parameters [43, 44] that allow to differentiate between various crystalline orders

$$Q_l = \left(\frac{4\pi}{2l+1}\frac{1}{N_b^2}\sum_{m=-l}^{l}\left|\sum_{N_b} Y_{lm}\left(\theta_{jk}, \phi_{jk}\right)\right|^2\right)^{1/2}, \tag{2.67}$$

where the $Y_{lm}(\theta, \phi)$ are spherical harmonics and θ_{jk}, ϕ_{jk} are the polar and azimuthal angles of a vector pointing from the cluster center of mass to the center of the *(j,k)* bond which connects one of the N_b pairs of atoms. Note that whereas some authors restrict the sum over bonds connecting atoms of the inner core [32, 45], we include all the bonds in our definition. The parameter Q_4 is often used to distinguish between the icosahedral and cubic structures, for which it has values around 0.02 and 0.18 respectively. [30] Q_4 however does not distinguish between the icosahedral and the liquid-like phase and one thus often uses Q_6, for which FCC, icosahedral and the liquid-like phase take values around 0.5, 0.13 and 0.05, [27] respectively. To show the spread of the various basins in the (Q_4, Q_6) plane, we ran several molecular dynamic simulations, long enough to equilibrate within each basin but short enough so that one does not see tunneling (see figure 2.5).

Although the whole temperature scale is interesting, the challenging part from a computational point of view is the low-temperature regime where ergodicity is difficult to achieve. Below, we show the results of our algorithm for three temperatures: $T = 0.12\varepsilon/k_B$, $T = 0.15\varepsilon/k_B$ and $T = 0.19\varepsilon/k_B$ that span the ranges around the solid-solid and partial melting transitions.

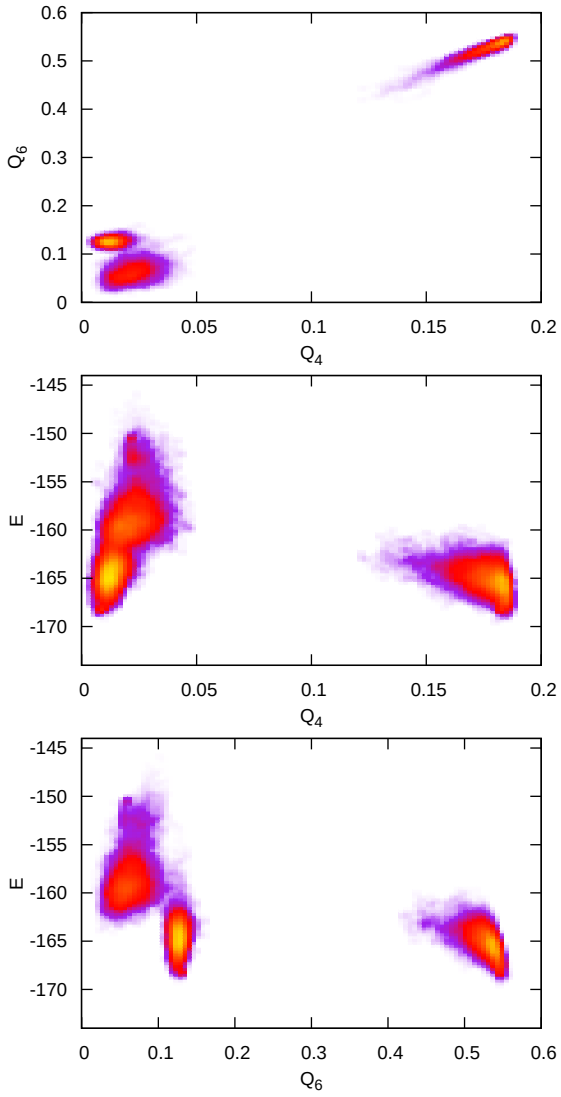

Figure 2.5: Short MD simulations were run to give an impression of the spread in the (Q6,Q4,E) space of each 'phase'. The simulation time was short enough that no tunneling between the phases was observed. The temperature was set to $T = 0.15$. The positions of the phases barely move in the (Q_4, Q_6) plane when the temperature changes, although their spreading does. The kinetic energy however shifts when the temperature changes, and is roughly proportional to NkT where N is the number of degrees of freedom.

2.4.2.2 Simulations

Given the high dimensionality of the system, it is difficult to follow the evolution of all the coordinates of the clones in order to know if they have localized interesting structures. Instead, we proceed as follows: we plot the evolution of the average over the clone population of Q_4, Q_6 and E as a function of the simulation time and we frequently store the positions and velocities of all the clones.

If we see a plateau in $Q_4(t)$, $Q_6(t)$ and $E(t)$, two cases are possible: either the clones have converged to a reaction path, or they are stuck in a metastable basin. In order to distinguish the two situations, we run an auxiliary short molecular dynamic simulation (*without cloning*) starting from the positions and velocities of the clones. The duration of this auxiliary simulation is long enough to observe relaxation into the metastable basins, but much shorter than the transition times. If the clones evolve away from the region they had populated in phase-space, we know they had found a reaction path and the auxiliary MD simulation converges to the metastable basins connected by this reaction path. If on the other hand the clones do not evolve away, we know that they had been stuck in some local basin. In such a case we can change two parameters to enhance the sampling of the phase space: the number of clones and the friction γ (see below for more details). The time step is always $\delta t = 0.01$. Note that this procedure could be automated, but the way to do so is let for future work.

In principle, any observable that can measure whether the population of clones splits in two separate sub-populations after a short Langevin dynamics would be suitable. If the clone population splits in two subpopulations with the same Q_4, Q_6 and E, we may fail to detect the corresponding barrier. However, this coincidence would be extremely unlikely.

Last, in addition to help us localize barriers, these short Langevin simulations allows us to explore the true dynamics close to a particular transition states.

2.4.2.3 $T = 0.15$

We first ran several simulations at $T = 0.15$, where the most stable state is the MacKay icosahedral minimum (ICOm) while the liquid-like phase (ICOam) and the FCC basin are metastable.

Starting from the ICOm basin with $\mathcal{N} = 200$ clones and a low friction $\gamma\delta t = 10^{-3}$, the clones rapidly find ($t \sim 1500$) a transition path to the liquid-like phase ICOam. Later on ($t \sim 3500$) an activated event bring the clones to another reaction path that points towards the FCC funnel. These times have to be compared with the transition time between the ICOm and FCC basins that was previously evaluated in the literature at roughly 10^7. [37] Note that each barrier or path act as a metastable state for the cloned dynamics and it is by activation that the population jumps from one barrier to another. Running the same

dynamics with a larger number of clones ($\mathcal{N} = 600$) tends to stabilize the first barrier so that one has to wait longer to see the transition to the second one.

Starting from the FCC minimum with the same number of clones and at the same friction results in the clones rapidly going out of the FCC funnel and falling in the amorphous zone at the entrance of the icosahedral funnel. [30] A reaction path is *followed* by the clones but not *maintained*. To stabilize this reaction path, we increased the number of clones and the friction. The effect of the former is mostly to slow down the dynamics while the latter allow the clones to populate the reaction path more uniformly. For $\mathcal{N} = 600$ clones and $\gamma\delta t = 1$, the population of clones indeed stabilizes the reaction path leading from the FCC basins to the entrance of the icosahedral funnel. The reason why we need more clones to stabilize this barrier than the ones in the icosahedral funnel is probably that the former is more flat and spread than the latter ones [27] and thus requires a larger number of clones to be sampled uniformly.

All these results are plotted on figure 2.6, in which we show the three basins ICOm, FCC and ICOam obtained from the initial MD simulations (see figure 2.5) and the positions of the clones in the (Q_4, Q_6) and (Q_6, E) plans at different simulation times.

To identify the various metastable basins connected by the clones, we ran several short MD simulations starting from the two long-lived plateaux (blue and green arrows in the right panel of figure 2.6). Histograms made from these MD runs are shown in figure 2.7. They show that the clones going out of the ICO basin find barriers toward the amorphous region at the entrance of the ICO funnel while the ones starting from the FCC minimum find a reaction path between the FCC basin and the icosahedral funnel. Interestingly, this path goes through a faulty FCC basin located around $(Q_4, Q_6) = (0.12, 0.45)$ that has been previously reported in the literature. [30, 23]

The clones have thus found reaction paths pointing out of their starting funnels. The clones starting from the FCC basins find a reaction path that leads into the icosahedral funnel while the one started from the ICOm basin still remain in the icosahedral funnel. This could be explained by the fact that at this temperature ICOm is the *stable* state while FCC is only metastable so that the barrier ICO→FCC has to be harder to access than the one from the FCC side. Running short MD starting from the clones positions reveal intermediate metastable basins, either a faulty FCC or amorphous structures.

2.4.2.4 $T = 0.12$

This is the coexistence temperature between the ICOm and FCC minima. At such a low temperature, more and more secondary barriers play a role so that the transition between ICO and FCC becomes more and more complex. From the point of view of the time

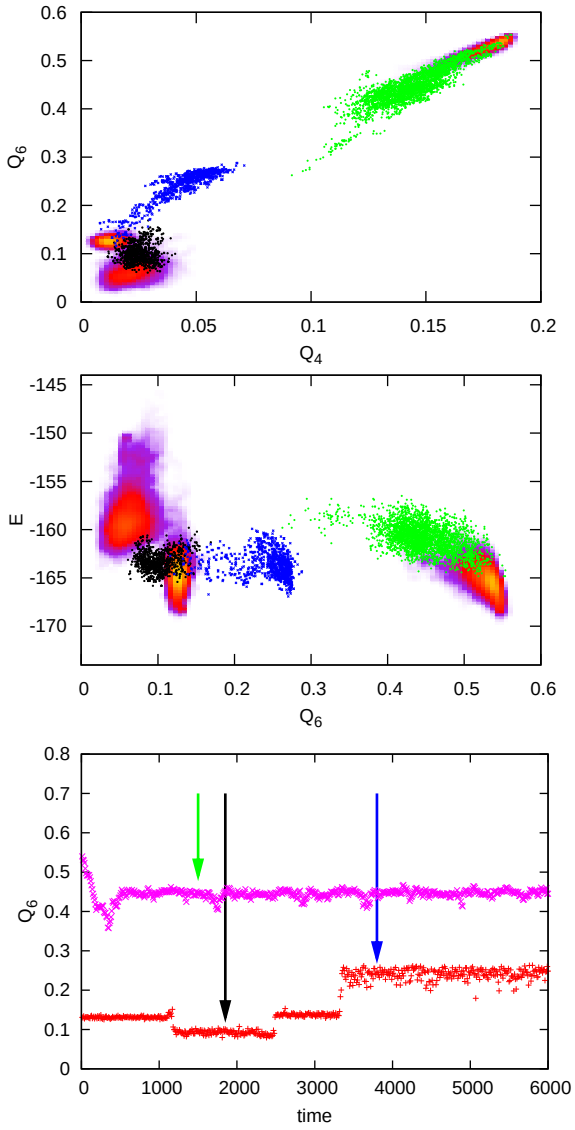

Figure 2.6: **Top and Center:** Positions of the clones starting from the ICOm and FCC minima in the (Q_4, Q_6) and (Q_6, E) plans at $T = 0.15$. The clones starting from the icosahedral basin first find the barrier between ICOm and ICOam (black symbols, $t = 1850$). They then fall back in the ICO basin before finding a path that points towards the FCC funnel (blue symbols, $t = 3500$). Starting from FCC, the 600 clones find a path that leads toward the icosahedral funnel (green symbols, $t = 1500$). **Bottom:** We plot Q_6 as a function of time for the clones starting from the ICOm basins (red symbols) and the FCC basin (magenta symbols). Arrows indicates the time at which the snapshots shown in the left and center panel are taken.

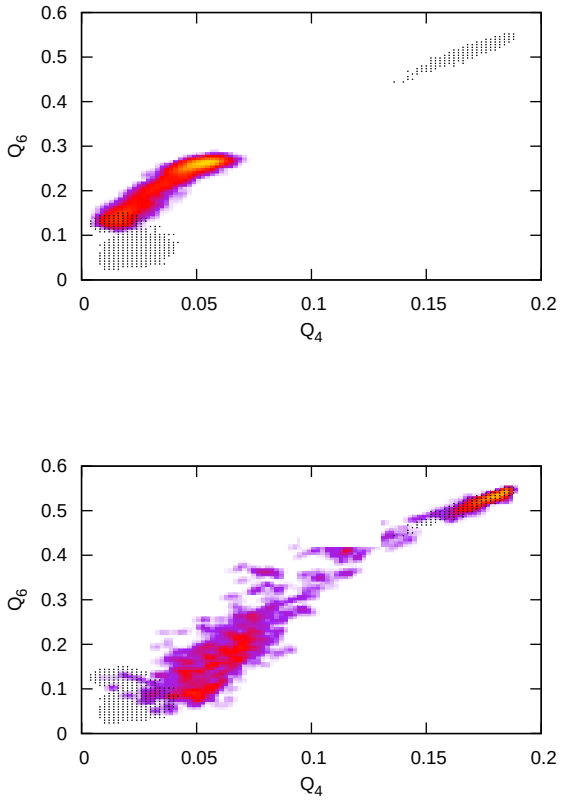

Figure 2.7: Histograms made at the end of short MD simulations at $T = 0.15$ started from the clones positions at the times indicated by the green and blue arrows in figure 2.6. The gray-dotted regions correspond to the equilibrium MD simulations of the three basins ICOm, ICOam and FCC. **Top**: MD simulations started from the stationary structures found by the clones in the ICO funnel fall either back into the ICO basin or in a metastable basin around $(Q_4, Q_6) = (0.05, 0.3)$ that corresponds to an amorphous structure at the entrance of the ICO funnel. **Bottom**: The clones starting from the stable structure found in the FCC funnel fall either back in the FCC basin, or in a faulty FCC metastable state (blue rectangle) or in the ICO funnel. Both structures thus correspond to reaction paths.

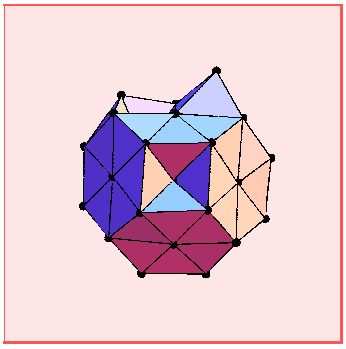

Figure 2.8: Position of the surface atoms of a clone that has fallen in the faulty FCC configuration after the short MD. This figure was made using a Mathematica Spreadsheet that can be downloaded at $http://www-wales.ch.cam.ac.uk/\ wales/make_frames.nb$.

evolution of the transition current, this means that there are more and more metastable states for the clone dynamics.

Starting from the ICOm basin with 600 clones and $\gamma\delta t = 10^{-3}$, we once again locate the barrier between ICOm and liquid-like phase ICOam. At this temperature this barrier is long-lived and we do not locate the one previously found at $T = 0.15$ that points toward the entrance of the icosahedral funnel.

Starting from the FCC basin with $\gamma\delta t = 0.02$, the 600 clones find several barriers that constitute a multi-step reaction path toward the icosahedral funnel. Once again, the larger the friction the longer the clones spend on intermediate barriers. Note however that the width of the clones distribution in the configuration space is of order $\sqrt{\gamma T}$ [13], so that for very large friction these clouds start to cover several barriers at the same time and their dynamics can be affected by this effect. The position of the clones corresponding to the successive metastable barriers are shown in figure 2.9. Note that the typical times needed for locating the barriers are of the order of 10^3, that is *seven orders of magnitude smaller* than the reaction times between ICOm and FCC, which is of the order of 10^{10}. [37]

Running short MD simulations starting from the clone positions on the barriers and constructing the corresponding histograms reveals various intermediate metastable basins in the ICO and FCC funnels (see figure 2.10). The fact that Q_4 and Q_6 are not good reaction coordinates is confirmed in this figure: the first plateau (green points on figure 2.9) seems to be *after* the faulty configuration when going from the FCC funnel to the icosahedral one but the MD starting from this barrier falls into the faulty configuration and the FCC basin, which seems to indicate that this barrier is a reaction state between the FCC and the faulty configuration. There is then a second barrier between the faulty FCC and the ICO funnel (blue dots in figure 2.9). A last barrier leads to the amorphous region that separates the liquid-like phase and ICOm minimum. Note that in these regions the

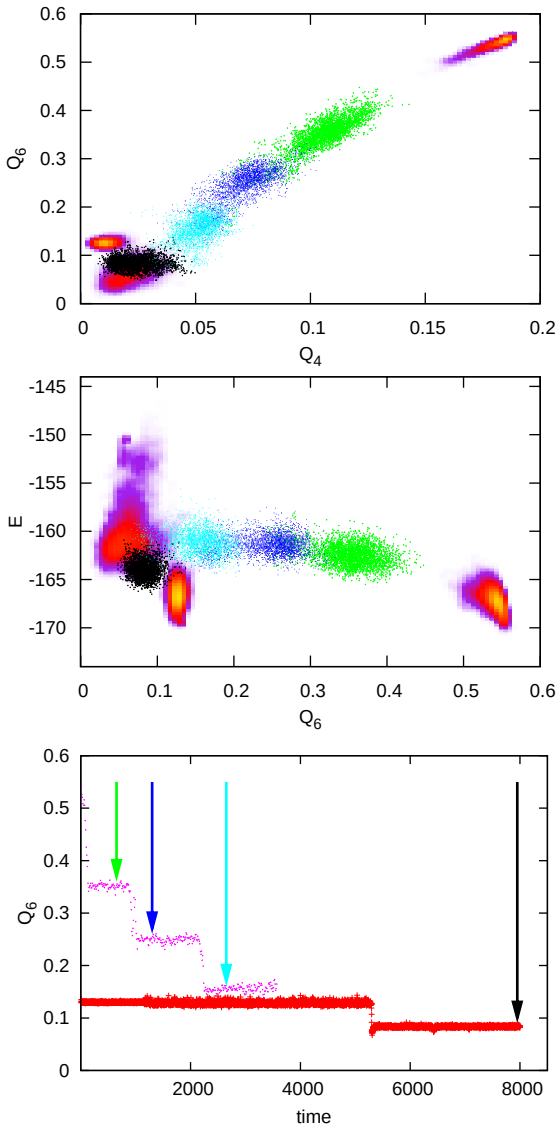

Figure 2.9: **Top and Center**: Positions of the clones starting from the ICOm and FCC minima in the (Q_4, Q_6) and (Q_6, E) plans at $T = 0.12$. The clones starting from ICO find the barrier between ICOm and ICOam (black symbols, $t = 8000$). Starting from FCC, the clones find a succession of barriers that leads toward the icosahedral funnel (green symbols at $t = 650$, blue symbols at $t = 1300$ and cyan symbols at $t = 2650$). **Bottom:** We plot Q_6 as a function of time for the clones starting from the ICOm basins (red symbols) and the FCC basin (magenta symbols).

MD simulations are not very helpful because the transition between ICOm and ICOam has an entropic nature so that it is difficult to relax into the basins. The clones, however, successfully identify the barrier between these two states.

2.4.2.5 $T = 0.19$

This temperature is very close to the transition between ICO and liquid-like phase. As shown by free-energy studies, the barrier between the FCC and the ICO funnels is very low and the FCC basin is rather unstable. [27] Clones starting from the FCC basin do not stabilize on any structure because there is no proper 'rare barrier' and MD simulations starting from FCC immediately falls into the icosahedral funnel. [27]

Starting 100 clones from the ICO basin at $\gamma\delta t = 0.01$, they rapidly find a barrier connecting to the liquid-like phase. Later on, activated events lead the clones to locate a reaction path leading towards the FCC funnel. Starting MD from this barrier show that the clones relax into the FCC and ICO funnel.

As mentioned above, it is hard for the clones to stabilize because the FCC funnel is barely metastable and the barrier crossed while going from FCC to ICO is rather flat at this temperature. It is thus quite surprising that they nevertheless manage to do so while starting from the ICO basin. If one starts from the FCC funnel, the clones almost immediately fall into the ICO funnel and then from there can locate the barrier again, but we were not able to stabilize the barrier when coming from the FCC basin. This might be due to the fact that clones stabilize reactions that take place on long time-scale (ICO→FCC), but not short-time relaxations (FCC→ICO).

2.4.2.6 $T = 0.05$: annealing the cloned system

If one starts at such a low temperature from one of the various metastable basins, the clones remain trapped for a time longer than the simulation time. One can however use a temperature annealing to locate the barriers. If one starts the cloning simulation at $T = 0.12$ or higher, it is quite easy, as we saw above, to localize the barriers. The temperature can then be decreased to $T = 0.05$ and the clones remains on the structure that were localized at a higher temperature (see figure 2.12).

2.5 Conclusions

The algorithm we have discussed in this paper may be characterized as one that simulates the evolution in time of the current distribution, rather than that of the configuration. Because the time for the escape current to be established is often much smaller than the passage time itself, the method is able to find the transition paths very efficiently.

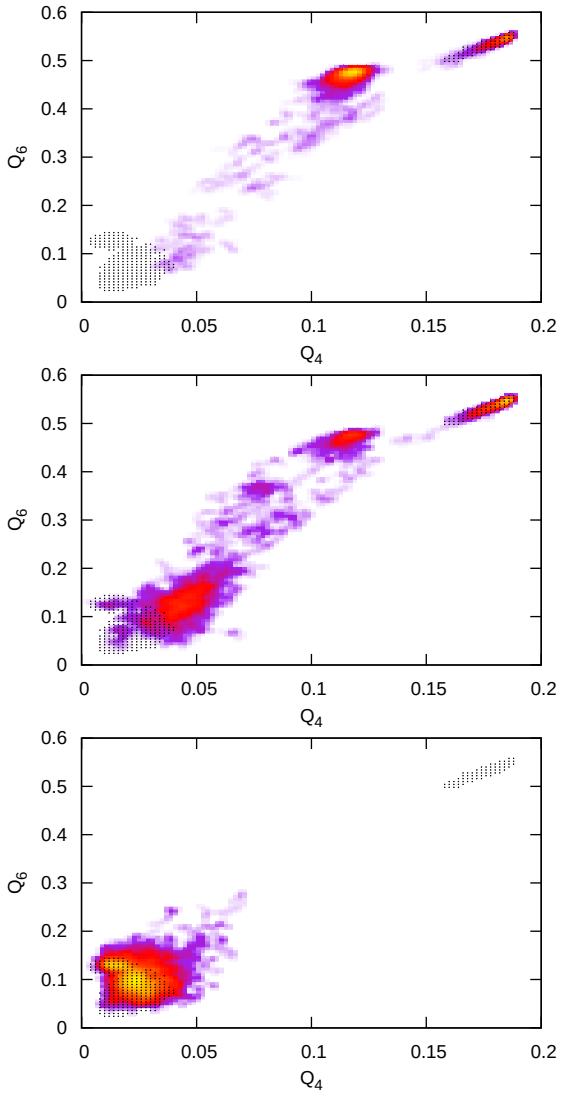

Figure 2.10: The color codes correspond to MD simulations at $T = 0.12$ started on the green (left), blue (center) and black (right) arrows in figure 2.9. **Top:** Starting from the first stationary structure found in the FCC funnel, the clones relaxes mostly in the FCC basin and in the faulty FCC configuration shown in 2.7. **Center** The second barrier is close to the commitor between the ICO and the FCC funnel: the clone population relaxes almost equally in both funnel (57% of the clones fall back in the icosahedral funnel while 43% enter the fcc funnel). **Bottom** Clones started from the barrier between ICOm and ICOam populate both basins. Note that the relaxation is much slower than for the other barrier because of the entropic nature of this barrier.

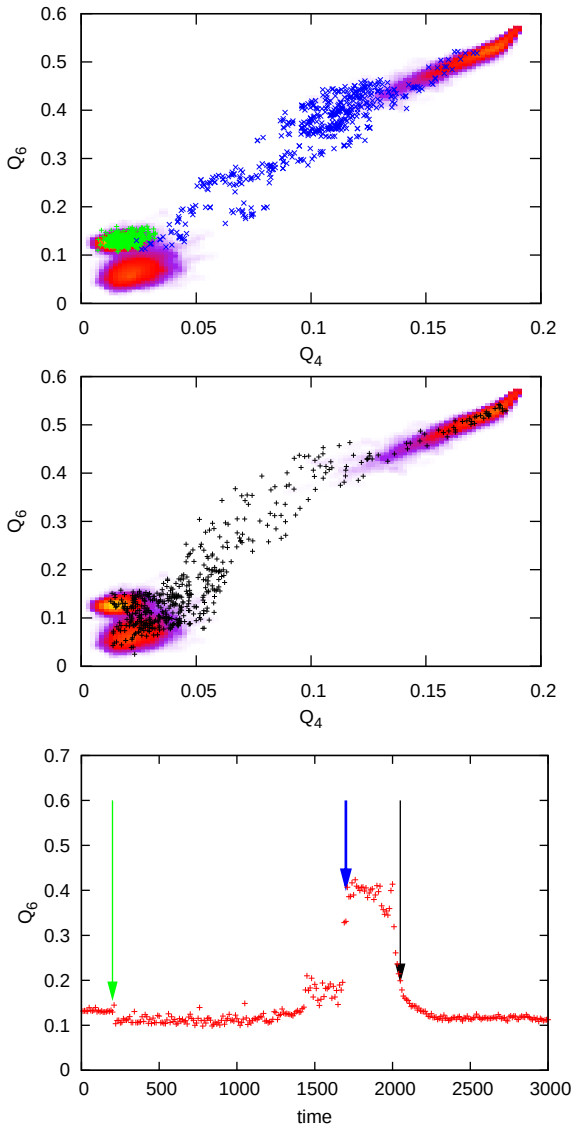

Figure 2.11: **Top**: 100 Clones are started at $T = 0.19$ in the ICOm basin where they spend some time (first first time steps after $t = 200$, green dots) before locating the barrier toward the FCC funnel (first five time steps after $t = 1700$, blue crosses). **Center:** When the clones have found the barrier ($t = 2000$) a standard MD starts and relaxes as it should into the two funnels (black dots, five first snapshots after $t = 2050$). **Bottom:** Evolution of $Q_6(t)$. The cloning is stopped at $t = 2000$ and a normal MD follows.

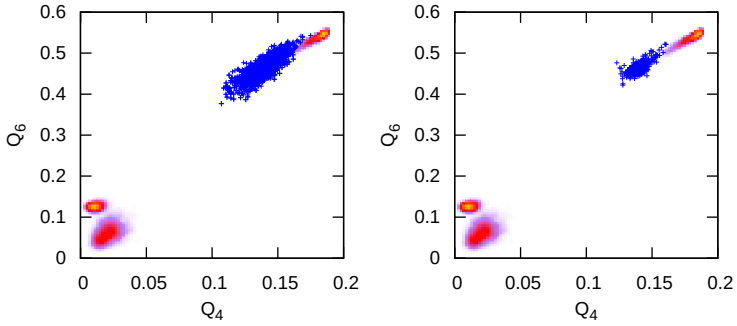

Figure 2.12: **Left**: Result of a simulation run at T=0.12 with 600 clones, starting from the FCC minimum, with $\gamma\delta t = 0.6$ **Right:** Starting from the end point of the simulations at T=0.12, we run a standard cloning simulation at $T = 0.05$. After a time $t = 1790$ the 600 clones are still on the structure that had localized at $T = 0.12$, which is thus very stable.

The method has several attractive features:

i) It does not require any previous knowledge of the relevant reaction coordinates. On the other hand, if an approximation of the reaction path is known *a priori*, one may always start the clones along this path, and they will populate the true current distribution in a shorter time.

ii) Because the target of the dynamics is the reaction path distribution itself, one may perform simulated annealing in path space: first populating the reaction path corresponding to relatively high temperature, and then refining it to the lower, target temperature. Repeated annealing can also be used to locate several competing barriers in system with multiple reaction mechanisms.

iii) The reaction current vanishes between mutually thermalized regions. [**?**] This is why at longer times, the system converges to the barriers that take longer to cross, *irrespective of whether they are of entropic or energetic nature*. This may be an advantage in cases in which the energy landscape is not in itself dominant, but rather the multiplicity of paths dominates.

iv) The construction of the transition current and the cloning algorithm also applies for non-equilibrium systems where the forces derive locally, but not globally from a potential, such as a system with leads at the edges having a potential difference. Reaction paths between non-equilibrium metastable states, which cannot be described in term of a free energy, may be studied in the same way. The only difference is that the average (2.48) does not vanish in the long time limit and converges instead to the steady-state transition current.

Note that since the method does not require the knowledge of the reaction coordinate, it could be used efficiently in systems with competing reactions where one does not

know *a priori* the end points of the reaction paths. This would for instance be particularly interesting when studying the crystallization of suspensions of oppositely charged colloids. [46, 47]

In principle, the reaction time may be expressed directly in terms of the (unnormalized) reaction current. It may also be recovered from the weights carried by the clones, which may possibly be achieved from importance sampling in a Lyapunov-weighted ensemble of trajectories. [48] However, the method, as it stands does not allow one to calculate the reaction *time* with great precision, due to the exponential nature of the timescale.

Further work is required in this direction, and we will therefore approach the problem of reaction constants determination in the next chapter.

Chapter 3

Lyapunov-biased Transition Path Sampling

Contents

3.1 Introduction . . . 43
3.2 Lyapunov Exponents in dynamical systems . . . 45
3.2.1 Continuous time dynamics . . . 45
3.2.2 Discrete dynamics and numerical applications: state of the art . . . 46
3.2.3 Hamiltonian dynamics . . . 49
3.2.4 Maximum local Lyapunov numbers . . . 51
3.2.5 Lyapunov indicator for dynamical trajectories . . . 53
3.3 Transition path sampling with a Lyapunov bias . . . 54
3.3.1 General theory for deterministic TPS . . . 54
3.3.2 Lyapunov biased TPS: shooting and shifting algorithms . . . 56
3.4 Reaction-rate constants calculation . . . 61
3.4.1 Rate constants theory . . . 61
3.4.2 Rate constants with biased sampling and *waste-recycling* . . . 63
3.4.3 Unbiasing rate constants: the MBAR algorithm . . . 64
3.5 Numerical results: LJ_{38} . . . 66
3.5.1 LJ_{38} cluster . . . 66
3.5.2 FCC-ICO reactive paths . . . 67
3.5.3 FCC-ICO reaction constants . . . 72
3.6 Conclusion . . . 79

3.1 Introduction

We propose in this chapter an efficient method to compute reaction rate constants of thermally activated processes occurring in many-body systems at finite temperature. The

method consists in two steps: first, trajectories are sampled using a transition path sampling (TPS) algorithm supplemented with a Lyapunov bias favoring diverging trajectories. This enhances the probability of observing rare reactive trajectories between stable states during relatively short simulations. Secondly, reaction constants are eventually estimated from the unbiased fraction of reactive trajectories, yielded by an appropriate statistical data analysis tool, the multistate Bennett acceptance ratio (MBAR) package.

In more details, we propose a transition path sampling algorithm where the fraction of reactive paths sampled is enhanced using an adequate bias that favours diverging trajectories. It is indeed possible to show [15, 48] that reactive paths we want to sample share important features with diverging trajectories observed in chaotic systems. Therefore, a suitable parameter that quantifies chaoticity properties of diverging trajectories can be exploited also to bias a path sampling algorithm aimed to reproduce reactive paths.

The main instrument proposed in the literature to quantify chaotic properties of dynamical systems is the evaluation of Lyapunov exponents, [52] that are usually employed to estimate the sensitivity of deterministic systems to small changes in initial conditions. For this feature, they have been widely studied, [68] both analytically and numerically, in hamiltonian as well as in nonlinear systems of small dimensions. Moreover, the use of Lyapunov exponents to characterize numerically phase transitions in finite size systems has been extensively explored in the past years, and many noticeable results have been obtained in the early 90's. [58, 59, 57, 78]

Resorting to Lyapunov exponents in order to achieve numerical ergodicity and localize saddles and transition paths has been done recently with the Lyapunov-weighted dynamics method proposed by Tailleur and Kurchan: [15] in this sampling scheme, a set of clones are copied or deleted depending on a probability weight computed from quantities related to Lyapunov exponents. After this work, the paper of Geiger and Dellago [48] has showed how to couple the chaoticity features of a dynamical system to a TPS technique for sampling deterministic trajectories, using an indicator for diverging trajectories borrowed from studies on planetary systems [61], the relative Lyapunov indicator (RLI).

Here, we present a chaoticity indicator different from RLI, and based on local Lyapunov numbers, that are quantities closely related to Lyapunov exponents. This indicator is used to introduce a bias in the path sampling scheme, thus obtaining a Lyapunov biased TPS method that will be in the sequel applied to complex many-body systems, like the well known optimization benchmark model LJ_{38}. Furthermore, we show how reaction rate constants can be recovered from biased TPS quantities, resorting to an appropriate statistical analysis to unbias reaction rate values computed in a Lyapunov biased TPS framework.

This chapter is organized as follows. In Sec. 3.2, we first recall the basic concepts of Lyapunov exponents for dynamical systems. We will then briefly review the use that

has been made of them in numerical algorithms to characterize phase transitions, or in importance sampling contexts. We then expose how to use local Lyapunov numbers in the context of a Transition Path Sampling to determine saddle points and reactive paths (Sec. 3.3). Reaction constants are computed from the fraction of reactive paths using the Bennett-Chandler approach [70] of population correlation functions and the standard TPS technique [3]; we also explain how unbiased reaction constants are recovered from a Lyapunov biased algorithm thanks to the multistate Bennett acceptance ratio [66] (MBAR) method (Sec. 3.4). Finally, numerical results concerning the application of our method to solid-solid structural transition in LJ_{38} and vacancy migration in α-Iron are presented (Sec. 3.5).

3.2 Lyapunov Exponents in dynamical systems

We briefly recap the theory of Lyapunov exponents, mainly following Ott [52]; then we propose a formulation allowing the use of these exponents in *importance sampling techniques*.

3.2.1 Continuous time dynamics

Let us consider a dynamical system with continuous dynamics, whose time evolution is given by a set of first order ordinary differential equations $\dot{\mathbf{x}} = \mathbf{F}(\mathbf{x})$. The state vector $\mathbf{x}(t)$ indicates the coordinates of the system in its complete phase-space representation at a given instant.

Let the system be at time $t = 0$ in an initial position $\mathbf{x}_0$, and let $\delta\mathbf{x}_0$ be a small perturbation applied to this initial state. The dynamics of such a perturbed system can then be denoted using a new state vector $\tilde{\mathbf{x}} = \mathbf{x} + \delta\mathbf{x}$, whose time evolution will be

$$\dot{\tilde{\mathbf{x}}} = \dot{\mathbf{x}} + \dot{\delta\mathbf{x}} = \mathbf{F}(\tilde{\mathbf{x}}) = \mathbf{F}(\mathbf{x} + \delta\mathbf{x}) \tag{3.1}$$

For a sufficiently small perturbation, it is possible to linearize the function $\mathbf{F}$ as

$$\mathbf{F}(\tilde{\mathbf{x}}) = \mathbf{F}(\mathbf{x} + \delta\mathbf{x}) = \mathbf{F}(\mathbf{x}) + D\mathbf{F}(\mathbf{x}) \cdot \delta\mathbf{x} + O(\delta\mathbf{x}^2) \tag{3.2}$$

Inserting Eq. (3.2) into Eq. (3.1), the time evolution of the perturbation at first order is

$$\dot{\delta\mathbf{x}} = D\mathbf{F}(\mathbf{x}) \cdot \delta\mathbf{x} \tag{3.3}$$

where $D\mathbf{F}(\mathbf{x})$ is the *Jacobian matrix* of $\mathbf{F}$.

The continuous time evolution of the perturbation $\delta\mathbf{x}$, given by Eq. (3.3), has particular solutions of the kind $\delta\mathbf{x}(t) = \mathbf{e} \cdot \exp(\Lambda t)$, that transform Eq. (3.3) into an eigenvalue equation

$$D\mathbf{F}(\mathbf{x}) \cdot \mathbf{e} = \Lambda\mathbf{e} \tag{3.4}$$

where Λ is a scalar satisfying the characteristic polynomial $det\{D\mathbf{F}(\mathbf{x}) - \Lambda\mathbf{I}\} = 0$ and $\mathbf{e}$ is an eigenvector of the Jacobian matrix $D\mathbf{F}(\mathbf{x})$. For N-body hamiltonian systems, having $3N$ degrees of freedom, $\mathbf{x}(t)$ is a $6N$-dimensional state vector accounting for both the positions and momenta of the N particles, thus the Jacobian matrix $D\mathbf{F}(\mathbf{x})$ has $6N$ eigenvectors $\mathbf{e}_k$, each one corresponding to an eigenvalue Λ_k: the complete solution of Eq. (3.3) is then of the form

$$\delta\mathbf{x}(t) = \sum_k A_k \mathbf{e}_k \exp(\Lambda_k t) \tag{3.5}$$

with coefficients A_k defined by $\delta\mathbf{x}(0) = \sum_k A_k\mathbf{e}_k$ and where the eigenvalues Λ_k are the *Lyapunov exponents* of our system. Such eigenvalues can be real, or pairs of complex conjugate numbers. In the case of complex conjugate pairs of eigenvalues $\Lambda_j = \Lambda^*_{j+1} = \sigma_j - i\omega_j$, with σ_j and ω_j real numbers, one can replace the two corresponding eigenvectors $\mathbf{e}_j$, $\mathbf{e}_{j+1}$ with two linear combinations of them, $\mathbf{g}_j$, $\mathbf{g}_{j+1}$. In this way, Eq. (3.5) can be rewritten [52] as $\delta\mathbf{x}(t) = \sum_k \tilde{A}_k\mathbf{g}_k \exp(\Lambda_k t)$, where coefficients $\tilde{\mathbf{A}}_k$ are all reals.

The stability properties of the system, expressed as its response to an initial small perturbation, are fully determined by the sign of the real part of the Lyapunov exponents. Indeed, the imaginary part of the Lyapunov exponents $\Im\{\Lambda_k\}$ does not affect the stability of the system, but only indicates if the dynamics is spiraling clockwise or counterclockwise. By contrast, for $\Re\{\Lambda_k\} > 0$ the perturbation in Eq. (3.5) diverges exponentially in time at a rate given by $\Re\{\Lambda_k\}$, so that the system is said to be *unstable*: this means that two trajectories initially separated by a small distance $\delta\mathbf{x}(0)$ evolve exponentially far away from each other. Otherwise, for $\Re\{\Lambda_k\} \leq 0$ the system is said to be *stable* and the distance between the reference and the perturbed trajectories vanishes (or remains constant) for long times.

3.2.2 Discrete dynamics and numerical applications: state of the art

In numerical applications, dynamics are discrete: the evolution of state vector $\mathbf{x}$ at time step n is described by a *mapping* $\mathbf{x}_{n+1} = \mathbf{M}(\mathbf{x}_n)$, where $\mathbf{M}$ is a matrix expressing the system evolution from one time step to the following. We give below the expression of Lyapunov exponents that will be evaluated numerically.

As for the continuous dynamics reported above, the time evolution of a small perturbation to the initial state vector (see Eqns. (3.1) - (3.3)) reads

$$\delta\mathbf{x}_{n+1} = D\mathbf{M}(\mathbf{x}_n) \cdot \delta\mathbf{x}_n \tag{3.6}$$

where $D\mathbf{M}(\mathbf{x}_n)$ is the Jacobian matrix of the map. Inserting in Eq. (3.6) particular solutions $\delta\mathbf{x}_n = \mathbf{e}[\Lambda]^n$, we again find an eigenvalue equation

$$D\mathbf{M}(\mathbf{x}_n) \cdot \mathbf{e} = \Lambda \cdot \mathbf{e}. \tag{3.7}$$

In the discrete case, the $6N$ eigenvalues Λ_k of $D\mathbf{M}(\mathbf{x}_n)$, solutions of Eq. (3.7), are called *Lyapunov numbers* rather the Lyapunov exponents, and trajectories are *unstable* for $|\Lambda_k| > 1$, and stable otherwise. We introduce the matricial product

$$D\mathbf{M}^n(\mathbf{x}_0) = D\mathbf{M}(\mathbf{x}_{n-1}) \cdots D\mathbf{M}(\mathbf{x}_0) \tag{3.8}$$

between the Jacobian matrices of the hamiltonian map at successive time steps, and we express the perturbation at time step n with respect to the initial perturbation $\delta\mathbf{x}_0$ as

$$\delta\mathbf{x}_n = D\mathbf{M}^n(\mathbf{x}_0) \cdot \delta\mathbf{x}_0$$

Defining with $\|\delta\mathbf{x}_0\|$ the Euclidean norm of $\delta\mathbf{x}_0$ in phase space, we introduce the *Lyapunov exponents* h, given the initial condition $\mathbf{x}_0$ and the initial perturbation orientation $\mathbf{u}_0 = \delta\mathbf{x}_0 / \|\delta\mathbf{x}_0\|$, as

$$h(\mathbf{x}_0, \mathbf{u}_0) = \lim_{n\to\infty} \frac{1}{n} \ln\left(\frac{\|\delta\mathbf{x}_n\|}{\|\delta\mathbf{x}_0\|}\right) = \lim_{n\to\infty} \frac{1}{n} \ln \|D\mathbf{M}^n(\mathbf{x}_0) \cdot \mathbf{u}_0\| \tag{3.9}$$

For a $6N$-dimensional hamiltonian map, there will be $6N$ Lyapunov exponents, usually ordered in literature from the largest to the smallest ($h_1 \geq \cdots \geq h_{6N}$). The term $\|D\mathbf{M}^n(\mathbf{x}_0) \cdot \mathbf{u}_0\|$ in Eq. (3.9) can be recasted in the form $|\mathbf{u}_0^\dagger [D\mathbf{M}^n(\mathbf{x}_0)]^\dagger D\mathbf{M}^n(\mathbf{x}_0) \cdot \mathbf{u}_0|^{1/2}$, where $\dagger$ denotes transpose and $[D\mathbf{M}^n(\mathbf{x}_0)]^\dagger D\mathbf{M}^n(\mathbf{x}_0)$ is a real nonnegative hermitian matrix having real and nonnegative eigenvalues. Moreover, as stated in [52], the Oseledec multiplicative ergodic theorem [67] guarantees the existence of the limits used in the definition of the Lyapunov exponents under very general circumstances.

The Lyapunov exponents are related to the aforementioned Lyapunov numbers as

$$\Lambda_k = \exp[h_k]\,. \tag{3.10}$$

From Eq. (3.9), we can also define *finite-time Lyapunov exponents*:

$$\bar{h}_n(\mathbf{x}_0, \mathbf{u}_0) = \frac{1}{n} \ln\left(\frac{\|\delta\mathbf{x}_n\|}{\|\delta\mathbf{x}_0\|}\right) = \frac{1}{n} \ln \|D\mathbf{M}^n(\mathbf{x}_0) \cdot \mathbf{u}_0\| \tag{3.11}$$

For long enough times, the greatest Lyapunov number Λ_1 will give the dominant contribution to the perturbation evolution, and the associated eigenvector $\mathbf{e}_1$ indicates the direction of maximum growth of the perturbation $\delta\mathbf{x}$.

We stress here that finite-time Lyapunov exponents are calculated for a given $\mathbf{x}_0$ and that, strictly speaking, their values do depend on the initial orientation $\mathbf{u}_0$. It is however shown that the largest exponent $h_1(\mathbf{x}_0, \mathbf{u}_0)$ is approximately independent of the choice of $\mathbf{u}_0$ in Hamiltonian ergodic systems[52, 40], while the complete spectra of finite-time exponents can be determined using specific numerical techniques. [65]

In numerical simulations, only finite-time Lyapunov exponents can be estimated, due to limited CPU time. To evaluate $\bar{h}_n$ from Eq. (3.11) we should compute the matricial

product of Eq. (3.8). For systems with many degrees of freedom, a calculation of this matrix product is not possible neither analytically nor numerically affordable, due to its computational cost. The solution most followed in literature consists of directly evaluating the quantity

$$\bar{h}_n(\mathbf{x}_0, \mathbf{u}_0) = \frac{1}{n} \ln \left(\frac{\|\delta \mathbf{x}_n\|}{\|\delta \mathbf{x}_0\|} \right) \tag{3.12}$$

given by the distance $\|\delta \mathbf{x}_n\|$ between two nearby dynamical trajectories, the first one started from the initial state $\mathbf{x}_0$ and the second one from the perturbed configuration $\tilde{\mathbf{x}}_0 = \mathbf{x}_0 + \delta \mathbf{x}_0$ after n time steps.

The use of Eq. (3.12) as a mean to evaluate finite-time Lyapunov exponents has two main drawbacks: the need of computing two trajectories to evaluate a single Lyapunov exponent, thus doubling computational cost, and the fact that values obtained for $\bar{h}$ can be sensitive to initial conditions, because of the dependence of the computed finite-time Lyapunov exponents from the choice of the orientation of initial perturbation, as recalled above.

Several numerical strategies have been proposed to bypass these problems. The tangent space method [65, 29] assigns to each state $\mathbf{x}_t$ of the trajectory started in $\mathbf{x}_0$ a vector $\mathbf{u}(\mathbf{x}_t)$. These vectors are computed from the local hessian matrix of the hamiltonian mapping, and their norms indicate the distance between the current trajectory and the perturbed one, i.e. $\mathbf{u}(t) \sim \delta \mathbf{x}(t)$. As these distances evolve exponentially (see Eq. (3.5)), the lengths of the vectors $\mathbf{u}$ can quickly diverge or vanish: a reorthonormalization of the set of the $\mathbf{u}$ is therefore required, for instance with a Gram-Smith algorithm. This method has been implemented in the literature [68], for instance in the context of Lyapunov weighted dynamics. [14, 13, 15] To make this algorithm independent of the choice of the first vector $\mathbf{u}(\mathbf{x}_0)$, one could integrate the equations of motion backward in time from $\mathbf{x}_0$ for a duration τ, and then reintegrate the evolution of $\mathbf{u}(\mathbf{x}_t)$ forward until $t = 0$ [69]. In this way, $\mathbf{u}(\mathbf{x}_0)$ would be automatically oriented in the direction of maximum growth. However, the duration τ should be long enough to ensure the loss of correlation between the orientation of $\mathbf{u}(\mathbf{x}_{-\tau})$ and $\mathbf{u}(\mathbf{x}_0)$, thus requiring the computation of long trajectories at sustained computational cost. [48, 69]

Another solution proposed in the definition of finite-time Lyapunov exponents is the Relative Lyapunov Indicator (RLI), elaborated by Sàndor *et al.* [61] in the context of planetary trajectories, and further used in a Lyapunov weighted path sampling scheme [48]. The main idea is to compare finite-time Lyapunov exponents $\bar{h}$ for trajectories starting very close, say in $\mathbf{x}_0$ and $\mathbf{x}_0 + \Delta \mathbf{x}_0$. The difference between finite-time exponents at time step n can be written as

$$\Delta \bar{h}_n(\mathbf{x}_0, \mathbf{u}_0) = \left| \bar{h}_n(\mathbf{x}_0 + \Delta \mathbf{x}_0, \mathbf{u}_0) - \bar{h}_n(\mathbf{x}_0, \mathbf{u}_0) \right| \tag{3.13}$$

and will in general undergo strong fluctuation, [61] which can be smoothed by an average

over $\mathcal{N}$ trajectory steps: in this way one defines the RLI as the quantity

$$R(\mathbf{x}_0, \mathbf{u}_0) = \frac{1}{\mathcal{N}} \sum_{i=1}^{\mathcal{N}} \Delta \bar{h}_i(\mathbf{x}_0, \mathbf{u}_0) = \frac{1}{\mathcal{N}} \sum_{i=1}^{\mathcal{N}} \left| \bar{h}_i(\mathbf{x}_0 + \Delta\mathbf{x}_0, \mathbf{u}_0) - \bar{h}_i(\mathbf{x}_0, \mathbf{u}_0) \right| \tag{3.14}$$

This average over the entire trajectory length reduces [61] the dependence of the computed finite-time Lyapunov exponents on the orientation of initial perturbation, but introduces an additional dependence on $\Delta\mathbf{x}_0$. Both finite-time Lyapunov exponents are calculated evaluating the distance between two trajectories evolving close to each other (instead of the matricial product of Eq. (3.8)): in terms of computational cost, four trajectories are computed to obtain a single RLI. Finally, its implementation in a TPS algorithm with shifting procedure (see below) can be rather complicated.

In the following, we propose a faster and orientation-independent way to evaluate the chaotic properties of hamiltonian systems, alternative to tangent space method and RLI, to be used in the path-sampling scheme described in Sec. 3.3.

3.2.3 Hamiltonian dynamics

We restrict our focus to systems with deterministic dynamics governed by an hamiltonian of the form $\mathcal{H} = \sum_{i=1}^{N} \frac{\mathbf{p}_i^2}{2m_i} + V(\mathbf{q})$. The time evolution of the state vector $\mathbf{x} = (\mathbf{q}, \mathbf{p})$ (also indicated as "hamiltonian flow" [68]) directly follows from Hamilton equations,

$$\dot{\mathbf{x}} = \begin{pmatrix} \mathbf{0} & \mathbf{G} \\ -\mathbf{I} & \mathbf{0} \end{pmatrix} \begin{pmatrix} \frac{\partial \mathcal{H}(\mathbf{q},\mathbf{p})}{\partial \mathbf{q}} \\ \frac{\partial \mathcal{H}(\mathbf{q},\mathbf{p})}{\partial \mathbf{p}} \end{pmatrix} \tag{3.15}$$

The evolution of a small perturbation of positions and momenta for a standard hamiltonian is given by

$$\delta\dot{\mathbf{x}} = \begin{pmatrix} \mathbf{0} & \mathbf{I} \\ -\frac{\partial^2 \mathbf{V}(\mathbf{q})}{\partial \mathbf{q} \partial \mathbf{q}} & \mathbf{0} \end{pmatrix} \delta\mathbf{x} \tag{3.16}$$

Let us discretize the hamiltonian dynamics in Eq. (3.15) with the velocity Verlet algorithm:

$$\begin{aligned} p_{i,n+1/2} &= p_{i,n} - \frac{1}{2} dt \cdot \frac{\partial V(\mathbf{q}_n)}{\partial q_{i,n}} \\ q_{i,n+1} &= q_{i,n} + \frac{dt}{m_i} p_{i,n+1/2} \\ p_{i,n+1} &= p_{i,n+1/2} - \frac{1}{2} dt \cdot \frac{\partial V(\mathbf{q}_{n+1})}{\partial q_{i,n+1}}. \end{aligned} \tag{3.17}$$

This algorithm is accurate to second order and numerically stable [71]. It will be used to generate dynamical trajectories in numerical applications.

The jacobian matrix for the velocity Verlet discretization reads

$$D\mathbf{M}(\mathbf{x}_n) = \begin{bmatrix} \mathbf{I} - \frac{dt^2}{2m}\mathbf{H}(\mathbf{x}_n) & dt\mathbf{G} \\ -\frac{dt}{2}\left\{\mathbf{H}(\mathbf{x}_n) + \mathbf{H}(\mathbf{x}_{n+1})\left[\mathbf{I} - \frac{dt^2}{2m}\mathbf{H}(\mathbf{x}_n)\right]\right\} & \mathbf{I} - \frac{dt^2}{2m}\mathbf{H}(\mathbf{x}_{n+1}) \end{bmatrix}. \tag{3.18}$$

In the upper right and bottom left blocks we introduced the $3N \times 3N$ inverse mass matrix $G_{ij} = \delta_{ij}/m_i$ and the hessian matrix of the potential energy $\mathbf{H}$ at states $\mathbf{x}_n$ and $\mathbf{x}_{n+1}$, respectively. Eq. (3.18) is derived recasting the velocity Verlet algorithm of Eq. (3.20) in the three following steps:

1. from $\mathbf{x}_n = (\mathbf{q}_n, \mathbf{p}_n)$ to $(\mathbf{q}_n, \mathbf{p}_{n+1/2})$

$$\begin{aligned} q_{i,n} &= q_{i,n} \\ p_{i,n+1/2} &= p_{i,n} - \frac{1}{2}dt \cdot \frac{\partial V(\mathbf{q}_n)}{\partial q_{i,n}} \end{aligned} \tag{3.19}$$

2. from $(\mathbf{q}_n, \mathbf{p}_{n+1/2})$ to $(\mathbf{q}_{n+1}, \mathbf{p}_{n+1/2})$

$$\begin{aligned} q_{i,n+1} &= q_{i,n} + \frac{dt}{m_i}p_{i,n+1/2} \\ p_{i,n+1/2} &= p_{i,n+1/2} \end{aligned} \tag{3.20}$$

3. from $(\mathbf{q}_{n+1}, \mathbf{p}_{n+1/2})$ to $(\mathbf{q}_{n+1}, \mathbf{p}_{n+1})$

$$\begin{aligned} q_{i,n+1} &= q_{i,n+1} \\ p_{i,n+1} &= p_{i,n+1/2} - \frac{1}{2}dt \cdot \frac{\partial V(\mathbf{q}_{n+1})}{\partial q_{i,n+1}} \end{aligned} \tag{3.21}$$

The jacobian matrices $D\mathbf{M}$ corresponding to steps 1, 2 and 3 are respectively

$$D\mathbf{M}^{(1)}(\mathbf{x}_n) = \left[\mathbf{I}_{6N} + dt \begin{pmatrix} \mathbf{0} & \mathbf{0} \\ -\frac{1}{2}\mathbf{H}(\mathbf{x}_n) & \mathbf{0} \end{pmatrix}\right] \tag{3.22}$$

$$D\mathbf{M}^{(2)}(\mathbf{q}_n, \mathbf{p}_{n+1/2}) = \left[\mathbf{I}_{6N} + dt \begin{pmatrix} \mathbf{0} & \mathbf{G} \\ \mathbf{0} & \mathbf{0} \end{pmatrix}\right] \tag{3.23}$$

$$D\mathbf{M}^{(3)}(\mathbf{q}_{n+1}, \mathbf{p}_{n+1/2}) = \left[\mathbf{I}_{6N} + dt \begin{pmatrix} \mathbf{0} & \mathbf{0} \\ -\frac{1}{2}\mathbf{H}(\mathbf{x}_{n+1}) & \mathbf{0} \end{pmatrix}\right] \tag{3.24}$$

and the product $D\mathbf{M}(\mathbf{x}_n) = D\mathbf{M}^{(3)}(\mathbf{q}_{n+1}, \mathbf{p}_{n+1/2})D\mathbf{M}^{(2)}(\mathbf{q}_n, \mathbf{p}_{n+1/2})D\mathbf{M}^{(1)}(\mathbf{q}_n, \mathbf{p}_n)$ gives the jacobian matrix of Eq. (3.18). The perturbation $\delta\mathbf{x}_{n+1}$ can now be evaluated with respect to $\delta\mathbf{x}_n$ using Eq. (3.6).

The jacobian matrix of Eq. (3.18) obtained with the velocity Verlet scheme of Eq. (3.20) contains the hessian matrices at steps n and $n+1$. Therefore, manipulations of $D\mathbf{M}(\mathbf{x}_n)$

results to be numerically expensive. A simpler expression for the jacobian matrix can be obtained from the less accurate Euler discretization algorithm: Eq. (3.15) becomes a set of *6N* coupled equations of motion

$$\begin{aligned} q_{i,n+1} &= q_{i,n} + dt \cdot \frac{p_{i,n}}{m_i} \\ p_{i,n+1} &= p_{i,n} - dt \cdot \frac{\partial V}{\partial q_{i,n}} \end{aligned} \tag{3.25}$$

where $i = 1, ..., 3N$, so that the jacobian matrix of the hamiltonian map reads

$$D\mathbf{M}(\mathbf{x}_n) = \left[\mathbf{I}_{6N} + dt \begin{pmatrix} \mathbf{0} & \mathbf{G} \\ -\mathbf{H}(\mathbf{x}_n) & \mathbf{0} \end{pmatrix} \right]. \tag{3.26}$$

The perturbation $\delta\mathbf{x}_n$ at each time step can be evaluated by inserting Eq. (3.26) in Eq. (3.6).

The difference between the jacobian matrix $D\mathbf{M}(\mathbf{x}_n)$ of Eq. (3.26) and the one of Eq. (3.18) consists in second order terms. However, it is numerically less expensive to manipulate the former then the latter, as $D\mathbf{M}(\mathbf{x}_n)$ of Eq. (3.26) requires to evaluate the hessian only at time step n. In the following, we will be interested in computing the eigenvalues of $D\mathbf{M}(\mathbf{x}_n)$, in order to obtain a bias favoring reactive trajectories (see below): this bias will be removed at the end, so it would be useless to spend CPU time to accurately evaluate the jacobian matrix. Therefore, accordingly to Ref. [58], we consider the Euler scheme (Eq. (3.25)) precise enough for our purposes, and we use the first order Euler discretization of Eq. (3.26) to compute $D\mathbf{M}(\mathbf{x}_n)$.

3.2.4 Maximum local Lyapunov numbers

Using the discretized hamiltonian dynamics given in Eq. (3.25), we proceed by computing at each time step the maximum local Lyapunov number [86] that is given by the largest eigenvalue of the Jacobian matrix $D\mathbf{M}(\mathbf{x}_n)$ (Eq. (3.26)).

The $6N$ eigenvalues Λ_n of $D\mathbf{M}(\mathbf{x}_n)$, computed at time step n, can be obtained from the secular equation

$$P(\Lambda_n) = det\left\{\Lambda_n \mathbf{I} - D\mathbf{M}(\mathbf{x}_n)\right\} = 0. \tag{3.27}$$

whose solutions are *3N* pairs of eigenvalues Λ_n of $D\mathbf{M}(\mathbf{x}_n)$, because of the simplectic properties of the hamiltonian mapping matrix $\mathbf{M}$ [52]. These eigenvalues are given by the expression [58]

$$\Lambda^{\pm}_{j,n} = 1 \pm dt\sqrt{-\lambda_{j,n}} \quad \forall j = 1, \ldots, 3N \tag{3.28}$$

where the $\lambda_{j,n}$ correspond to the eigenvalues of the mass-weighted Hessian $\mathbf{H}'(\mathbf{x}_n)$ of components

$$\mathbf{H}'_{ij}(\mathbf{x}_n) = \frac{1}{\sqrt{m_i m_j}} \frac{\partial^2 V(\mathbf{x}_n)}{\partial q_i \partial q_j}. \tag{3.29}$$

The result of Eq. (3.28) is derived below. We first rewrite the secular equation (3.27) as

$$P(\mu_n) = det\left\{\mu_n \mathbf{I} - D\tilde{\mathbf{M}}(\mathbf{x}_n)\right\} = 0 \tag{3.30}$$

where $\mu_n = \left(\frac{\Lambda_n - 1}{dt}\right)$ and

$$D\tilde{\mathbf{M}}(\mathbf{x}_n) = \left[\begin{pmatrix} \mathbf{0} & \mathbf{I} \\ -\mathbf{D}(\mathbf{x}_n) & \mathbf{0} \end{pmatrix}\right] \tag{3.31}$$

The lower-left block matrix $\mathbf{D}(\mathbf{x}_n)$ is a $3N \times 3N$ diagonal matrix whose elements are the eigenvalues $\lambda_{j,n}$ of the mass-weighted hessian $\mathbf{H}'$ just mentioned above, at time step n. The solution to Eq. (3.30) is obtained by Laplace expansion of the matrix $\mu_n \mathbf{I} - D\tilde{\mathbf{M}}(\mathbf{x}_n)$ with respect to the first row. Since this matrix is composed of four diagonal blocks of $3N \times 3N$ elements, one finds the recursive expression

$$\begin{aligned} P_{3N}(\mu) &= \mu^2(-1)^{6N} P_{3N-1}(\mu) + \lambda_{3N}(-1)^{6N+1} P_{3N-1}(\mu) \\ &= (\mu^2 - \lambda_{3N}) P_{3N-1}(\mu) \end{aligned} \tag{3.32}$$

$P_{3N-1}(\mu)$ are secular equations for the minors of matrix $\mu_n \mathbf{I} - D\tilde{\mathbf{M}}(\mathbf{x}_n)$, where each minor is composed by four blocks of size $(3N-1) \times (3N-1)$. From Eq. (3.32) and the fact that $P_1(\mu) = (\mu^2 - \lambda_1)$, we infer by induction

$$P_{3N}(\mu) = \prod_{j=1}^{3N} \left(\mu^2 - \lambda_j\right). \tag{3.33}$$

Besides, using the definition of μ_n, one immediately recovers Eq. (3.28). Eq. (3.32) being valid at every time step, subscript n has been omitted in $\lambda_{j,n}$.

Hence, Eq. (3.28) shows that at each time step n the jacobian eigenvalues $\Lambda_{j,n}$, i.e. the local Lyapunov numbers, depend on the potential energy surface through the hessian eigenvalues $\lambda_{j,n}$: unstable configurations $\mathbf{x}_n$, such as saddle points are characterized by negative $\lambda_{j,n}$, and correspond to real and positive local Lyapunov numbers $\Lambda_{j,n}$. Conversely, stable states have positive $\lambda_{j,n}$ and imaginary local Lyapunov numbers with unitary real part. In the following path sampling scheme of Sec. 3.3 we neglect the imaginary part of $\Lambda_{j,n}$ given by stable states. This is not an issue because, as mentioned at the end of Sec. 3.2.1, to characterize unstable dynamics which we are interested in it is sufficient to determine real and positive (global) Lyapunov exponents, and the imaginary part of the jacobian eigenvalues $\Lambda_{j,n}$ can be neglected.

At each time step n, the most negative eigenvalue of the hessian matrix λ_n^{min} indicates the direction of greatest instability on the potential energy surface and gives the eigenvalue of the Jacobian matrix $D\mathbf{M}(\mathbf{x}_n)$ with the largest real part. This maximum local Lyapunov number at that time step reads

$$\Lambda_n^{MAX} = 1 + dt\sqrt{\max(0, -\lambda_n^{min})} \tag{3.34}$$

Eq. (3.34) entails $\Lambda_n^{MAX} = 1$ for stable configurations, where all λ are positive, and $\Lambda_n^{MAX} > 1$ for unstable configurations having a negative spectra. Hence, Eq. (3.34) can be used to compute the maximum local Lyapunov number for each time step of an hamiltonian dynamics.

The diagonalization of the hessian matrix $\mathbf{H}$ in order to find its eigenvalues λ_n can be computationally very expensive for systems with a large number of degrees of freedom. One efficient solution to evaluate Λ_n^{MAX} consists in extracting only the lowest eigenvalue λ_n^{min} using the Lanczos algorithm [62]. This iterative algorithm finds extremal eigenvalues of any matrix with a reduced computational cost, diagonalizing only a submatrix of the initial one (see for example Appendix D or Ref. [53] for details). As pointed out in Ref. [**?**], a 15×15 Lanczos submatrix is sufficient to detect negative eigenvalues. Moreover, it is possible to decrease the submatrix size to as little as 4×4 by verifying at each iteration that the Lanczos solution is stable; if not, repeat the calculation until a the solution is converged. Hence, the most negative eigenvalue, corresponding to the most unstable direction of the potential energy surface at a give system position in the phase-space, instant can be extracted in a few iterations. This is the numerical method we will apply in the following to evaluate Λ_n^{MAX}.

3.2.5 Lyapunov indicator for dynamical trajectories

A dynamical trajectory is defined as an ordered sequence of states in phase space separated by a small time increment δt, and denoted as $\mathbf{z} = \{\mathbf{x}_0, ..., \mathbf{x}_\tau\}$, i.e. a path of total length τ composed by $\mathcal{N} = \frac{\tau}{\delta t} + 1$ state vectors. We introduce a *Lyapunov indicator* for path $\mathbf{z}$

$$L(\mathbf{z}) = \frac{1}{\mathcal{N}} \ln \prod_{n=1}^{\mathcal{N}} \Lambda_n^{MAX} \tag{3.35}$$

given by the average of the maximum Lyapunov number of Eq (3.34) over the whole trajectory.

The verification of the difference between finite-time Lyapunov exponents estimated by RLI or tangent space method and $L(\mathbf{z})$ from Eq. (3.35) is not the scope of this work. We stress instead that the maximum local Lyapunov number, being based on the hessian spectra λ, is strictly related to the topological properties of the potential energy surface, thus gives, through the indicator proposed in Eq. (3.35), local information on the stable or unstable configurations sampled in phase space by a given trajectory. Hencefore, we consider this Lyapunov indicator suitable for importance sampling techniques.

The idea of evaluating the largest local Lyapunov exponent has been proposed by Hinde *et al.* [58] in the slightly different context of studying the dependence of the Kolmogorov entropy on the potential energy surface of small Lennard-Jones clusters (see Appendix C). In Ref. [58], the Lyapunov exponents derived from the eigenvalues of the jacobian matrix of

the hamiltonian mapping are summed over trajectories of different lengths, thus obtaining - using Pesin's theorem [85] - an estimation of the Kolmogorov entropy. This approach to compute finite-time Lyapunov exponents has been shown to be quite succesfull, as it still furnishes enough information to quantify the degree of instability of phase space trajectories, thus supporting that evaluating the global Lyapunov exponent from local Lyapunov numbers allow to correctly reproduce the chaotic properties of the system.

3.3 Transition path sampling with a Lyapunov bias

The idea of sampling the phase space of a many-body system through paths generated by molecular dynamics, using the Metropolis algorithm, was introduced first by Pratt [64], and then further developed by Dellago and coworkers. [3, 63, 54] The approach was called transition path sampling (TPS). Herein, we briefly describe the TPS method, prior to explaining how to bias TPS with the Lyapunov indicator of Eq. (3.35).

3.3.1 General theory for deterministic TPS

Each path $\mathbf{z}$ is equipped with the probability density

$$\mathcal{P}[\mathbf{z}] = \rho(\mathbf{x}_0) \prod_{i=0}^{\tau/\delta t-1} p\left(\mathbf{x}_{i\delta t} \to \mathbf{x}_{(i+1)\delta t}\right) \tag{3.36}$$

where $\rho(\mathbf{x}_0) = Z^{-1}\exp(-\beta\mathcal{H}(\mathbf{x}_0))$ is the canonical distribution at inverse temperature β from which the initial configuration is selected, while the quantity $p\left(\mathbf{x}_{i\delta t} \to \mathbf{x}_{(i+1)\delta t}\right)$ is the probability to transit from configuration $\mathbf{x}_{i\delta t}$ to configuration $\mathbf{x}_{(i+1)\delta t}$ using a given propagation algorithm.

Let us define two main equilibrium basins on the free energy landscape, and indicating them as A (reactants) and B (products). The probability of observing a path starting from the A basin[1] is

$$\mathcal{P}_A[\mathbf{z}] = \frac{h_A(\mathbf{x}_0)\mathcal{P}[\mathbf{z}]}{Z_A} \tag{3.37}$$

where the indicator function h_Ω is defined for a generic state Ω as

$$h_\Omega(\mathbf{x}) = \begin{cases} 1 & \mathbf{x} \in \Omega \\ 0 & \mathbf{x} \notin \Omega \end{cases}$$

[1] The probability of observing reactive paths between basins A and B is written as

$$\mathcal{P}_{AB}[\mathbf{z}] = \frac{h_A(\mathbf{x}_0)\mathcal{P}[\mathbf{z}]\,h_B(\mathbf{x}_\tau)}{Z_{AB}}$$

with a partition function

$$Z_{AB} = \int \mathcal{D}z h_A(\mathbf{x}_0)\mathcal{P}[\mathbf{z}]\,h_B(\mathbf{x}_\tau)$$

.

and the trajectory-space partition function is defined as

$$Z_A = \int \mathcal{D}\mathbf{z}\, h_A(\mathbf{x}_0)\mathcal{P}\left[\mathbf{z}\right]. \tag{3.38}$$

Our approach in the following is based on deterministic dynamics associated with Newton's equation of motion, whose evolution (Eq. (3.15)) corresponds to a set of differential equations $\dot{\mathbf{x}} = \Gamma(\mathbf{x})$, see Appendix A. Resorting to a *temporal propagator* $\mathbf{x}_t = \phi_t(\mathbf{x}_0)$ (i.e. the aforementioned hamiltonian mapping) associated to this dynamics, the conditional probability of being in $\mathbf{x}_{t+\delta t}$, given the configuration $\mathbf{x}_t$ at the previuos time step, is

$$P_{cond}\left(\mathbf{x}_t \to \mathbf{x}_{t+\delta t}\right) = \delta\left[\mathbf{x}_{t+\delta t} - \phi_{\delta t}(\mathbf{x}_t)\right] \tag{3.39}$$

Taking P_{cond} for p in Eq. (3.36), the path probability expressed in Eq. (3.37) reads

$$\mathcal{P}_A\left[\mathbf{z}(\tau)\right] = \exp(-\beta\mathcal{H}(\mathbf{x}_0))\frac{h_A(\mathbf{x}_0)}{Z_A}\prod_{i=0}^{\tau/\delta t-1}\delta\left[\mathbf{x}_{(i+1)\delta t} - \phi_{\delta t}(\mathbf{x}_{i\delta t})\right] \tag{3.40}$$

The entire trajectory is therefore determined by the initial configuration $\mathbf{x}_0$, distributed according to

$$\rho_A(\mathbf{x}_0) = \frac{\exp(-\beta\mathcal{H}(\mathbf{x}_0))h_A(\mathbf{x}_0)}{Z_A}. \tag{3.41}$$

The distribution $\mathcal{P}_A$ is approximated by a Markov chain of M steps constructed by importance sampling, by means of the Metropolis algorithm. The sampling is done in the following way: at Markov chain step m, starting from the current path $\mathbf{z}^m$, a trial path $\tilde{\mathbf{z}}$ is generated with the probability distribution P_{gen}. Then, the trial path is accepted with a probability P_{acc} and added to the Markov chain as $\mathbf{z}^{m+1} = \tilde{\mathbf{z}}$; otherwise, if the trial path is rejected, $\mathbf{z}^{m+1} = \mathbf{z}^m$. To ensure the convergence of the Markov chain towards the equilibrium distribution $\mathcal{P}_A$, we impose that the probability $\pi\left[\mathbf{z} \to \mathbf{z}'\right]$ to transit from a path $\mathbf{z}$ to a different path $\mathbf{z}'$ satisfies the detailed balance equation

$$\mathcal{P}_A\left[\mathbf{z}\right]\pi\left[\mathbf{z} \to \mathbf{z}'\right] = \mathcal{P}_A\left[\mathbf{z}'\right]\pi\left[\mathbf{z}' \to \mathbf{z}\right] \tag{3.42}$$

Taking account of the generating and acceptance probabilities P_{gen} and P_{acc}, the transition probability π reads

$$\pi\left[\mathbf{z} \to \mathbf{z}'\right] = \sum_{\tilde{\mathbf{z}}} P_{gen}\left[\mathbf{z} \to \tilde{\mathbf{z}}\right]\left\{\delta(\tilde{\mathbf{z}} - \mathbf{z}')P_{acc}\left[\mathbf{z} \to \tilde{\mathbf{z}}\right] + \delta(\tilde{\mathbf{z}} - \mathbf{z})(1 - P_{acc}\left[\mathbf{z} \to \tilde{\mathbf{z}}\right])\right\} \tag{3.43}$$

where δ is the delta distribution and we allow for the possibility that $\mathbf{z}'$ is either the old path $\mathbf{z}$ or the proposed path $\tilde{\mathbf{z}}$. The acceptance probability can be constructed from Eqs. (3.42) and (3.43) as the Metropolis acceptance

$$P_{acc}\left[\mathbf{z} \to \tilde{\mathbf{z}}\right] = \min\left\{1, \frac{\mathcal{P}_A\left[\tilde{\mathbf{z}}\right]P_{gen}\left[\tilde{\mathbf{z}} \to \mathbf{z}\right]}{\mathcal{P}_A\left[\mathbf{z}\right]P_{gen}\left[\mathbf{z} \to \tilde{\mathbf{z}}\right]}\right\}. \tag{3.44}$$

that is widely used in numerical simulations, as it has the main advantage of maximizing P_{acc}.

3.3.2 Lyapunov biased TPS: shooting and shifting algorithms

We now introduce a bias in the TPS algorithm in order to favor the sampling of reactive trajectories. The bias is proportional to the Lyapunov indicator $L(\mathbf{z})$, obtained in Eq. (3.35) by summing the values of the maximum local Lyapunov number computed at each time step along path $\mathbf{z}$:

$$L(\mathbf{z}) = \frac{1}{\mathcal{N}} \sum_{n=1}^{\mathcal{N}} \log \Lambda_n^{MAX} \tag{3.45}$$

The Λ_n^{MAX} are the eigenvalues of the jacobian matrix, and are calculated using the Lanczos algorithm (see Sec. 3.2.4). We use this indicator to modify the probability weight of path $\mathbf{z}$ by multiplying the path probabilities $\mathcal{P}_A(\mathbf{z})$ by $\exp\{\alpha L(\mathbf{z})\}$: each path $\mathbf{z}$ constrained to start in a reactant basin A is equipped with a probability density

$$\mathcal{P}_A^{\alpha}(\mathbf{z}) = \frac{1}{Z_A^{\alpha}} \exp\{\alpha L(\mathbf{z}) - \beta \mathrm{H}(\mathbf{z})\} \, \varphi_A^{\alpha}(\mathbf{x}_0) \tag{3.46}$$

where Z_A^{α} is the partition function on the biased trajectory ensemble, and function $\varphi_A^{\alpha}(\mathbf{x}_0)$ is an additional term linking the initial state $\mathbf{x}_0$ of the path to state $\mathbf{x}_A$. Different choices for φ_A^{α} are possible, for instance $\varphi_A^{\alpha}(\mathbf{x}_0) = h_A(\mathbf{x}_0)$, where h_A is an indicator function on A, such that

$$h_A(\mathbf{x}) = \begin{cases} 1 & \mathbf{x} \in A \\ 0 & \mathbf{x} \notin A \end{cases}, \tag{3.47}$$

or

$$\varphi_A^{\alpha}(\mathbf{x}_0) = \exp\left\{-\frac{1}{2}\kappa^{\alpha}(\mathbf{x}_0 - \mathbf{x}_A)^2\right\} h_A(\mathbf{x}_0) \tag{3.48}$$

that accounts for having a tunable spring of stiffness κ^{α} linking the origin of path $\mathbf{z}$ to state A. In this last case, the stiffness parameter κ^{α} can be tuned to counterbalance the strength of the bias. We denoted in Eq. (3.46) for simplicity

$$\exp\{-\beta \mathrm{H}(\mathbf{z})\} = \exp(-\beta \mathcal{H}(\mathbf{x}_0)) \prod_{i=0}^{\tau/\delta t - 1} \delta\left[\mathbf{x}_{(i+1)\delta t} - \phi_{\delta t}(\mathbf{x}_{i\delta t})\right] \tag{3.49}$$

as the unnormalized dynamical path probability arising from the deterministic propagation of the trajectory.

In this biased ensemble, choosing positive α enhances the probability weights of trajectories with a large Lyapunov indicator $L(\mathbf{z})$, favoring via Eq. (3.28), to reactive paths passing over saddles and unstable directions of the potential energy landscape. On the contrary, choosing negative α would mainly restrict the sampling of non reactive or regular trajectories within stable basins.

Shooting algorithm

The standard shooting algorithm for deterministic dynamic is obtained by (i) selecting a state $\mathbf{x}_{t'}$ of the current trajectory, (ii) perturbing the momenta of each particle of this state, and then generating from this selected state two segments, one backward of duration t' and the other one forward of duration $\tau - t'$, in order to get a trial trajectory $\tilde{\mathbf{z}}$ of same duration, (iii) accepting or rejecting the new trajectory $\tilde{\mathbf{z}}$. For deterministic dynamics, the total energy is constant.

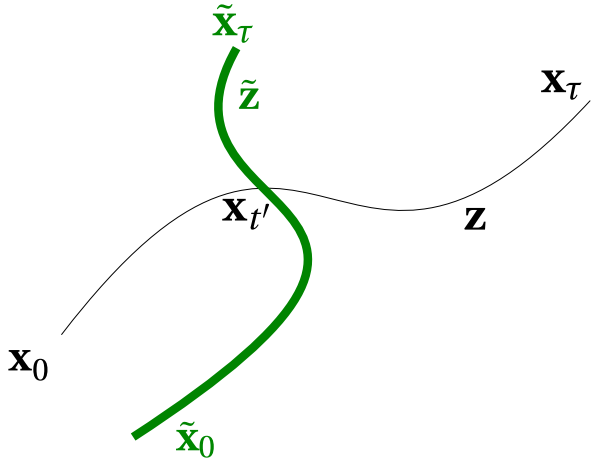

Figure 3.1: Representation of the shooting move: the trial trajectory $\tilde{\mathbf{z}}$ (in green) is derived from the current trajectory $\mathbf{z}$ by perturbing momenta at state $\mathbf{x}_{t'}$.

The perturbation step (ii) is done with the algorithm proposed by Stoltz [74], where momenta for the trial trajectory $\tilde{\mathbf{z}}$ are obtained from old ones as

$$\tilde{\mathbf{p}} = \varepsilon \mathbf{p} + \sqrt{1-\varepsilon^2}\delta\mathbf{p} \tag{3.50}$$

where ε is a tunable parameter and $\delta\mathbf{p}$ is drawn from a white Gaussian distribution of variance mk_BT. Since we have $\langle \delta\mathbf{p}^2 \rangle = \left\langle |\mathbf{p}|^2 \right\rangle = mk_BT$ and $\langle \delta\mathbf{p} \cdot \mathbf{p} \rangle = 0$, the variance of $\tilde{\mathbf{p}}$ is

$$\left\langle |\tilde{\mathbf{p}}|^2 \right\rangle = \left\langle \varepsilon^2 |\mathbf{p}|^2 + (1-\varepsilon^2) |\delta\mathbf{p}|^2 \right\rangle = mk_BT \tag{3.51}$$

thus the distribution of the kinetic energy is preserved. Furthermore, the probability of having trial momenta $\tilde{\mathbf{p}}$ from $\mathbf{p}$ is written as [74]

$$p(\mathbf{p} \to \tilde{\mathbf{p}}) = \left(\frac{1}{\sqrt{2\pi(1-\varepsilon^2)}} \right)^{3N} \exp\left\{ -\frac{(\tilde{\mathbf{p}} - \varepsilon\mathbf{p})^T (\tilde{\mathbf{p}} - \varepsilon\mathbf{p})}{2(1-\varepsilon^2) mk_BT} \right\}. \tag{3.52}$$

and ensures a detailed balance condition at the shooting point t'

$$\frac{\exp\{-\beta\mathcal{H}(\tilde{\mathbf{x}}_{t'})\}\, p(\tilde{\mathbf{p}}_{t'} \to \mathbf{p}_{t'})}{\exp\{-\beta\mathcal{H}(\mathbf{x}_{t'})\}\, p(\mathbf{p}_{t'} \to \tilde{\mathbf{p}}_{t'})} = 1. \tag{3.53}$$

such that the probability flux between the current and perturbed momenta at the shooting point is balanced, and the hamiltonian distribution is preserved.

If we neglect numerical approximations in the integration from $\tilde{\mathbf{x}}'_t$ to $\tilde{\mathbf{x}}_0$, that indeed give in computations $\mathcal{H}(\tilde{\mathbf{x}}'_t) \neq \mathcal{H}(\tilde{\mathbf{x}}_0)$, due to finite time step discretizations, we finally obtain

$$\frac{\exp\left\{-\beta\mathcal{H}(\tilde{\mathbf{x}}_0)\right\} p\left(\tilde{\mathbf{p}}_{t'} \to \mathbf{p}_{t'}\right)}{\exp\left\{-\beta\mathcal{H}(\mathbf{x}_0)\right\} p\left(\mathbf{p}_{t'} \to \tilde{\mathbf{p}}_{t'}\right)} = 1. \tag{3.54}$$

Using Eq. (3.52) the probability $p_{gen}[\mathbf{x}_{t'} \to \tilde{\mathbf{x}}_{t'}]$ of obtaining the shooting point $\tilde{\mathbf{x}}_{t'}$ for the trial trajectory from state $\mathbf{x}_{t'}$ selected in the current trajectory reads

$$p_{gen}[\mathbf{x}_{t'} \to \tilde{\mathbf{x}}_{t'}] = p\left(\mathbf{p}_{t'} \to \tilde{\mathbf{p}}_{t'}\right) \tag{3.55}$$

as only momenta are perturbed at the shooting point, while positions are left unchanged.

The generating probability $P_{gen}[\mathbf{z} \to \tilde{\mathbf{z}}]$ appearing in Eq. (3.44) can now be determined as follows. The probability to generate the segment of $\tilde{\mathbf{z}}$ from time t' to time τ forward is

$$P^f_{gen}[\tilde{\mathbf{z}}] = \prod_{i=t'/\delta t}^{\tau/\delta t-1} \delta\left[\tilde{\mathbf{x}}_{(i+1)\delta t} - \phi_{\delta t}(\tilde{\mathbf{x}}_{i\delta t})\right]. \tag{3.56}$$

while the probability to generate the segment of $\tilde{\mathbf{z}}$ from time t' to time 0 backward is

$$P^b_{gen}[\tilde{\mathbf{z}}] = \prod_{i=1}^{t'/\delta t} \delta\left[\tilde{\mathbf{x}}_{(i-1)\delta t} - \phi^{-1}_{\delta t}(\tilde{\mathbf{x}}_{i\delta t})\right] \tag{3.57}$$

where $\phi^{-1}_{\delta t}$ is the time reversal of the temporal propagator $\phi_{\delta t}$ associated with the deterministic dynamics, i.e. $\phi^{-1}_{\delta t} = \phi_{-\delta t}$.

Combining the generating probability for the forward and backward segments of the trial trajectory $\tilde{\mathbf{z}}$ with $p_{gen}[\mathbf{x}_{t'} \to \tilde{\mathbf{x}}_{t'}]$, we obtain the overall generating probability for the trial trajectory

$$P_{gen}[\mathbf{z} \to \tilde{\mathbf{z}}] = p_{gen}[\mathbf{x}_{t'} \to \tilde{\mathbf{x}}_{t'}] \prod_{i=1}^{t'/\delta t} \delta\left[\tilde{\mathbf{x}}_{(i-1)\delta t} - \phi^{-1}_{\delta t}(\tilde{\mathbf{x}}_{i\delta t})\right] \prod_{i=t'/\delta t}^{\tau/\delta t-1} \delta\left[\tilde{\mathbf{x}}_{(i+1)\delta t} - \phi_{\delta t}(\tilde{\mathbf{x}}_{i\delta t})\right] \tag{3.58}$$

Inserting Eq. (3.46) and Eq. (3.58) in Eq. (3.44) we have

$$P_{acc}\left[\mathbf{z} \to \tilde{\mathbf{z}}\right] = \min\left\{1, \frac{\exp\left\{\alpha L(\tilde{\mathbf{z}}) - \beta\mathcal{H}(\tilde{\mathbf{x}}_0)\right\} \varphi^\alpha_A(\tilde{\mathbf{x}}_0) p_{gen}[\tilde{\mathbf{x}}_{t'} \to \mathbf{x}_{t'}]}{\exp\left\{\alpha L(\mathbf{z}) - \beta\mathcal{H}(\mathbf{x}_0)\right\} \varphi^\alpha_A(\mathbf{x}_0) p_{gen}[\mathbf{x}_{t'} \to \tilde{\mathbf{x}}_{t'}]}\right\} \tag{3.59}$$

Note that in Eq. (3.59) terms deriving from the forward and backward generation of the current and trial path cancel:

$$\frac{\prod_{i=0}^{\tau/\delta t-1} \delta\left[\tilde{\mathbf{x}}_{(i+1)\delta t} - \phi_{\delta t}(\tilde{\mathbf{x}}_{i\delta t})\right] P^f_{gen}[\mathbf{z}] P^b_{gen}[\mathbf{z}]}{\prod_{i=0}^{\tau/\delta t-1} \delta\left[\mathbf{x}_{(i+1)\delta t} - \phi_{\delta t}(\mathbf{x}_{i\delta t})\right] P^f_{gen}[\tilde{\mathbf{z}}] P^b_{gen}[\tilde{\mathbf{z}}]} = 1. \tag{3.60}$$

This is a consequence of the unit phase space compressibility of the Newtonian dynamics [4], that ensures the microscopic reversibility between forward and backward moves: indeed, the deterministic move for each time step in Eq. (3.56) can be written as

$$\delta\left[\mathbf{x}_{(i+1)\delta t} - \phi_{\delta t}(\mathbf{x}_{i\delta t})\right] = \delta\left[\phi_{\delta t}^{-1}(\mathbf{x}_{(i+1)\delta t}) - \mathbf{x}_{i\delta t}\right] \left|\partial\phi_{\delta t}(\mathbf{x}_{i\delta t})/\partial\mathbf{x}_{i\delta t}\right|^{-1} \tag{3.61}$$

where $|\partial\phi_{\delta t}(\mathbf{x}_{i\delta t})/\partial\mathbf{x}_{i\delta t}|$ is the Jacobian associated with the time evolution of duration δt. For Newtonian dynamics, the Liouville theorem guarantees that the phase space volume is conserved (see Appendix A), hence this Jacobian is unity. Eq. (3.60) is then directly obtained by using Eq. (3.61) in Eq. (3.56) to express the forward generation P_{gen}^{f}: forward and backward moves in Eq. (3.60) simplify, and the only remaining terms are due to Jacobians, that are equal to one.

Using in Eq. (3.59) the property of the Stoltz proposal (Eq. (3.54)), the Metropolis acceptance rule in Eq. (3.44) can be furthermore simplified as

$$P_{acc}\left[\mathbf{z} \to \tilde{\mathbf{z}}\right] = \min\left\{1, \exp\left\{\alpha L(\tilde{\mathbf{z}}) - \alpha L(\mathbf{z})\right\}\left[\varphi_A^{\alpha}(\tilde{\mathbf{x}}_0)/\varphi_A^{\alpha}(\mathbf{x}_0)\right]\right\}. \tag{3.62}$$

Shifting algorithm

The second Monte Carlo move in trajectory space is based on the shifting algorithm, supplemented with a waste-recycling estimator. [87] $\mathcal{N}$ trial trajectories $\tilde{\mathbf{z}}_j$ are constructed from $\mathbf{z}$ as follows: the duration of the trajectory $\mathbf{z}$ is doubled selecting a random duration $\nu\delta t$ and integrating two segments backward and forward, starting from $\mathbf{x}_0$ and $\mathbf{x}_\tau$, along ν and $\mathcal{N} - \nu$ time steps, respectively. Adding these segments to the current trajectory, one obtains a "buffer" trajectory $\zeta = \{\mathbf{x}_{n\delta t}\}_{-\nu \le n \le 2\mathcal{N}-\nu}$ of total duration $2\mathcal{N}\delta t$, containing $\mathcal{N}$ possible trial paths. The conditional probability of obtaining the "buffer" trajectory ζ starting from the current trajectory $\mathbf{z}$ is indicated as $P_{cond}(\zeta|\mathbf{z})$.

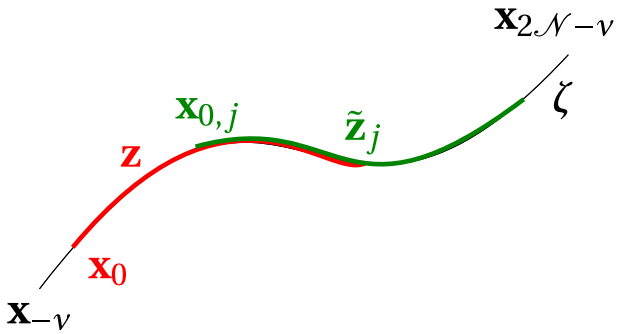

Figure 3.2: Representation of the shifting move: the buffer path ζ is derived from the current trajectory $\mathbf{z}$ (in red). One of the $\mathcal{N}$ trial trajectories $\tilde{\mathbf{z}}_j$ is selected (in green).

The probability weight of each trial path $\tilde{\mathbf{z}}_j$ is then

$$\mathcal{P}_A^\alpha(\tilde{\mathbf{z}}_j) = \frac{1}{Z_A^\alpha} \exp\left\{\alpha L(\tilde{\mathbf{z}}_j) - \beta H(\tilde{\mathbf{z}}_j)\right\} \varphi_A^\alpha(\tilde{\mathbf{x}}_{0,j}) \tag{3.63}$$

if a constraining function $\varphi_A^\alpha(\tilde{\mathbf{x}}_{0,j})$ linking the initial state $\tilde{\mathbf{x}}_{0,j}$ of each trial path $\tilde{\mathbf{z}}_j$ trajectories to state A is used, as in Eq. (3.46). Index j runs over the $\mathcal{N}$ possible paths on the "buffer" trajectory.

For the sake of concision, we introduce an action

$$-s_{\alpha,j} = \alpha L(\tilde{\mathbf{z}}_j) - \beta H(\tilde{\mathbf{z}}_j) \tag{3.64}$$

so as to rewrite the trajectory probability in the biased ensemble (Eq. (3.46)) as

$$\mathcal{P}_A^\alpha(\tilde{\mathbf{z}}_j) = \frac{1}{Z_A^\alpha} \varphi_A^\alpha(\tilde{\mathbf{x}}_{0,j}) \exp\left\{-s_{\alpha,j}\right\}. \tag{3.65}$$

We now define the selecting probability $P_{sel}(\tilde{\mathbf{z}}_j|\zeta)$ of selecting a trial trajectory $\tilde{\mathbf{z}}_j$ from the buffer trajectory ζ as

$$P_{sel}(\tilde{\mathbf{z}}_j|\zeta) = \frac{\varphi_A^\alpha(\tilde{\mathbf{x}}_{0,j}) \exp\left\{-s_{\alpha,j}\right\}}{\mathcal{R}_\alpha} \tag{3.66}$$

where we introduced the Rosenbluth factor

$$\mathcal{R}_\alpha = \sum_{j=1}^{\mathcal{N}} \varphi_A^\alpha(\tilde{\mathbf{x}}_{0,j}) \exp\left[-s_{\alpha,j}\right]. \tag{3.67}$$

Resorting to Bayes theorem, P_{sel} can be written as the posterior likelihood probability [36] of having $\tilde{\mathbf{z}}_j$ given the "buffer" trajectory ζ:

$$P_{sel}(\tilde{\mathbf{z}}_j|\zeta) = \frac{P_{cond}(\zeta|\tilde{\mathbf{z}}_j)\mathcal{P}_A^\alpha(\tilde{\mathbf{z}}_j)}{P_{marg}(\zeta)} \tag{3.68}$$

where $P_{cond}(\zeta|\tilde{\mathbf{z}}_j)$ is the conditional probability of constructing a "buffer" path ζ from the trial path, as in Eq. (3.39), and because of the deterministic dynamics, $P_{cond}(\zeta|\tilde{\mathbf{z}}_j) = 1/\mathcal{N}$. $P_{marg}(\zeta)$ is the marginal probability associated with the buffer path: comparing Eq. (3.68) with Eq. (3.66), we see that

$$P_{marg}(\zeta) = \mathcal{R}_\alpha \frac{1}{Z_A^\alpha} \frac{1}{\mathcal{N}}. \tag{3.69}$$

Let us now consider a Monte Carlo move between two paths both contained in the buffer trajectory ζ , i.e. from the current path $\mathbf{z}$ to $\tilde{\mathbf{z}}_j$, whose associated transition probability $\pi[\mathbf{z} \to \tilde{\mathbf{z}}_j]$, as in Eq. (3.42), obeys a detailed balance with respect to the prior distribution $\mathcal{P}_A^\alpha$:

$$\mathcal{P}_A^\alpha[\mathbf{z}]\, \pi[\mathbf{z} \to \tilde{\mathbf{z}}_j] = \mathcal{P}_A^\alpha[\tilde{\mathbf{z}}_j]\, \pi[\tilde{\mathbf{z}}_j \to \mathbf{z}]. \tag{3.70}$$

Defining the transition probability

$$\pi\left[\mathbf{z} \to \tilde{\mathbf{z}}_j\right] = P_{sel}(\tilde{\mathbf{z}}_j|\zeta)P_{cond}(\zeta|\mathbf{z}) \tag{3.71}$$

the detailed balance in Eq. (3.70) can be recasted as

$$P_{sel}(\tilde{\mathbf{z}}_j|\zeta)P_{cond}(\zeta|\mathbf{z})\mathcal{P}_A^\alpha(\mathbf{z}) = P_{sel}(\tilde{\mathbf{z}}_\nu|\zeta)P_{cond}(\zeta|\tilde{\mathbf{z}}_j)\mathcal{P}_A^\alpha(\tilde{\mathbf{z}}_j) \tag{3.72}$$

where $\mathbf{z} = \tilde{\mathbf{z}}_\nu$ and $P_{sel}(\tilde{\mathbf{z}}_\nu|\zeta)$ is the probability to transit from $\tilde{\mathbf{z}}_j$ to $\mathbf{z}$. P_{sel} leaves then the probability distribution $\mathcal{P}_A^\alpha$ invariant. Moreover, recalling that the deterministic dynamics entails $P_{cond}(\zeta|\mathbf{z}) = P_{cond}(\zeta|\tilde{\mathbf{z}}_j)$, the detailed balance in Eq. (3.72) simplifies into

$$P_{sel}(\tilde{\mathbf{z}}_j|\zeta)\mathcal{P}_A^\alpha(\mathbf{z}) = P_{sel}(\tilde{\mathbf{z}}_\nu|\zeta)\mathcal{P}_A^\alpha(\tilde{\mathbf{z}}_j). \tag{3.73}$$

We conclude this section by extending the detailed balance of Eq. (3.70) for trajectories $\mathbf{z}$ and $\tilde{\mathbf{z}}_j$ belonging to two *different* buffer paths ζ and $\tilde{\zeta}$ respectively. Writing as in Eq. (3.68) expressions for $P_{sel}(\mathbf{z}|\zeta)$ and $P_{sel}(\tilde{\mathbf{z}}_j|\tilde{\zeta})$, and using these results in Eq. (3.70) we obtain

$$P_{marg}(\zeta)P_{sel}(\mathbf{z}|\zeta)\pi\left[\mathbf{z} \to \tilde{\mathbf{z}}_j\right] = P_{marg}(\tilde{\zeta})P_{sel}(\tilde{\mathbf{z}}_j|\tilde{\zeta})\pi\left[\tilde{\mathbf{z}}_j \to \mathbf{z}\right] \tag{3.74}$$

Eq. (3.74) is indeed a detailed balance condition for the alternate shooting and shifting moves, and samples the buffer trajectory ζ. This implies that the distribution P_{marg} is invariant along the sampling algorithm. P_{marg} is therefore suitable to be used as an input path probability weight required by the unbiasing algorithm MBAR, presented in Section 3.4.3.

3.4 Reaction-rate constants calculation

3.4.1 Rate constants theory

Here we recall how to calculate reaction rates in the TPS framework. A more detailed description is given in Appendix F. The reactivity of the sampled paths is given by the time correlation function with respect to initial and final states of the paths: a trajectory is said to be reactive if it starts in the reactants A basin and ends in the products B basin. The time correlation function [54, 2] is

$$C(t) = \frac{\langle h_A(\mathbf{x}_0)h_B(\mathbf{x}_t)\rangle}{\langle h_A(\mathbf{x}_0)\rangle} \tag{3.75}$$

where again the indicator function h_Ω is defined for a generic state Ω as

$$h_\Omega(\mathbf{x}) = \begin{cases} 1 & \mathbf{x} \in \Omega \\ 0 & \mathbf{x} \notin \Omega \end{cases}$$

and brackets $\langle\cdot\rangle$ indicate averages taken over the equilibrium trajectory ensemble. $C(t)$ can therefore be understood as the (conditional) probability of observing a trajectory of duration t ending in state B, knowing that it started in state A: indeed, using a reactive flux formalism and detailed balance conditions, [75, 54, 2] this probability $p(\mathbf{x}_t \in B \mid \mathbf{x}_0 \in A)$ equals $C(t)$. The correlation function approach its asymptotic value exponentially as

$$C(t) \approx \rho_B^{eq} \left(1 - \exp\left\{-t/\tau_{rxn}\right\}\right) \tag{3.76}$$

where ρ_B^{eq} is the equilibrium occupation probability of state B, and the parameter $\tau_{rxn} \equiv (k_{A\to B} + k_{B\to A})^{-1}$ is the characteristic reaction time of the system, given by the forward and backward reaction constants $k_{A\to B}$ and $k_{B\to A}$, respectively.

Note that the basic assumption required to compute reaction rate constants of rare events from the correlation function $C(t)$ is the presence of a well separated time scale for processes occurring between 'fast' intra-funnel relaxation, having a typical time constant τ_{mol}, and activated processes indicating passages *between* funnels, needing a much longer time scale, of the order of τ_{rxn} [75].

For times in the intermediate time regime $\tau_{mol} < t \ll \tau_{rxn}$, the correlation function in Eq. (3.76) can indeed be expressed by means of its first order expansion

$$C(t) \approx k_{A\to B} t \tag{3.77}$$

where the detailed balance condition $k_{A\to B}\rho_A^{eq} = k_{B\to A}\rho_B^{eq}$ has been used to eliminate ρ_B^{eq}. Hence, the slope of $C(t)$ for this intermediate time regime gives direct access to reaction rates. The reactive probability flux flowing from state A towards B per unit time, defined by $k(t) \equiv \frac{dC(t)}{dt}$, displays a plateau corresponding to the forward phenomenological reaction constant $k_{A\to B}$. [70]

Let us point out that these results, obtained with a macroscopic 'flux over population' probability approach, can be recovered by a Bennett-Chandler formalism [70], based on microscopic quantities (positions and momenta, see Appendix F). Moreover, this second framework gives important information on the relation between the phenomenological forward rate constant $k_{A\to B}$ and its Transition State Theory value k_{TST}, defined as [17]

$$k_{TST} = \left(\frac{k_B T}{h}\right) \exp\left(-\beta \Delta F_{A\to B}\right) \tag{3.78}$$

where $\Delta F_{A\to B}$ is the height of the free energy barrier separating states A and B, h is the Planck constant and $\beta = \frac{1}{k_B T}$ the inverse temperature. The reactive flux can indeed be expressed as [70]

$$k(t) = \kappa(t) k_{TST} \tag{3.79}$$

where $\kappa(t)$ is the *transmission factor*. This factor is always lower than one, and is introduced to take into account trajectories started in basin A that reach the saddle point but

fall back to state A, instead of ending in state B: these occurrences are called *recrossing events*. The transmission coefficient usually reaches a steady value, depending on the temperature and the reaction coordinate chosen to localize the barrier. At this plateau value of $\kappa = \bar{\kappa} < 1$, the reactive flux corresponds to

$$k_{A\to B} = \bar{\kappa} k_{TST}. \tag{3.80}$$

thus showing that phenomenological rates are always lower than TST rates.

3.4.2 Rate constants with biased sampling and *waste-recycling*

In numerical experiments, the computation of reaction constants by direct evaluation of $C(t)$ at times longer than the intrafunnel relaxation time τ_{mol} means performing very long molecular dynamics trajectories. To estimate $C(t)$ in the TPS framework computing relatively short trajectories, one resorts to a factorisation of the correlation function in a static quantity related to k_{TST}, thus dependent on the free-energy barrier and calculated through an umbrella-sampling technique, and a dynamic factor related to $\kappa(t)$ given by the time derivative of the probability of reaching basin B at times shorter than the whole trajectory length. [63, 3]

We propose herein a variant strategy: reaction constants will be calculated directly by averaging indicator functions on short trajectories, as in Eq. (3.75), once the fraction of reactive paths is significantly enhanced by introducing an appropriate bias favoring reactions between basins A and B.

The correlation function in Eq. (3.75) can be intended as an average over all performed trajectories - i.e. over all successive steps m of the Markov chain - of the *reactivity* $\mathcal{A}(\mathbf{z}^m)$, defined as

$$\mathcal{A}(\mathbf{z}^m) = h_A(\mathbf{x}_0^m) h_B(\mathbf{x}_\tau^m) \tag{3.81}$$

For an unbiased TPS algorithm sampling the probability of Eq. (3.46), $C(t) = \langle \mathcal{A} \rangle_0$, where brackets $\langle \cdot \rangle_0$ correspond to averages over a canonical trajectory ensemble and the trajectory distribution ensures $\langle h_A(\mathbf{x}_0) \rangle = 1$ because of φ_A^α.

In a context of biased TPS, averages on Markov chains are taken on the biased trajectory distribution, hence we denote biased averages of the correlation function as $C_\alpha(t) = \langle \mathcal{A} \rangle_\alpha$, where index α accounts for the current bias. Herein, index α will indicate all observables obtained from a biased distribution, where $\alpha = 0$ stands for the equilibrium canonical ensemble average. We estimate the correlation function $C_\alpha(t) = \langle \mathcal{A} \rangle_\alpha$ using an estimator denoted by $\mathbb{I}_\alpha^M$, which consists in taking the average over the Markov chain of lenght M as

$$\mathbb{I}_\alpha^M [\mathcal{A}] = \frac{1}{M} \sum_{m=1}^{M} \mathcal{A}_\alpha^m \tag{3.82}$$

$\mathcal{A}(\mathbf{z}_\alpha^m) = \mathcal{A}_\alpha^m$ denotes a reactivity value coming from a biased trajectory $\mathbf{z}_\alpha$ distributed according to $\mathcal{P}_A^\alpha$. Estimates given by $\mathbb{I}_\alpha^M$ are however not optimal [94].

A *waste-recycling* (WR) estimator [94, 95] is associated to the multiple proposal sampler for the shifting move of Sec. 3.3.2 to obtain more accurate estimates. Waste recycling consists in including information about all possible paths contained in the buffer trajectory ζ. The reactivity at Markov chain step m in a given ensemble α has to be first averaged over the $\mathcal{N}$ trajectories contained in the buffer path ζ_α^m as

$$\overline{\mathcal{A}}_\alpha^m = \sum_{j=1}^{\mathcal{N}} \mathcal{A}_{\alpha,j}^m \frac{\varphi_A^\alpha(\mathbf{x}_j^m)\exp\left[-s_{\alpha,j}^m\right]}{\mathcal{R}_\alpha^m} = \sum_{j=1}^{\mathcal{N}} \mathcal{A}_{\alpha,j}^m \varphi_A^\alpha(\mathbf{x}_j^m)\exp\left[-s_{\alpha,j}^m + S_\alpha^m\right] \tag{3.83}$$

where we write $\overline{\mathcal{A}}_\alpha^m = \overline{\mathcal{A}}(\zeta_\alpha^m)$ and define the Rosenbluth factor

$$\mathcal{R}_\alpha^m \equiv \exp\left[-S_\alpha^m\right] \tag{3.84}$$

as proportional to the marginal probability $P_{marg}(\zeta_\alpha^m)$ of Eq. (3.67) associated to the "buffer" trajectory ζ_α^m corresponding to Markov chain step m. Correlation functions for reactive paths are therefore estimated in a way similar to Eq. (3.82), with the WR estimator

$$\mathbb{J}_\alpha^M[\mathcal{A}] = \frac{\sum_{m=1}^M \sum_{j=1}^{\mathcal{N}} \mathcal{A}_{\alpha,j}^m \varphi_A^\alpha(\mathbf{x}_j^m)\exp\left[-s_{\alpha,j}^m + S_\alpha^m\right]}{\sum_{m=1}^M \sum_{j=1}^{\mathcal{N}} \varphi_A^\alpha(\mathbf{x}_j^m)\exp\left[-s_{\alpha,j}^m + S_\alpha^m\right]} = \frac{1}{M}\sum_{n=1}^M \overline{\mathcal{A}}_\alpha^m \tag{3.85}$$

and again $C_\alpha(t) \approx \mathbb{J}_\alpha[\mathcal{A}]$. The calculation of rate constants $k_{A\to B}^\alpha$ for the given α-ensemble follows from Eq. (3.77). We discuss in Section 3.5.3 the effect of WR in the evaluation of reaction constants.

3.4.3 Unbiasing rate constants: the MBAR algorithm

A suitable unbiasing algorithm is needed in order to recover canonical ensemble correlation functions from reactivity values witnessed in a Lyapunov biased path ensemble. The canonical equilibrium values of $C_0(t)$ can in principle be obtained by estimating reactivities $\mathcal{A}_\alpha^m$, computed in any α-biased path ensemble, resorting to an adequate unbiasing algorithm. We define an unbiasing WR estimator $\mathbb{J}_{\theta,\alpha}$, where the left subscript θ indicates the ensembles in which we are interested in measuring averages, while the right subscript α refers to the ensemble that our Lyapunov biased TPS will effectively sample. Equilibrium values for $C_0(t)$ ($\theta = 0$) are retrieved from reactivities computed in any α-biased ensemble as

$$C_0(t) \approx \mathbb{J}_{0,\alpha}^M[\mathcal{A}] = \frac{\sum_{n=1}^M \sum_{j=1}^{\mathcal{N}} \mathcal{A}_\alpha^m \varphi_A^\alpha(\mathbf{x}_{0,j}^m)\varphi_A^{\alpha\,-1}(\mathbf{x}_{0,j}^m)\exp\left[-s_{\alpha,j}^m + S_\alpha^m + s_{\alpha,j}^m\right]}{\sum_{n=1}^M \sum_{j=1}^{\mathcal{N}} \varphi_A^\alpha(\mathbf{x}_{0,j}^m)\varphi_A^{\alpha\,-1}(\mathbf{x}_{0,j}^m)\exp\left[-s_{\alpha,j}^m + S_\alpha^m + s_{\alpha,j}^m\right]} \tag{3.86}$$

Unbiasing the sampling consists of correcting for the bias $\varphi_A^\alpha(\mathbf{x}_j^m)\exp\left[-s_{\alpha,j}^m\right]$. However, the variance associated to the unbiasing estimator in Eq. (3.86) would be too large to consider estimates reliable [66]. This well-known fact results from the lack of overlap between the sampled and measured distributions. We therefore carry out a series of simulations for a set of α values ranging from 0 to a maximum value α_{max} so to ensure overlap between successive sampled distributions.

Our choice is then to use the multistate Bennett acceptance ratio (MBAR) instead of the estimator of Eq. (3.86). MBAR is a method elaborated by Shirt and Chodera [66, 76], which aims at minimizing the statistical variance associated to the estimates. Following these authors, we briefly expose the principles of this procedure in a context of biased path ensembles in Appendix E.

To use the MBAR method in the waste-recycling framework of Sec. 3.4.2, we take as probability weights corresponding to a given α ensemble at each Markov chain step m the marginal probability $P_{marg}^\alpha(\zeta_\alpha^m)$ of Eq. (3.84). This is possible because, thanks to the detailed balance of Eq. (3.74), P_{marg}^α is preserved.

Once one knows weights $\exp[-S_\alpha]$ related (via Eqs. (E.3)-(E.5)) to $P_{marg}^\alpha(\zeta_\alpha)$ for each α-ensemble, reactivity averages $\langle\mathcal{A}\rangle_{\alpha'}$ for every ensemble $\alpha'\neq\alpha$ can be computed resorting to the importance sampling identity

$$\frac{\langle\mathcal{A}\exp[-S_{\alpha'}]\rangle_\alpha}{\langle\mathcal{A}\exp[-S_\alpha]\rangle_{\alpha'}}=\frac{Z_{\alpha'}}{Z_\alpha} \tag{3.87}$$

where we used the partition functions $Z_\alpha=\int\mathcal{D}\zeta\exp[-S_\alpha(\zeta)]$. For a set of K different values of the bias α, a set (namely, a Markov chain) of $\mathcal{M}_\alpha$ buffer trajectories are sampled for each bias value. An estimate of $C_\alpha(t)$ is given by the MBAR estimator $\mathbb{K}$ for the waste-recycling averaged reactivity $\overline{\mathcal{A}}_\alpha$ of Eq. (3.83) as

$$\mathbb{K}_\alpha^{\mathcal{M}_\alpha}[\mathcal{A}]=\sum_{m=1}^{\mathcal{M}_\alpha}W_{m,\alpha}\overline{\mathcal{A}}_\alpha^m \tag{3.88}$$

where weights $W_{m,\alpha}$ are given by the expression

$$W_{m,\alpha}=\hat{Z}_\alpha^{-1}\frac{\exp[-S_\alpha^m]}{\sum_{k=1}^K\mathcal{M}_k\hat{Z}_k^{-1}\exp\left[-S_{\alpha_k}^m\right]}. \tag{3.89}$$

and $\hat{Z}_\alpha$ are estimators for the partition functions Z_α with minimal asymptotic covariance (see Eq. (E.5) and Ref. [76]). Note that the denominator in Eq. (3.89) indicates that each weight $W_{m,\alpha}$ takes into account contributions from all other ensembles $k=0,...,\alpha,...,K$.

Introducing also partition functions $Z_{\mathcal{A}_\alpha}\equiv\int\mathcal{D}\zeta\mathcal{A}\exp[-S_\alpha(\zeta)]$, the uncertainty can be estimated as

$$\mathrm{var}(\mathbb{K}_\alpha[\mathcal{A}])\approx\mathbb{K}_\alpha[\mathcal{A}]^2\left(\mathrm{var}(\hat{\mathrm{Z}}_{\mathcal{A}_\alpha})+\mathrm{var}(\hat{\mathrm{Z}}_\alpha)-2\mathrm{cov}(\hat{\mathrm{Z}}_{\mathcal{A}_\alpha},\hat{\mathrm{Z}}_\alpha)\right). \tag{3.90}$$

Canonical equilibrium values of the correlation function $C_0(t)$ and corresponding values of the reaction rate constants can be recovered once we consider estimates in Eq. (3.90) with $\alpha = 0$. We emphasize that this is by now the first application of the MBAR unbiasing method based on marginal probabilities, able to estimate observables computed with a path sampling algorithm supplemented by waste-recycling. Numerical recipes to obtain these estimations have been furnished by J. Chodera [91].

3.5 Numerical results: LJ_{38}

3.5.1 LJ_{38} cluster

In order to test the Lyapunov biased TPS algorithm (LyTPS), we consider again a Lennard-Jones 38 cluster. We recall briefly his main properties.

LJ_{38} is a well-known benchmark system aimed at assessing the efficiency of sampling algorithms, and has been widely explored in literature for its rich thermodynamic properties. The LJ_{38} potential energy landscape presents two main basins: a deep and narrow funnel containing the global energy minimum, a face-centered cubic truncated octahedron structure (FCC), and a separate, wider, funnel leading to a large number of icosahedral structures (ICO) of slightly higher energies. Although the configuration with the lowest potential energy corresponds to the FCC one, the greater configurational entropy associated with a large number of local minima in the icosahedral funnel make this second configuration much more stable at higher temperatures. As temperature increases, LJ_{38} undergoes several structural transitions. First, a solid-solid transition occurs at $T_{ss} = 0.12\frac{\varepsilon}{k_B}$ when the octahedral FCC structure gives place to the icosahedral ones. Secondly, above $T_{sl} = 0.18\frac{\varepsilon}{k_B}$, the outer layer of the cluster melts, while the core remains of icosahedral structure. [32]

The Lennard-Jones potential and the bond-orientational order parameter Q_4 are the same as described in Sec. 2.4.2 of Chapter 2.

We recall (see Chapter 2) that Monte Carlo sampling fails to equilibrate the two funnels, and global optimization methods are unable to find its global energy minimum [2]. Hence, several elaborated algorithm have been employed in the past to study the thermodynamic equilibrium of this system, such as parallel tempering, [30, 31, 32] basin-sampling techniques, [33] Wang-Landau approaches [34] or path-sampling methods. [23, 35, 36]

Standard transition path sampling [35] and discrete path sampling [37] (DPS) have been already used to study transitions between the two funnels of LJ_{38}. However, in the case of TPS the large number of metastable states separating the two main basins prevented the traditional shooting and shifting algorithm to identify reactive paths, despite previous success for smaller LJ clusters. [42] Authors had to resort to a two-ended approach linking the two minima to find trajectories with the same energy of those found by DPS

approach. [35] The main drawbacks of this TPS method were a lack of ergodicity and a very large computational cost.

Conversely, DPS has been more successfull in this task. This method uses eigenvector following and graph transformation [41] to compute the overall transition rate between two regions of phase space. To the best of our knowledge, this is by now the most successful approach to computing reaction rates in LJ_{38}. [41] In particular, reaction rate constants for transitions between the two solid structures have been computed using DPS [37, 38, 39] at different temperatures.

We use here the Lyapunov biased TPS algorithm to investigate structural transitions in LJ_{38} for temperatures above and below the solid-solid transition temperature $T_{ss} = 0.12$, spanning a temperature range from $T = 0.10$ to $T = 0.15$. Our simulations required about 10^2 hours of cpu time to observe reactive trajectories between the two main funnels. Reaction constants, computed with the method exposed in Sec. F, can be compared to values obtained with the discrete path sampling approach. [35]

3.5.2 FCC-ICO reactive paths

In order to thermalize the system at a given temperature, Langevin dynamics are run for 1000 time steps, using a friction parameter $\gamma\delta t = 1$. The last configuration is used as the starting point of the first deterministic trajectory of the TPS simulations. At each new temperature, a new preliminary Langevin dynamics is performed.

In the simulations, trajectories consist of $\mathcal{N} = 700$ time steps, each step of duration $\delta t = 10^{-2}$. Deterministic trajectories are obtained with the Verlet algorithm [74], and then selected following the Lyapunov biased TPS algorithm described in Sec. 3.3. For each temperature, 25 different biased path distributions are sampled, for values of the control parameter α ranging from $\alpha = 1$ to $\alpha = 2500$, in order to obtain reactive paths and have a sufficient overlap between distributions sampled for different α values. The unbiased distribution corresponding to $\alpha = 0$ has been simulated with TPS as well.

Values for the control parameters are chosen after observing the magnitude of the Lyapunov indicators $L(\mathbf{z})$ for few trajectories, and the difference between Lyapunov indicators $L(\mathbf{z})$ for current and trial trajectories in the shooting step (Eq. (3.62)), in order to have an acceptance ratio for the shooting move not below 20%, see Fig. 3.3. The choice of the trajectory length τ depends not on the Lyapunov bias, but on the necessity of having long enough trajectories to link the two funnels, and recover an appropriate statistics for the calculations of reaction contants (see below). The use of the Stoltz algorithm (Eq. (3.50)) in the shooting moves ensures that the energy distribution imposed by the preliminary MD is maintained along the simulation. The value for ε in Eq. (3.50) is taken as 0.95, so to control the decorrelation of sampled paths and ensure a sufficient acceptance ratio, see Fig. 3.4. A Markov sequence of 5000 biased TPS shooting and shifting moves is performed,

in order to ensure an ergodic sampling. For the diagonalization of the hessian matrix via the Lanczos algorithm (see Appendix D) we used a submatrix of size $l = 15$ and a Lanczos step of $\delta_L = 10^{-6}$.

We focus on the octahedral to icosahedral (FCC-ICO) transition: observing this passage using a direct MD or a standard TPS would require a considerable amount of CPU time (about 10^5h, see [35]) as the FCC configuration is at low temperatures the most stable one, so that the system rarely escapes from the FCC basin. In contrast, with our biased TPS technique we were able to observe the first FCC-ICO reactive trajectories after about 300 Markov chain steps.

To ensure that reactive paths start in the stable FCC state, we include in the path probability weight the constraining function (see Eq. (3.48))

$$\varphi^{FCC}(\mathbf{x}_0) = \exp\left\{-\frac{\kappa}{2}\left(Q_4(\mathbf{x}_0) - Q_4^{FCC}\right)^2\right\} \tag{3.91}$$

assigned to the starting state $\mathbf{x}_0$ of the path, function of the bond order parameter Q_4 and centered on the value $Q_4^{FCC} = 0.18$. We set $\kappa = 500$, a sufficiently small stiffness that lets the trajectory starting point span the whole FCC basin. The function φ^{FCC} keeps the beginning of the trajectories inside the FCC funnel, thus counterbalancing the effect of the local Lyapunov bias, that would pull trajectories on barriers.

We present in Fig. 3.5 histograms for the first and the last point of the trajectories, for different values of the control parameter α at the FCC-ICO cohexistence temperature $T = 0.12$. As α values increase, trajectories explore regions that are increasingly distant from the initial FCC basin, and some of them eventually cross the transition region and reach the ICO basin.

Once reaction paths have been identified, the computation of the inter-funnel reaction constant by the correlation function of Sec. 3.4 via Eq. (3.77) is possible if reactants and products basins are adjacent, i.e. if there is no intermediate state between them. [75, 63] However, this hypothesis is not valid for the FCC-ICO transition: several results reported in the literature [26, 30] show that reactive paths linking FCC and ICO states pass through many short-lived metastable basins, separated by barriers of different heights, not belonging to the two main funnels. These metastable states and transition regions have also been observed in a previous work using the transition current sampling method. [88] Such a feature has been confirmed as well by an attentive analysis of our trajectories.

Among all the intermediate metastable states, we emphasize the presence of a basin related to a faulted FCC configuration, having a bond order parameter value around $Q_4 = 0.12$, indicated in the following with D and already acknowledged in precedent studies [24, 30, 88]. This basin has a rather important occupation probability if compared to other metastable configurations, and is visited by every reaction path linking FCC to ICO state. Moreover, this metastable state is indeed configurationally related to the FCC basin, and

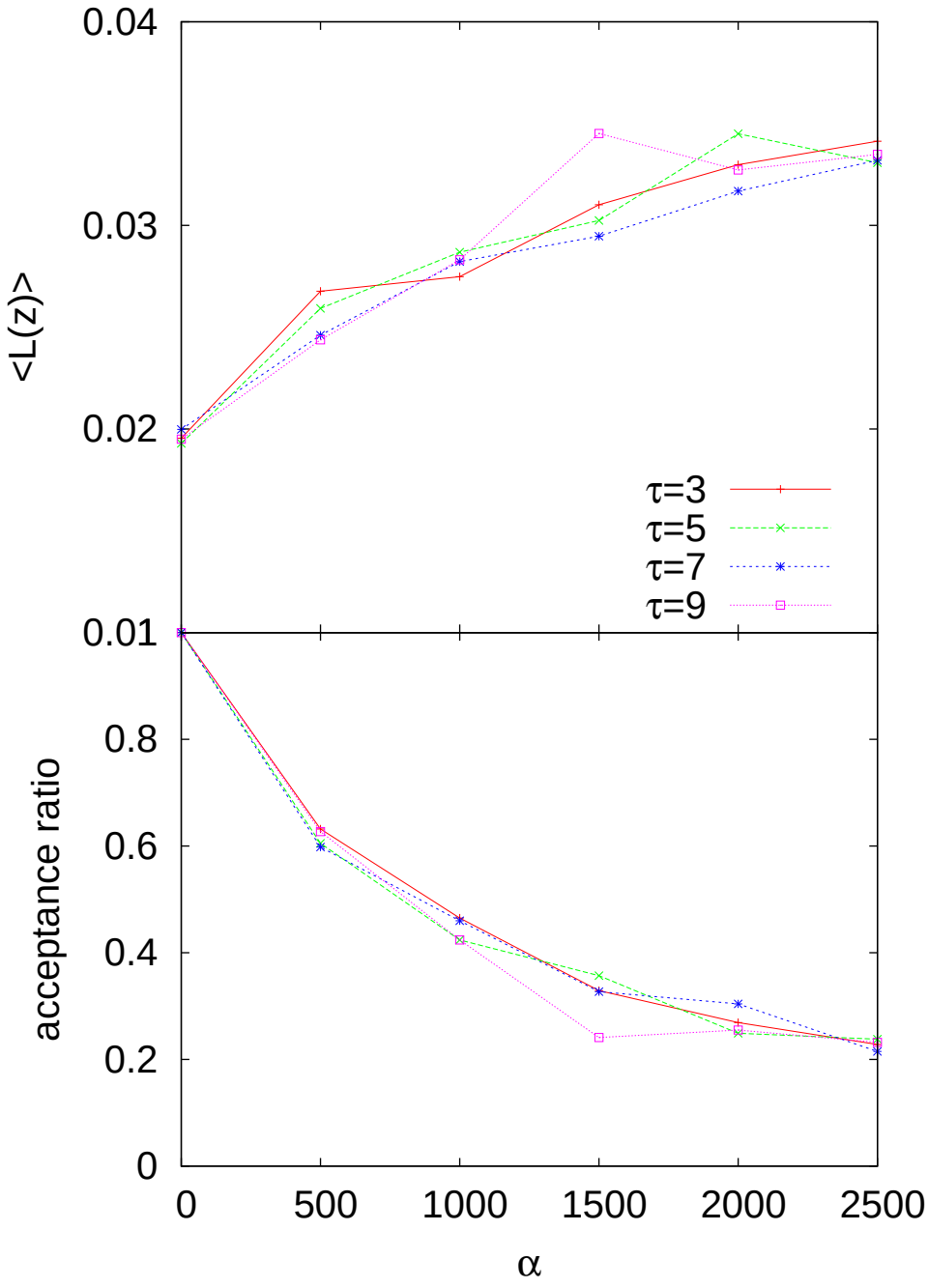

Figure 3.3: **Top**: Average value of the Lyapunov indicator $L(\mathbf{z})$ over a Markov chain of 1000 trajectories, starting from the FCC basin at $T = 0.12$, as function of the control parameter α used in the simulations, for different trajectory lengths τ. Increasing α increases the mean Lyapunov indicator and enables trajectories to explore barriers and transition states. Average Lyapunov indicators are almost independent of the trajectory length τ. **Bottom**: Acceptance ratio, given by Eq. (3.62) for the same simulations.

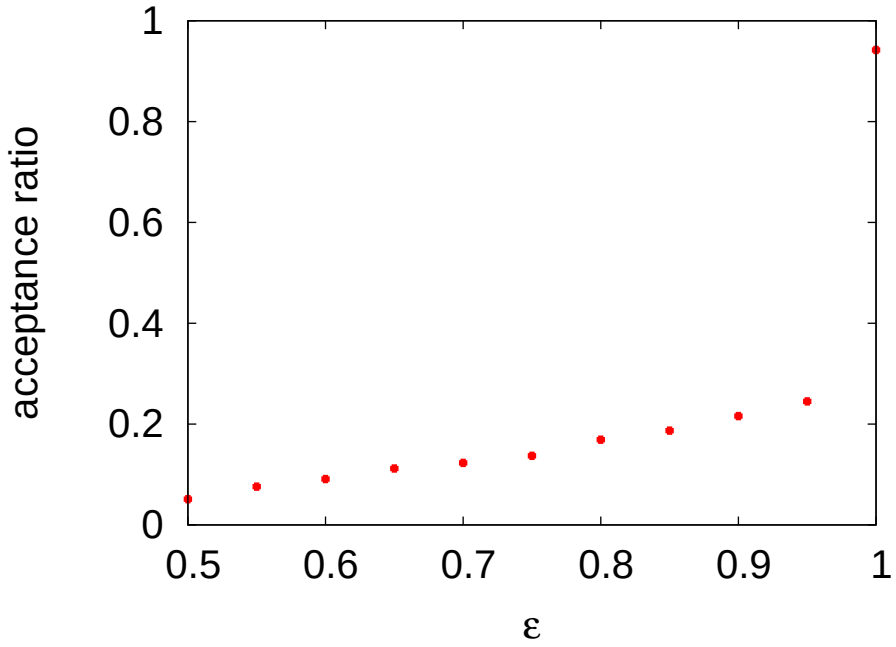

Figure 3.4: Acceptance ratio (Eq. (3.62)) as a function of the parameter ε in the Stoltz algorithm, Eq. (3.50), for a Markov chain of 1000 trajectories, starting from the FCC basin at $T = 0.12$, with trajectory lengths $\tau = 500$ and a control parameter set to $\alpha = 2000$.

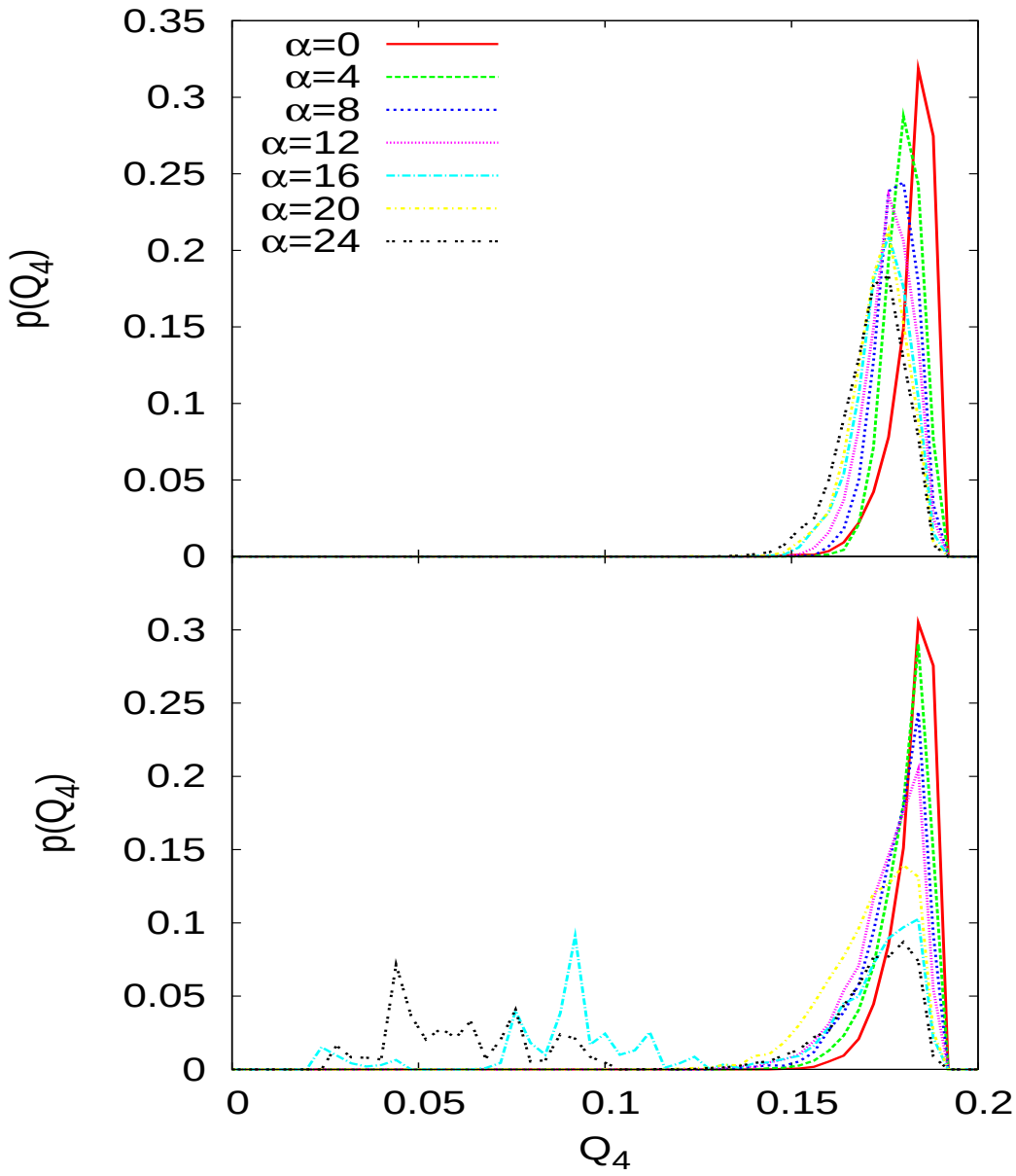

Figure 3.5: **Top**: Histogram of the initial point position $\mathbf{x}_0$ for trajectories starting from the FCC basin at $T = 0.12$ for different values of the control parameter α, averaged on a Markov chain of 5000 steps. The restraining function of Eq. (3.91) mantains the initial states of the trajectories in the FCC funnel for all α values. **Bottom**: Same histogram, for the final position $\mathbf{x}_\tau$. Trajectories sampled with large α values escape the FCC funnel more often. Their final states are distributed over the whole FCC-ICO range.

the barrier separating the D structure from FCC is lower than the one separating the former from ICO state. As a result, several recrossing events of trajectories starting in FCC, visiting the D state and then going back to FCC, can be observed.

Hence, in order to correctly reconstruct the FCC to ICO transition paths, we have to take into account this intermediate metabasin. We therefore split the FCC-ICO passage in two steps: the first part is given by the passage from the FCC basin to the D basin corresponding to $Q_4 = 0.12$. The second part is then given by trajectories starting from the D configuration, and ending up in the ICO funnel.

To obtain this second part of FCC-ICO reactive paths, we constrain the first point of the trajectories to start in the D metabasin, using as in Eq. (3.47) a constraining function given by an indicator on the bond-order parameter value $Q_4(\mathbf{x}_0)$:

$$h_d(Q_4) = \begin{cases} 1 & 0.10 \leq Q_4 \leq 0.13 \\ 0 & \text{elsewhere} \end{cases} \tag{3.92}$$

In Fig. 3.6 we present histograms for the distribution of the beginning and the end point of trajectories constrained with the indicator function of Eq. (3.92), at a temperature $T = 0.13$ slightly above the solid-solid cohexistence. Paths sampled with the unbiased distribution $\alpha = 0$ completely remain in the "window" given by $h_d(Q_4(\mathbf{x}_0))$. On the contrary, trajectories weighted with a Lyapunov bias tend to leave the metabasin: their starting points $\mathbf{x}_0$ tend to accumulate on the borders of the region defined by the indicator function in Eq. (3.92), while the end points $\mathbf{x}_\tau$ are lead to explore both the FCC and the ICO funnels.

In simulations performed at lower temperatures, this reconstruction of the second part of the FCC-ICO reactive path with trajectories starting from the D state is more difficult. Indeed, histograms for trajectories of the same length at temperatures lower than the solid-solid transition $T = 0.12$ show that an important fraction of the sampled trajectories fall from the D state directly to the FCC basin, while a few trajectories end in the ICO state. This is attributed to the heights of the barriers separating the metastable D structure from either the stable ICO or stable FCC structures, the latter barrier being lower than the former one.

3.5.3 FCC-ICO reaction constants

The total reaction constants for the two-step FCC-ICO transition, assuming a steady occupation probability for the intermediate D state, is derived in Appendix F.1.1 and reads

$$k_{F\to I} = \frac{k_{F\to d} k_{d\to I}}{(k_{d\to F} + k_{d\to I})} \tag{3.93}$$

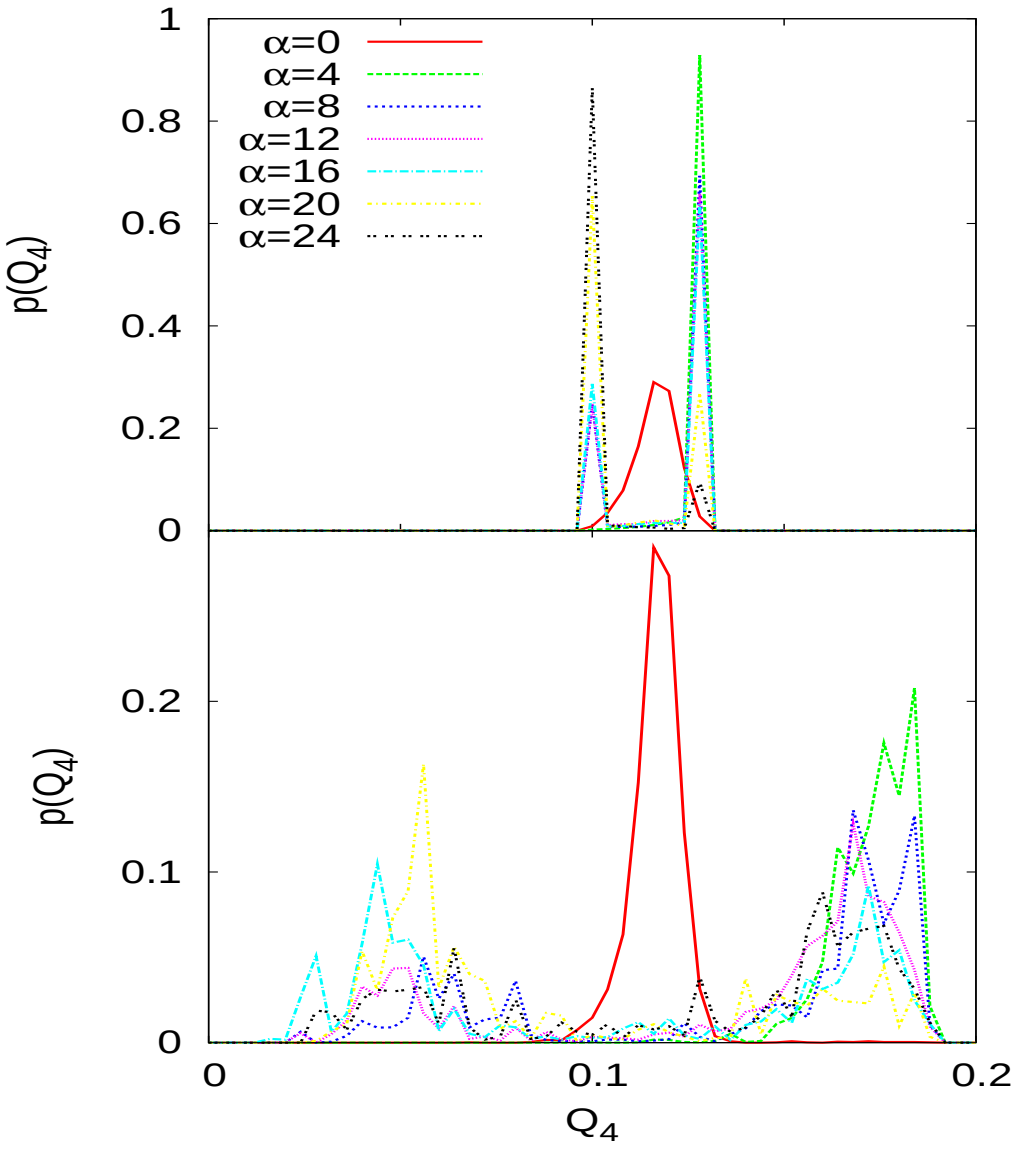

Figure 3.6: **Top**: Histogram of the initial configuration $\mathbf{x}_0$ for trajectories starting from the D configuration metabasin located at $T = 0.13$ for different values of the control parameter α, averaged over a Markov chain of 5000 steps. **Bottom**: Same histogram, for the final position $\mathbf{x}_\tau$. Trajectories end up in both the FCC or the ICO funnel.

where subscripts F, d and I refers to FCC, D and ICO states respectively. The same steady approximation is assumed for all intermediate metastable states in discrete path sampling studies. [2, 37, 41]

Reaction rates $k_{F\to d}$ and $k_{d\to I}$ involve transitions between states separated by high free energy barriers, [88] thus the hypothesis of time scale separation required by the reaction rate theory is still valid, and reaction constants can be computed using the method exposed in Sec. F. Reactive paths between FCC and D configuration, and from this last one and ICO, are computed as reported above (Sec. 3.5.2).

On the contrary, the D to FCC reaction rate $k_{d\to F}$ cannot be computed by Ly-TPS, because the requirement of a time scale separation is no longer valid, the barrier separating this two states being too low. It is therefore computed by direct MD simulation.

The reactivity $\mathcal{A}$ (Eq. (3.81)) for each trajectory is evaluated in simulations distinguishing the three basins FCC, ICO and D whose ranges of bond-order parameter Q_4 value, that is $0.13 < Q_4 < 0.18$, $0 < Q_4 < 0.04$ and $0.1 < Q_4 < 0.13$, respectively. Data harvested during LyTPS runs are unbiased using MBAR.

In Fig. 3.7 and 3.8, two examples of population correlation functions for the computation of reaction rate constants, unbiased with MBAR, are reported. Note that reactivity values computed at short times are nearly zero, and do not contribute significatively to the correlation functions: in fact, these values are obtained from segments of trajectories too short to witness a complete transition between two states. In Table 3.1, we report reaction rate values for the FCC to D structure ($k_{F\to d}$) and D structure to ICO ($k_{d\to I}$) reaction constants, that give, through Eq. (3.93), a total FCC to ICO ($k_{F\to I}$) rate in good agreement with values given by DPS calculations [37, 41]. Finally, an Arrhenius plot comparing our results with the reaction constants proposed in Ref. [37, 2] is presented in Fig. 3.10.

We conclude this section pointing out the importance of WR in the correct estimation of reaction constants. As recalled, WR allows to take into account the information contained in the whole buffer trajectory ζ: hence, it is possible to compute also contributions given by reactivity values of trajectories that will be rejected at the shifting move. We present in Fig. 3.9 the time correlation function for LyTPS simulations of the passage from the FCC to the D state at $T = 0.13$, already presented in Fig. 3.7 (top), computed with and without resorting to WR. Both simulations are based on the same Markov chain, and are derived using MBAR method. In this last case, input weights and reactivities for MBAR are given only by the probability weights of the trajectory selected after the shifting move. The difference between the two correlation functions amounts to a factor 3, hence contribution of the selected trajectory to the WR correlation function amounts to a third of the total (we recall that the buffer trajectory ζ contains $\mathcal{N}$ trajectories). However, they strongly differ qualitatively, as the trend of $C(t)$ computed without resorting to WR clearly indicates a poor statistic on the reactivity values given only by the selected trajectory. This can be

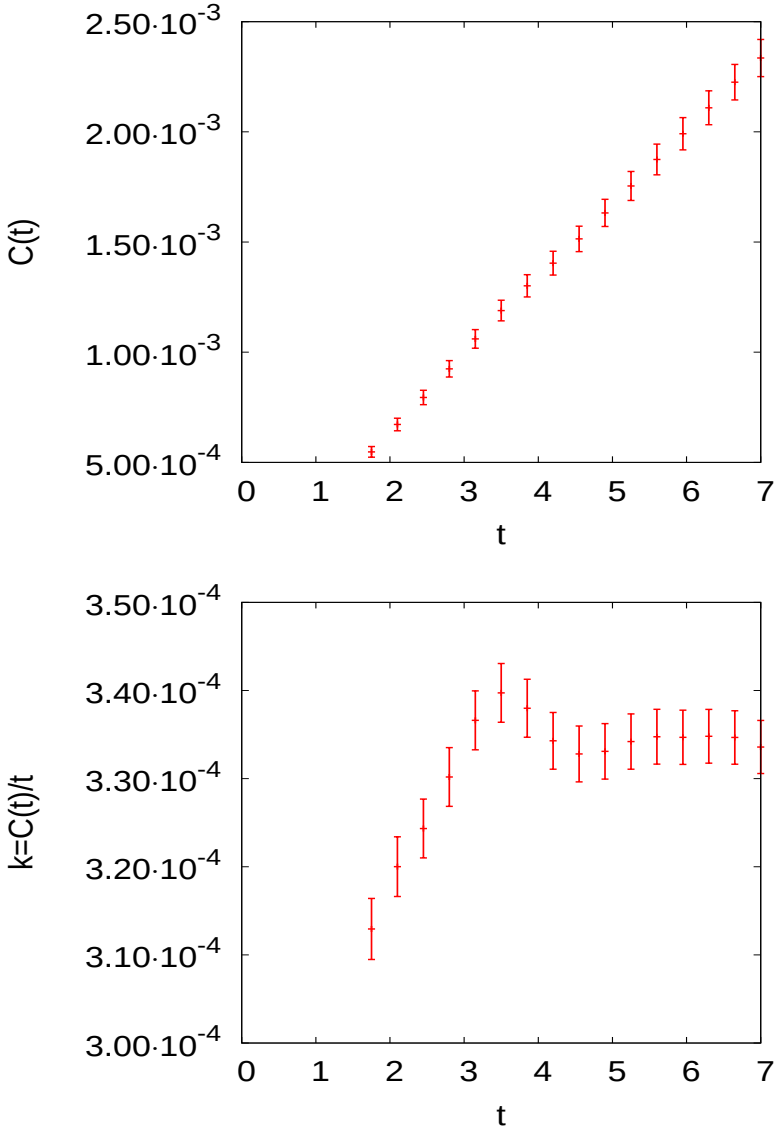

Figure 3.7: **Top**: Correlation function for the transition from FCC to D basin, at $T = 0.13$. **Bottom**: Reaction constant for this same passage, obtained at times shorter than the first mean passage time. The reactive flux $k(t)$ reaches a plateau value, corresponding to $k_{F\to d}$, as explained in Sec. F. Note that we have no statistics for times below $t = 1$, as trajectories of this duration are too short to join the D state.

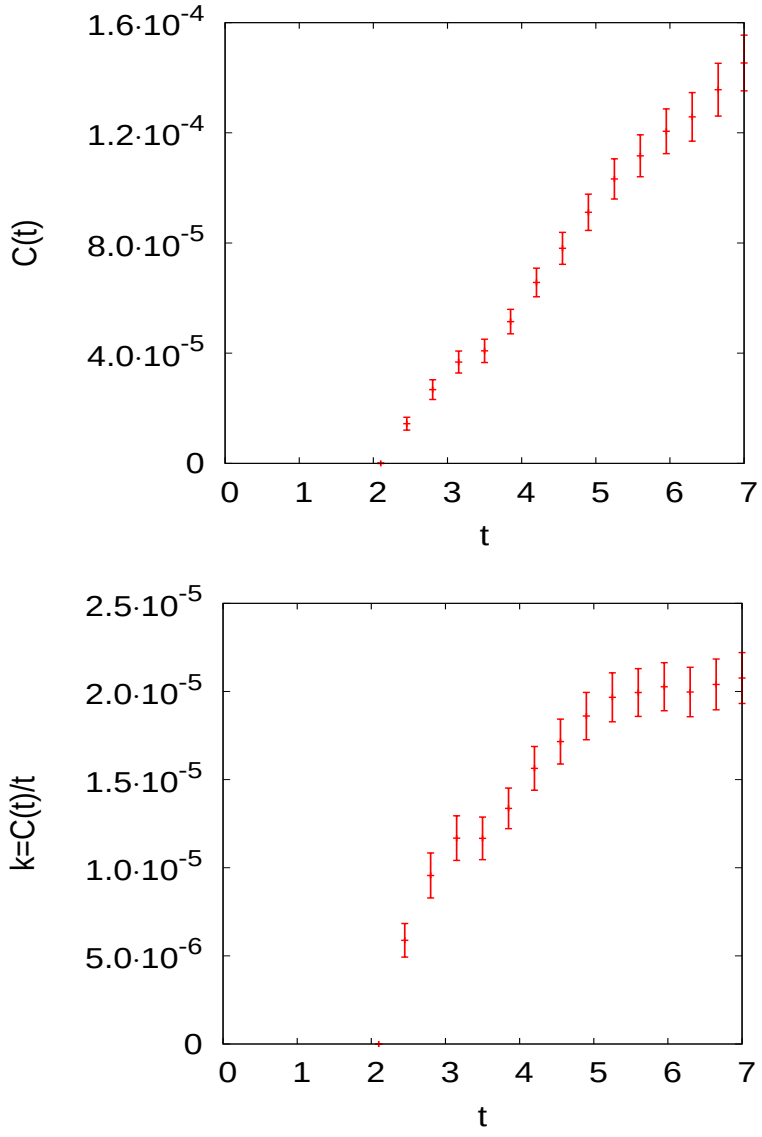

Figure 3.8: **Top**: Correlation function for the D to ICO transition, at $T = 0.13$. **Bottom**: Reaction constant for this same passage.

T	$k_{F\to d}$	$k_{d\to I}$	$k_{F\to I}$	$k_{F\to I}$ (Ref. [2])
0.10	$1.2\ 10^{-7}$	$1.4\ 10^{-7}$	$8.1\ 10^{-14}$	$2.5\ 10^{-13}$
0.11	$1.3\ 10^{-5}$	$2.5\ 10^{-7}$	$1.08\ 10^{-11}$	$1.15\ 10^{-11}$
0.12	$8.1\ 10^{-5}$	$4.0\ 10^{-7}$	$1.2\ 10^{-10}$	$2.82\ 10^{-10}$
0.13	$3.3\ 10^{-4}$	$2.0\ 10^{-5}$	$6.6\ 10^{-9}$	$4.2\ 10^{-9}$
0.14	$9.3\ 10^{-4}$	$4.5\ 10^{-5}$	$4.3\ 10^{-8}$	$4.3\ 10^{-8}$
0.15	$2.4\ 10^{-3}$	$2.4\ 10^{-4}$	$5.7\ 10^{-7}$	$3.2\ 10^{-7}$

Table 3.1: Table of reaction constants for the transitions FCC to D structure, D to ICO, and the total FCC to ICO transition, indicated as $k_{F\to d}$, $k_{d\to I}$ and $k_{F\to I}$ respectively, at different temperatures. Values of $k_{F\to I}$ are obtained using Eq. (3.93) and assuming the reaction constants $k_{d\to F}$ as 10^{-2}, $3\cdot 10^{-2}$, 10^{-1} for $T = 0.10$, $T = 0.11$ and $T = 0.12$ respectively (values obtained by Langevin MD), and unitary for $T \geq 0.12$. In the last column on the right, we report Discrete Path Sampling data from Ref. [2], computed in the harmonic approximation.

explained considering that the length of ζ is double of the selected trajectory, therefore in ζ can be contained trajectories that are reactive, but are partly lying in one of the two basins, thus having however a Lyapunov indicator lower than the selected path. This amounts to say that, for a given duration t, the selected trajectory is the one settling for the most of his length in the transition region, where the Lyapunov indicator his larger, while there can be reactive trajectories just partially crossing the barrier, and then falling down in one of the two states, thus recovering a lower $L(z)$. These trajectories are then rejected, but their reactivity contribution should be taken as well into account: this is successfully done within a WR framework. Moreover, we show in Fig. 3.7 (bottom) that the difference between standard deviation values for $C(t)$ computed with and without WR: in agreement with Ref. [94], WR values are lower of about 30%.

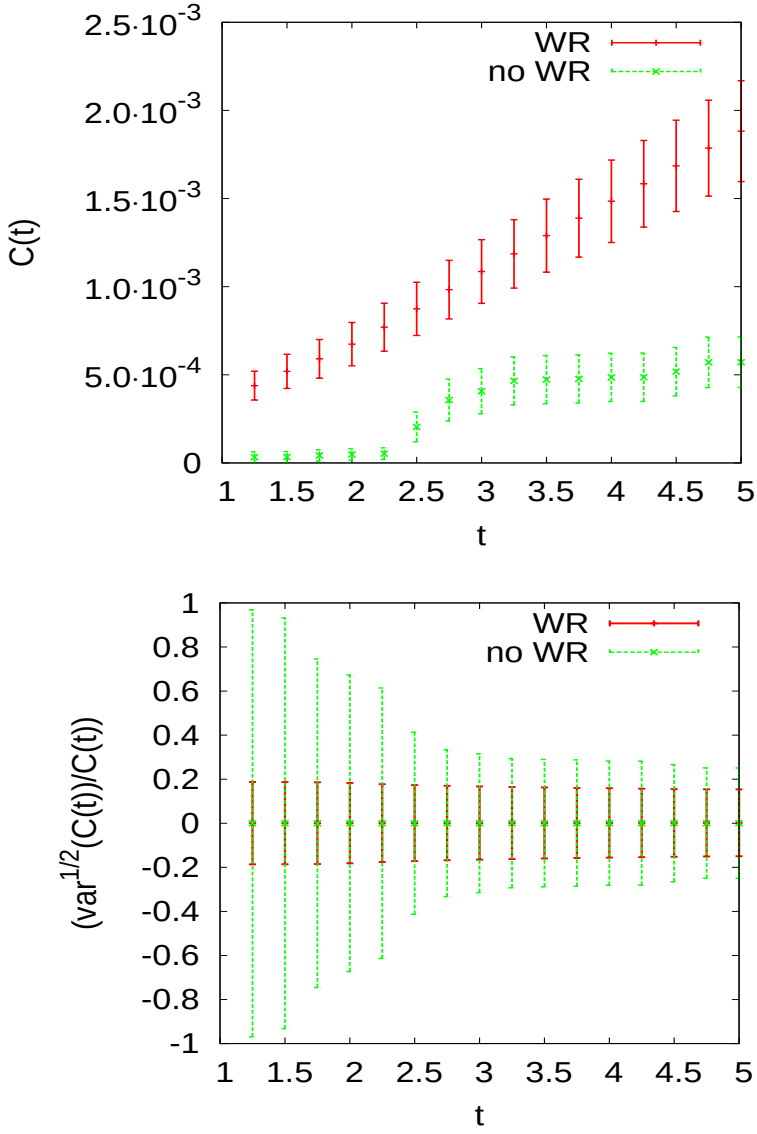

Figure 3.9: **Top**: Correlation function for the FCC to D configuration passage, at $T = 0.13$, with or without WR. **Bottom**: Standard deviations over averages for the correlation function computed with and without WR (see Eq. (3.90) and Appendix F).

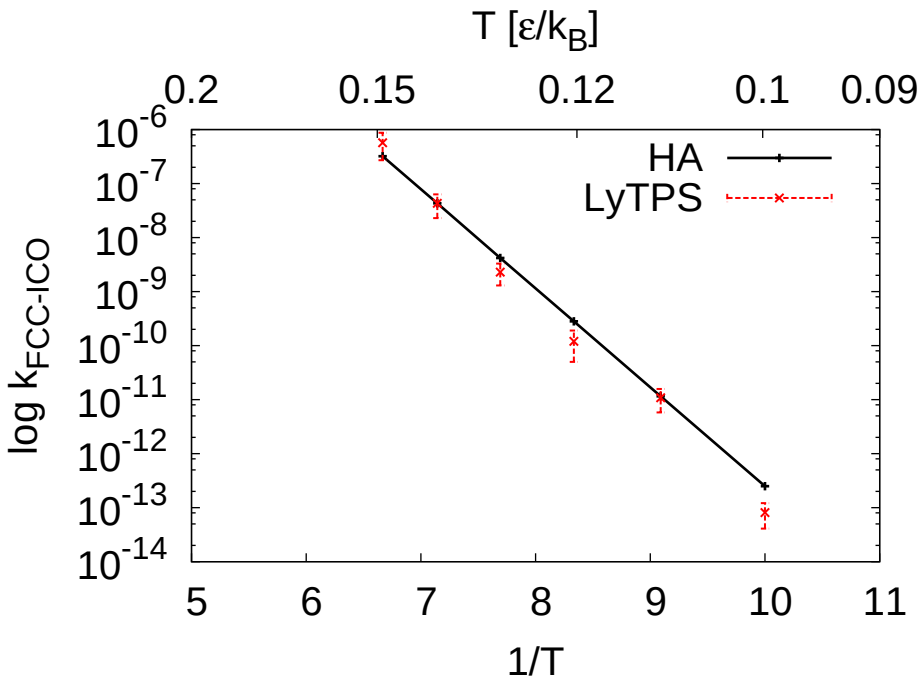

Figure 3.10: Arrhenius plot for the FCC to ICO reaction rate from Table 3.1 (LyTPS, red dots), compared with data obtained with Discrete Path Sampling [37] in the harmonic approximation (HA, black line) and reported in Ref. [2].

3.6 Conclusion

The method presented in this chapter allows to compute reaction rate constants for inter funnel transitions in many-body systems. The reaction rate values are evaluated using a path sampling algorithm biased with local Lyapunov numbers. This bias is introduced with the aim of accelerating the sampling of reactive paths, thus requiring shorter Markov chains and a limited amount of CPU time to observe activated processes.

We tested these features by observing reaction paths and evaluating equilibrium rates for structural transitions in the LJ_{38} system and for vacancy migration in an α-Iron crystal. For both systems, we were able to predict phenomenological rate constants, in very good agreement with data already given in the litterature in the case of LJ_{38}.

The Lyapunov biased TPS method presents several advantages, and incorporates features of different rare events simulation methods.

Firstly, with respect to other importance sampling methods based on Lyapunov weighted sampling [15, 48], Lyapunov biased TPS has the main advantage of a simpler implementation. This is due to the Lyapunov indicator $L(\mathbf{z})$ we propose in Eq. (3.35), that allows to quantify the chaoticity properties of the hamiltonian trajectories by re-

sorting to local Lyapunov numbers. These quantities can be easily calculated with an appropriate and fast method to compute the eigenvalues of the Jacobian matrix of the hamiltonian mapping, like the Lanczos algorithm, that demands a limited computational cost. As recalled in Sec. (3.2.2), resorting to local Lyapunov numbers to evaluate chaoticity of phase space trajectories doesn't suffer from the computational drawbacks of other algorithms aimed at the same purpose, as RLI or the tangent space method. [48] The implementation of shooting and shifting Monte Carlo moves in a Lyapunov biased TPS results therefore much less complicated, and computationally less expensive, than the way proposed in Ref. [48] with the use of RLI, because we do not need to compute four trajectories to evaluate the chaoticity of a single path [61, 48].

Secondly, this formulation for the Lyapunov indicator is such that the bias applied to each path in order to enhance the fraction of reactive trajectories is clearly identified, differently from bias depending on rather complex cloning algorithms like the one proposed in Lyapunov weighted dynamics [15] and transition current sampling [88]. Hence, the use of standard unbiasing statistical tools to recover unbiased observables is possible with a small theoretical and computational effort.

Furthermore, we consider the access to the evaluation of equilibrium transition rates as the most important aspect of Lyapunov biased TPS. On the computational point of view, the direct access to reaction rates without resorting to a distinct evaluation of the reaction barriers and the transmission factor, as usually done in standard TPS technique [3], is a very advantageous feature. To unbias reaction constants computed in Lyapunov biased ensembles we chose among other unbiasing algorithm, like WHAM [99] or Extended Bridge Sampling [100] techniques, the MBAR method [66]. MBAR has proven to be computationally efficient and to give an adequate numerical precision in estimating reaction constants. Moreover, this work is the first in which MBAR is implemented exploiting the marginal probability derived from a waste recycling method.

Finally, this biased path sampling is performed at a finite temperature, imposed to trajectories by the canonical distribution from which the path starting point is selected and maintained along the path thanks to the Stoltz proposal for the shooting algorithm, see Sec. 3.3.2. In parallel, the Lyapunov indicator used as a bias to select reactive paths directly links the path sampling to the local conformation of the potential energy surface via the hessian matrix, thus giving to our method an intrinsic dependence on the potential energy landscape. The coupling between a finite-temperature sampling and potential energy surface conformation is a noticeable improvement if compared to eigenvector-following methods, that are based on the shape of the potential energy surface, but usually operate at zero temperature. Lyapunov biased TPS can be acknowledged as a finite, nonzero temperature version of the well-known eigenvector-following techniques, such as Dimer, Optim or ART. [55, 56]

The advantages related to a finite temperature technique do not concern only the exploration of the energy landscape, but also the fact that the evaluation of physical observables like reaction rates takes into account temperature and anharmonicity effects. Indeed, the phenomenological reaction rate we computed (see Sec. 3.4) can be compared with experimental measures: Lyapunov biased TPS turns out to be a powerful tool in many condensed matter problems, like vacancy migration, where reaction rates are usually estimated using only the *potential energy* barriers and harmonic approximations give poor results with respect to experimental data obtained at nonzero temperatures.

We conclude observing that this method can be implemented for the computation of reaction rates in more complex condensed matter systems, and can find interesting applications in a wide class of research fields, spanning from molecular biophysics to physical metallurgy, where the numerical determination of reaction rates has important consequences for experimental applications.

For these reasons, we present in the next Chapter the use of LyTPS to evaluate vacancy migration rates in bcc crystals, and show how these rates have important applications in material science.

Chapter 4

Rate constants for point defect migration in α-Fe

Contents

4.1 Thermally activated processes in nuclear materials 84
4.1.1 Numerical methods for irradiated materials study 85
4.2 Vacancy and vacancy clusters migration mechanisms 86
4.3 Reaction rate theory for point defects migration 86
4.3.1 Thermodynamics of Point Defect Formation 87
4.3.2 Microscopic description of diffusion 90
4.3.3 Jump frequency 92
4.3.4 Diffusion coefficient 95
4.4 Migration rate estimates with LyTPS 95
4.4.1 Vacancy migration in α-Iron crystal with LyTPS 96
4.4.2 Divacancy migration in α-Iron crystal 100
4.5 Resistivity recovery experiments 102
4.6 Conclusion 107

The occurrence of rare events in physical systems of nuclear interest is the one of main reason of this PhD thesis. Indeed, the methods developed and presented in the two previous chapters can be applied in the study of physical processes concerning materials post-irradiation. These processes, that we study here from an atomistic point of view, have indeed important consequences on the structural behavior of nuclear plants components. In order to clarify this point, we first present in these Chapter a description of thermally activated events in nuclear materials. We then focus on the mechanism of vacancy migration, that is for his physical features by far the most significative example of such activated processes.

Finally, we present an application of the LyTPS method exposed in Chapter 3 to the computation of point defect migration rates: we calculate reaction rates for the migration of vacancies and divacancies in an α-Iron crystal, for temperatures ranging from 300 K

to 850 K. Vacancy and divacancy diffusion rates associated with activation barriers at finite temperature are then evaluated, and shown to be substantially different from values previously reported in the literature and obtained using zero-temperature and standard harmonic approximations.

In Sec. 4.4 we present results for migration rates for vacancies and divacancies in α-Fe obtained employing the transition path sampling method with a local Lyapunov bias (LyTPS) exposed in Chapter 3. These rates are then employed as input parameters for computational codes of Kinetic Monte Carlo type, aimed at the numerical simulation of the microstructural evolution of materials after irradiation. In particular, we use these migration rates for reproducing numerically resistivity recovery experiments.

4.1 Thermally activated processes in nuclear materials

Following the presentation of the book by Was [104] (from which large excerpts are taken for this introductory part), we here recall the fundamentals of physical metallurgy. Changes in microstructure and mechanical properties of nuclear materials are governed by the kinetics of defects produced by irradiation [101]. Indeed, the interaction of an energetic incident particle - like electrons, or neutrons in nuclear reactor vessels - with a lattice atom determines the transfer of a given amount of energy to this atom, that is subsequently displaced from its lattice site and, moving through the crystal, produces a displacement cascade, i.e. a series of point defects (vacancies and interstitials, i.e. isolated Frenkel pairs) and clusters of these defects in the crystal lattice. The most simple model that approximates the irradiation event is the collision of hard spheres with displacement occurring when the transferred energy is high enough to hit atom off its lattice site. In addition to energy transfer by hard-sphere collisions, the moving atom loses energy by several other physical mechanisms, like interactions with electrons, the Coulomb field of nearby atoms, the periodicity of the crystalline lattice, etc.

The radiation damage event is defined as the transfer of energy from the incident projectile to the solid and the resulting distribution of target atoms after completion of the event [104]. This chain of events happens in about 10^{-11}s. After the thermal spike due the energetic particle interaction with the crystal lattice, the irradiated material recovers its initial temperature, but presents a large amount of point defects caused by the cascade. Subsequent events, involving the migration of the point defects and defect clusters and the additional clustering or dissolution of the clusters, are classified as radiation damage effects. The migration of these individual defects yields either to their recombination or to the formation of vacancy or interstitial clusters, and is heavily responsible of the transformation of mechanical properties of the crystal. The microstructural evolution induced by irradiation in due to these mechanisms and it has marked effects on the mechanical

properties. These phenomena are of primary importance for the ageing of materials in the nuclear industry.

As these migration events occur at temperatures much lower than the thermal spike, they involve crossing barriers that are larger than the actual thermal energy of the system: hence, post-cascade defect migration can be considered as a thermally activated rare events, then studied using the methods we introduced in the Chapters 2 and 3.

We first recall the properties of point defects and the mechanisms of migration, following Ref. [104], before exposing the reaction rate theory for point defect migration [110]. We then give some details on current simulation methods aimed to reproduce radiation damage.

4.1.1 Numerical methods for irradiated materials study

A precise analytical description of radiation damage can be only very limited, due to the complexity of this phenomena. Computer simulations are therefore necessary to study and predict results experimentally observed with techniques like transmission electron microscopy, X-ray scattering, small angle neutron scattering and positron annihilation spectroscopy. [104]

Two tipes of numerical methods are usually employed to simulate the complete radiation damage process: molecular dynamics (MD) simulations and kinetic Monte Carlo (KMC).

MD is computationally intensive and adequate for modeling atomic systems on the appropriate scale for the simulation of displacement cascades. It provides the most realistic description of atomic interactions in cascades, once adequate interatomic potentials are used, like the Embedded Atom Model potentials described in Appendix G. MD simulation time steps are very small (5 to 10 fs), so MD simulations are generally run for no more than $100ps$. This demand of a large CPU time limits the predicting capabilities of MD simulation. However, molecular dynamics provides a detailed view of the spatial extent of the damage process on an atomic level that is not possible by other techniques.

To bypass this numerical time-scale bottleneck in MD simulations, it is possible to use kinetic Monte Carlo (KMC). KMC is the most powerful approach available for making dynamical predictions at the mesoscopic scale: it attempts to overcome the MD time limitation by exploiting the fact that the long-time dynamics of this kind of system typically consists of diffusive jumps from state to state (see Sec. 4.3). Rather than following particle trajectories, KMC offers a way to propagate dynamically correct trajectories through the state space. The result is that KMC can reach vastly longer time-scales, typically seconds and often well beyond. However, this requires a set of rate constants connecting the states of the system. These rates have to be accurate enough to coherently reproduce experimental data with numerical simulations: for this reason, we will use in Sec. 4.4 LyTPS to compute phenomenological reaction rates for vacancy migration.

Taken together, the MD and KMC methods cover the radiation damage time-scale.

MD simulations are practical up to the ns range, and KMC simulations extend the range to the seconds regime. Much occurs after this time-scale and this is generally modeled using rate theory.

4.2 Vacancy and vacancy clusters migration mechanisms

Understanding the effects of irradiation on materials requires a description of the nature of radiation damage on the atomic level. The recoiling lattice atom travels through the crystal, colliding with its neighbors and displacing these ones from their sites. As recalled cascade of atomic collisions created by the original particle ends in a number of vacant lattice sites and an equal number of displaced atoms positioned in the interstices of the lattice. These are called Frenkel pairs, and mainly recombine after irradiation. The basic defects (vacancies and interstitials) that remain in the crystal form the foundation for all observed effects of irradiation on the physical and mechanical properties of materials. We focus here on vacancies.

The vacancy, or missing lattice atom, is the simplest point defect in metal lattices. All calculations and computer simulations show that the single vacancy structure is a missing lattice atom with the nearest neighbors relaxing inward toward the vacancy.

Vacancies have low formation energies ($< 2eV$) and high migration energy ($> 0.5eV$) and are therefore much less mobile than interstitials. Beside monovacancies are the vacancies aggregates and cluster (such as divacancies, trivacancies etc.) that are often observed in irradiated metals.The migration energy of divacancies is less than for single vacancies but increases with increasing cluster size. It appears that since the tetra-vacancy can only migrate by dissociation, it is the first stable nucleus for further clustering.

The vacancy diffusion mechanism is one of the most important. It is the simplest mechanism of diffusion and occurs in metals and alloys. It is given by the jump of an atom from its lattice site to a neighboring vacant site. Since movement of the vacancy is opposite that of the atom, vacancy-type diffusion is regarded as either a movement of the atom or the equivalent movement of the vacancy. The absence of an atom from its lattice site (i.e., the vacancy) allow atoms to move rather easily with jumps to nearest neighbor or next nearest neighbor.

4.3 Reaction rate theory for point defects migration

The motion of an atomic defect in a solid can be described as the motion of a particle interacting with neighboring atoms via an effective potential (see Appendix G). The solid in which this processes occur is assumed at thermal equilibrium at a given temperature T, and atoms in the lattice are in a constant state of motion due to thermal vibration: this

means that point defects in the lattice are also in motion, i.e. the migrating particle is in principle submitted to lattice vibrations [104].

The mean amplitude of these vibrations is in general small if compared to the displacement required to the particle to go from one the initial stable configuration, in a potential energy minimum, to an unstable configuration corresponding to a saddle point separating the initial configuration to the closest stable one. The simplest approximation is here to suppose that jumping particle are isolated enough from each other, in order to make the reasonable assumption of single particle jump.

The random nature of thermal vibration gives rise to random walk of the atoms via the defects that are in thermal equilibrium with their surroundings, known as self-diffusion. Self-diffusion arises when a local concentration gradient of defects appears in the crystal, driving atoms to move in the direction that eliminates the gradient.

The behavior of point defects is usually described resorting to the formation and the migration energies. The formation energy is defined as the energy difference between the system with and without defect, at constant number of atoms. The migration energy is, by definition, the difference between the energy of the system at the saddle point and in a equilibrium minimum [104]. Finally, the binding energy between two defects is the difference between the formation energy of the system when the two involved defects are far apart and close to each other, according to the specified configuration: positive binding energies denote, therefore, attraction (the energy decreases by putting the defects together), while negative binding energies denote repulsion (the energy increases by putting the the defects together).

We recall in this section the basic ideas of defect migration in solids, focusing on vacancies, both treating this subjet from the macroscopic (thermodynamics) and microscopic points of view.

4.3.1 Thermodynamics of Point Defect Formation

Self diffusion requires, as a first condition, the presence of point defects, that allows crystal atoms to move without large distortions of the crystal lattice. We therefore derive first the concentration of point defects in a crystal at thermal equilibrium, i.e. after the thermal spike due to irradiation is recovered, giving an expression for the formation energy.

Even in the absence of irradiation, indeed, a crystal presents a finite number of defects. Statistically, there is a finite probability that sufficient energy will be concentrated, by local fluctuations, to form a defect in the crystal lattice. The Gibbs free energy (or free enthalpy) reads

$$G = E + p_{ext}V - TS = H - TS \tag{4.1}$$

If we assume that the volume of the crystal is constant, this expression is equivalent to the Helmholtz free energy function.

In Eq. (4.1), E is the internal energy, H is the total enthalpy of the N atoms comprising the system. The entropy S reads

$$S = k_B \ln w \tag{4.2}$$

where w is the number of possible different configurations of atoms. For a crystal with n defects and N available sites, the increase in free energy is

$$\Delta G_f = n\Delta H_f - T\Delta S \tag{4.3}$$

where ΔH_f is the increase in enthalpy brought about by the formation of the defect and ΔS is the change in total entropy, determined as follows. For n defects, there are N for the first, $N-1$ for the second, up to $N-n+1$ for the n-th. Because these configurations are not all distinct and defects are indistinguishable, the number above allows for $n!$ ways of distributing N defects among n sites. Hence, the number of possible different configurations is

$$w = \frac{N!}{n!(N-n)!}. \tag{4.4}$$

Using Stirling's approximation $lnx! \approx x \ln x$, the mixing entropy is then

$$S_{mix} = [N \ln N - n \ln n - (N-n)\ln(N-n)] \tag{4.5}$$

In addition to S_{mix} there is a contribution to S from the vibrational disorder of the presence of the defects.

We now use introduce an harmonic approximation to take into account the entropy contribution due to lattice vibration. According to the Einstein model of lattice motion, the atoms are represented as $3N$ independent linear harmonic oscillators (harmonic approximation, that works fairly well in most cases up to the melting point) and the associated entropy is:

$$S_f \approx 3k_B \ln\left(\frac{k_B T}{\hbar\omega_E}\right) \tag{4.6}$$

where ω_E is the natural frequency of the oscillator and $\hbar$ is Planck's constant, and we assumed $\hbar\omega_E/k_B T \ll 1$ If each defect changes the vibration frequency of z neighbors to ω_r, the entropy variation due to vibrational disorder of n defects is:

$$n(S_f - zS_f) = S_f = 3k_B nz \ln\left(\frac{\omega_E}{\omega_r}\right) \tag{4.7}$$

Taking both contributions to the entropy change and inserting them into the free energy equation gives

$$\Delta G_f = n\Delta H_f - k_B T[N \ln N - n \ln n - (N-n)\ln(N-n) + nz \ln\left(\frac{\omega_E}{\omega_r}\right)] \tag{4.8}$$

In equilibrium, n will be such that it satisfies $\frac{dG_f}{dn} = 0$ giving

$$\frac{\Delta H_f}{k_B T} = \ln\left[\frac{N-n}{n}\left(\frac{\omega_E}{\omega_r}\right)^{3z}\right] \tag{4.9}$$

For $N >> n$, the defect concentration $c_v = n/N$ reads

$$c_v = \left(\frac{\omega_E}{\omega_r}\right)^{3z} \exp\left[-\frac{\Delta H_f}{k_B T}\right] \tag{4.10}$$

or, rewriting in Eq. (4.6) the prefactor given by the vibration frequencies in terms of vibrational entropy, the vacancy concentration with respect to the non defective state reads

$$c_v = \exp(-(G_v - G_0)/k_B T) \tag{4.11}$$

where G_0 is the Gibbs free energy (or free enthalpy) of the perfect crystal.

Alternatively, following Ref. [110] we directly write, always in the quasi harmonic approximation the free enthalpy as

$$G = E + kT \sum_{\alpha=1}^{3N} \log\left(\frac{\hbar\omega}{kT}\right) + p_{ext}V \tag{4.12}$$

where again E is the potential energy of the system, the third term corresponds to the work of the external pressure p_{ext}, and the logarithmic term indicates the *vibrational entropy* obtained summing the non zero 3N normal eigenfrequencies ω, corresponding to normal modes of vibration. The free enthalpy difference in Eq. (4.11) can be written as

$$\Delta G = E_v - E_0 + kT \sum_{\alpha=1}^{3N} \log\left(\frac{\omega_\alpha^v}{\omega_\alpha^0}\right) + p_{ext}(V_v - V_0) \tag{4.13}$$

in which indexes v and 0 indicate the system with or without the vacancy.

The work of Lucas and Schaublin [105] investigate the modes of vibration of the vacancy in bcc Iron and estimate how the vibrational properties can affect the stability of these defects. The vibrational frequencies ω are given by the phonon density of states of the vacancy, and are calculated using density functional theory calculations. The spectra of phonons frequencies ω_i is obtained by diagonalizing the hessian matrix of the pseudopotential. From the phonon density of states, it is possible to estimate the vibration contributions F_{vib} to the free energy at finite temperature T,

$$F_{vib} = E_{vib} - TS_{vib} \tag{4.14}$$

where E_{vib} represents the vibrational internal energy and S_{vib} the vibrational entropy. In the harmonic approximation, these contributions can be written as

$$E_{vib} = \sum_i^{3N} \left[\frac{h\omega_i}{exp\left[\frac{h\omega_i}{k_B T}\right] - 1} + \frac{1}{2}h\omega_i\right] \tag{4.15}$$

and the exact expression for the vibrational entropy

$$S_{vib} = k_B \sum_i^{3N} \left\{ \frac{h\omega_i}{k_B T} \left(\exp\left[\frac{h\omega_i}{k_B T}\right] - 1 \right)^{-1} - \ln\left(1 - \exp\left[-\frac{h\omega_i}{k_B T}\right]\right) \right\} \tag{4.16}$$

The formation energy of the vacancy is found to be 2.16 eV. Calculations gave a vibrational formation entropy of $4.08k_B$. This value is compared by the authors with the value proposed by Seeger, who has estimated the sum of the formation entropy S_f and the migration entropy S_m (see below) around $5k_B$ using transition state theory [106]. Such a large vibrational formation entropy decreases the formation free energy of the vacancy from $2.11eV$ at 0 K to $1.98eV$ at 500K: it is then much easier to form vacancy when temperature increases.

4.3.2 Microscopic description of diffusion

We now pass to the study of the pure diffusive process involved in the vacancy migration. We sketch here a mathematical relation between the macroscopic parameters for diffusion (i.e., the self-diffusion coefficient) and the microscopic process of the elementary acts of defect jumps represented by the coefficients of diffusion for defects, following [110]. The main assumption is that the self-diffusion process consists of a completely random walk of defects.

Jumps of defects (hence, of atoms) are due to thermal vibrations of very high frequency. The Einstein expression for diffusion coefficient of a random walk along the x direction reads

$$D = \frac{\overline{X^2}}{2\tau} \tag{4.17}$$

where $\overline{X^2}$ is the mean square displacement along the x direction for a duration τ, and the overbar denotes an average over a large number of atoms. If X_i is the displacement of the i-th atom, we have

$$\overline{X^2} = \frac{1}{N} \sum_{i=1}^{N} X_i^2 \tag{4.18}$$

where N is the number of diffusing atoms. It is possible to show that

$$\overline{X} = \sum_{k=1}^{K} \overline{x}_k \tag{4.19}$$

and

$$\overline{X^2} = \sum_{k=1}^{n} \overline{x^2}_k + 2 \sum_{k,j} \overline{x}_k \overline{x}_j \tag{4.20}$$

where x_k is the k-th displacement along x, and K is the number of atomic jumps during τ. For a real random walk, the last term in Eq. (4.20) vanishes. However, even when $\overline{X} = 0$,

i.e. in absence of external forcing fields, $2\sum_{k,j}\overline{x}_i\overline{x}_j$ can be nonzero, because successive atomic jumps are not independent of each other. For the vacancy mechanism, for example, the vacancy concentration is so low (10^{-4} at the melting point) that two consecutive jumps are likely due to the same vacancy and it is obvious that after one jump an atom has a greater probability of making a reverse jump than to move randomly: jumps are therefore correlated. This correlation between the directions of two successive jumps initiated by the same vacancy reduces the efficiency of the effective walk with respect to a true random walk. Correlation occurs for all defect-assisted diffusion mechanism, it is related to the low concentration of point defects and decreases when this concentration increases.

We can compute $\overline{X^2}$ by assuming $\overline{X} = 0$ in the limit $\tau \to 0$. Neglecting correlation effects, we have

$$\overline{X^2} = \tau \sum_{k=1}^{z} \Gamma_k x_k^2 \tag{4.21}$$

where z is the number of jumps directions, Γ_k the mean atomic jump frequency for the kth direction and x_k the displacement along x for a k-jump. Hence, for an uncorrelated walk,

$$D_{rand} = \frac{1}{2} \sum_{k=1}^{z} \Gamma_k x_k^2 \tag{4.22}$$

For cubic lattices of celle size a, all frequencies Γ_k are equal, and

$$D_{rand} = \frac{\Gamma l^2}{6} \tag{4.23}$$

where $\Gamma = \sum_k \Gamma_k$ is the total jump frequency and l is the jump distance ($l = 1/2\sqrt{3}a$ for a bcc crystal, $1/2\sqrt{2}a$ for a bcc). For a bcc crystal, having 8 nearest neighbor at distance $a/2$, Eq. (4.22) gives

$$D_{rand} = \Gamma a^2. \tag{4.24}$$

Taking into account correlation effects for successive dependent jumps, we define a correlation factor, called the Haven coefficient, as

$$f = 1 + \frac{2\sum_{i,j}\overline{x_i x_j}}{\sum_{i=1}^{n}\overline{x^2}_i} \tag{4.25}$$

such that we write the real diffusion coefficient in Eq. (4.17) as

$$D = f D_{rand}. \tag{4.26}$$

For vacancy migration in a crystal with cubic symmetry we have

$$\overline{x_i x_j} = \overline{x_i^2 cos\theta_i j}. \tag{4.27}$$

With a few algebraic passages it is possible to show by recurrence that, if the jump obeys a two or three fold symmetry [110], the averages of cosines are

$$\overline{cos\theta_{ij}} = (\overline{cos\theta})^{j-i} \tag{4.28}$$

where θ is the angle between two subsequents jumps. Thus we have for the Haven coefficient

$$f = \frac{1 + \overline{cos\theta}}{1 - \overline{cos\theta}}. \tag{4.29}$$

An useful estimation of f yields

$$f = 1 - \frac{2}{z} \tag{4.30}$$

where z is again the coordination number of the lattice. Eq. (4.30) arises from the fact that because at each jump, the vacancy has the probability $1/z$ to performa a backward jump.

For self-diffusion, f is independent of temperature in isotropic materials, and has values $f = 0.727$ for vacancies bcc crystals, 0.78 for fcc and hcp, and 0.475 for divacancies in fcc and hcp.

4.3.3 Jump frequency

We pass now to the computation of the macroscopic diffusion coefficient for vacancy migration, i.e. the self diffusion coefficient for the atoms of the crystal.

The macroscopic diffusion coefficient is given as a function of the jumping rate of the diffusion species. The jump is seen, as in the context of statistical mechanical theory of fluctuations, as a passage of the system from one stable position to another, over an energetic barrier. The nature of this saddle is defined by the kind of lattice and the mechanism at work.

As recalled in Ref. [110], the probability of finding a vacancy in a neighboring atom is a static property, defined above with the computation of the formation free energy, and is therefore rigorously determined by the precedent statistical mechanics approach resorting to the definition of the formation energy. By contrast, the jump has a dynamic character: the jump proceed as an hamiltonian trajectory in phase space and the successive positions are strongly correlated. The approximations that are done in the reaction rate theory (see Appendix F) neglect these dynamical correlations, so that the different positions of the jump are viewed as independent static positions with an occupancy given by the equilibrium statistical weight all along the jump path, including the saddle position. The real diffusion coefficient can however be recovered, via the correlation factor f in Eq. (4.26) from the random walk diffusion coefficient. In this approach, the dynamical correlations between successive positions are lost, and therefore jumping particle has "no memory". Moreover, the approximation of a planar saddle hypersurface separating the initial and final states,

and passing through the saddle point, as usually taken in the harmonic approximation approach is not always valid.

The expression for the migration rate was obtained by Vineyard [107, 110]. As summarized in [51], Vineyard assumes in his work that the jump rate between two nearest defect positions A and B (corresponding to reactant and product states mentioned in Chapter 3) in a solid of N atoms at a given temperature T and pression p_{ext} is such that once the particle has passed the saddle point S, remains stacked in configuration B. This is indeed an assumption that neglects the aforementioned recrossing events; therefore, Vineyard theory corresponds to the transition state theory approach described in Appendix F.

The defect particle is described by a classical Hamiltonian, function of the $6N$ positions and momenta of the system. The transition state theory for reaction constants in many body systems (Appendix F) directly applies in the context of point defects migration in crystals, hence the absolute Vineyard transition rate is identical to transition state theory or Eyring expression, and reads

$$\Gamma = \frac{\prod_i^{3N} \omega_i^A}{\prod_i^{3N-1} \omega_i^s} \exp\{-\Delta H/k_B T\} \tag{4.31}$$

with the enthalpy difference $\Delta H = E_s - E_A + p_{ext}(V_s - V_A)$. In this expression, the ω_i^A are the frequencies of the normal modes for the vibrations of site A with potential energy V_A, while the ω_i^s are the normal mode frequencies for the vibrations orthogonal to path X at the saddle point S with potential energy E_s. The corresponding volumes of the solids are V_A where defects is in A, and V_s when the defects is in S. It is customary to assume that the total volume of the solid remains invariant before and after the jump, neglecting distortions given by the atom at the saddle point.

The neglected dynamic correlation aspects traduce in two effects: first, the presence of multiple jumps as a new diffusion mechanism (investigated for example in [108]), and secondly the existence of unsuccessful jumps, in which the jumping particle turns back once it reaches the saddle point (recrossing events). This second point recalls the necessity of considering the transmission factor mentioned in Chapter 3 and in Appendix F, needed in order to take account of the presence of failures in the jump attempts.

The main origin of these inefficiencies has been shown to lie in the anharmonicity of actual interatomic interactions, allowing for a curved rather then a planar hypersurface, as a curved hypersurface can be crossed twice [109]. Taking into account third order terms in the expansion of the potential (i.e. the first non harmonic term) about 10% of recrossing events can be avoided.

Always in the harmonic approximation, as in Eq. (4.6) we introduce an entropy difference between state A and the saddle S as the sum of logarithms of the number of available

vibrational modes in a range k_BT

$$\Delta S = k_B \left\{ \sum_{\alpha}^{3N} \ln\left(\frac{h\omega_\alpha^0}{k_BT}\right) - \sum_{\alpha}^{3N} \ln\left(\frac{h\omega_\alpha^s}{k_BT}\right) \right\}. \tag{4.32}$$

Recalling that the statistical weight corresponding to the saddle position is

$$P_s = P_0 \exp(-G_s/k_BT) \tag{4.33}$$

we show in Appendix F that the migration frequency in Eq. (4.31) derived from the flux over population method can be written as [110]

$$\Gamma = \frac{k_BT}{h} \exp\left(-(G_s - G_v)/k_BT\right) \tag{4.34}$$

where G_v is the free enthalpy of the vacancy at the initial equilibrium position, G_s is the free enthalpy of the vacancy *at the saddle point*, and using the harmonic approximation in both free enthalpies their difference is written

$$G_s - G_v = E_s - E_v + k_BT \sum_{\alpha=1}^{3N-1} \log\left(\frac{\hbar\omega_\alpha^s}{k_BT}\right) - k_BT \sum_{\alpha=1}^{3N} \log\left(\frac{\hbar\omega_\alpha^0}{k_BT}\right) + p_{ext}(V_s - V_0). \tag{4.35}$$

As mentioned also in Appendix F, notice that in Eq. (4.35) the eigenfrequencies ω corresponding to motions restricted to the saddle point do not correspond one to one to the frequencies in the stable position, and saddle vibrational modes are one less than stable state vibrational modes: indeed, we require here to restrict the motion to a hypersurface, of dimension $3N-1$, passing through the saddle point.

A more homogeneus formula is obtained writing the free enthalpy difference as

$$G_s - G_v = E_s - E_0 + k_BT \log\left(\nu_0 \frac{\prod_{\alpha=1}^{3N-1} \omega_\alpha^s}{\prod_{\alpha=1}^{3N} \omega_\alpha^0}\right) + p_{ext}(V_s - V_0) \tag{4.36}$$

and the jump frequencies reads

$$\Gamma = \nu_0 \exp\left\{-\frac{G_s - G_v}{k_BT}\right\}. \tag{4.37}$$

We introduced in Eq. (4.37) the so called 'attempt frequency' ν_0. This prefactor ν_0 compensates the difference of vibrational frequencies between saddle and stable point, and has no physical meaning on its own. It can be interpreted as the frequency at which the moving atom attempts to jump in the vacancy position, and assumed to be equal to the Debye frequency ν_D. In the case of Fe, having a Debye temperature $T_D = 470K$, $\nu_D = 10^{13}s^{-1}$. However, as can be seen from Eqs. (4.34) and (4.37), the assumption $\nu_0 = \nu_D$ can fail both for temperature effects (the Debye frequency ν_D is obviously different from prefactor k_BT/h for temperatures different then the Debye temperature) or for anharmonicities of

the vibrational entropy that are of course not taken into account in the quasi harmonic approximation.

Very often, in condensed matter problems the only term in Eq. (4.35) known without introducing any approximation is the height of the potential energy barrier $E_s - E_0$. Neglecting volume changes for the system with the atom in the equilibrium position and at the saddle, Eq. (4.37) is therefore rewritten in a Arrhenius way as

$$\Gamma = \Gamma_0 \exp(-\beta E_{barr}) \tag{4.38}$$

where $E_{barr} = E_s - E_0$ and the prefactor Γ_0 contains 'unknown' term, i.e. the attempt frequency and the entropic contribution of Eq. (4.32) related to the free enthalpy G, the *migration entropy* ΔS_m:

$$\Gamma_0 = \nu_0 \exp(\Delta S_m / k_B). \tag{4.39}$$

This formula is by far the most used in physical metallurgy. From Eq. (4.39) and (4.36), we see that in the harmonic approximation the migration entropy has a close expression to the vibrational entropy, both being given by vibrational modes.

4.3.4 Diffusion coefficient

The macroscopic diffusion coefficient of Eq. (4.26) can be written using Eq. (4.24) by considering also the contribution given by the point defect formation probability, c_v, with those connected to the jump frequency, taking into account also correlations between successive jumps. We have

$$D = f D_{rand} c_v = f a^2 c_v \Gamma \tag{4.40}$$

and inserting Eq. (4.37) for the jump frequency, we arrive to the expression

$$D = D_0^T \exp\left\{-\frac{\Delta H_f - \Delta H_m}{k_B T}\right\} \tag{4.41}$$

with

$$D_0^T = \nu_0 a^2 f \exp\left\{\frac{\Delta S_f + \Delta S_m}{k_B}\right\} \tag{4.42}$$

where the migration and formation entropies and enthalpies appear. Note that in constant volume system enthalpy differences reduce to potential energy barriers.

4.4 Migration rate estimates with LyTPS

In order to have reaction rate constants to use in KMC code, we apply LyTPS to the case of vacancy and divacancy migration in α-Iron. We then compare the results obtained with the values expected from the Vinayard transition state theory.

4.4.1 Vacancy migration in α-Iron crystal with LyTPS

The first example of a thermally activated process studied using the Lyapunov biased TPS method is the migration of a single vacancy in α-Iron crystal. Atomic interactions of the model system are described by an embedded atom model (EAM) potential (see Appendix G). Simulations are done for two different EAM potentials , A04 [90] and M07 [96]. The crystal structure is body-centered cubic, and the initial unrelaxed cell contains 1023 atoms displayed on 1024 lattice sites, the vacant site corresponding to the vacancy. The reaction coordinate used to represent the motion of the vacancy is the distance crossed by the moving atom that replaces the vacancy.

The free energy landscape for this system for the potential A04 has been investigated in [89]. It presents two stable states, the first corresponding to the initial configuration, and the second one to the initial configuration modified by an atom displaced of a first neighbour distance $a = 2.47$Å, switching its initial position with the vacancy site.

The potential energy barrier between these two states has been computed by several ab-initio methods (see [96] for a detailed description) giving values in the range $0.65 \pm 0.02 eV$. The EAM potential A04 used in these simulation estimates at 0K this barrier at 0.64 eV, while potential M07 estimates it at 0.67 eV [96]. Note that some experimental results [103] were interpreted in a way to give a potential energy barrier of $0.55 eV$ [96]; this value however was obtained by fitting experimental data with an Arrhenius plot and considering a prefactor Γ_0 in Eq. (4.39) as given only by the Debye frequency (see discussion below). For potential A04, there is a single free energy barrier separating these two states for temperatures above $T = 450K$, while for lower temperatures an intermediate metastable state appears, corresponding to an intra-site position for the moving atom.

We performed Lyapunov biased TPS simulations with trajectories of different lengths (see below), with time step $\delta t = 4 \cdot 10^{-15} s$. A preliminary MD simulation is done to equilibrate the system to the required temperature, with a friction parameter $\gamma = 2.5 \cdot 10^{12} s^{-1}$. We explored temperatures ranging from $300K$ to $850K$. The TPS shooting and shifting moves are iterated along a Markov chain of 1500 steps. Parameters for the diagonalization of the hessian matrix via the Lanczos algorithm (see Appendix D) were taken as $l = 4$ and $\delta_L = 10^{-13}$Å. Finally, we precise that in this case of vacancy migration we used a Lyapunov indicator L_{vac} given by the first order approximation of $L(\mathbf{z})$ in Eq. (3.35), i.e.

$$L_{vac}(\mathbf{z}) = \frac{1}{\mathcal{N}} \sum_{n=1}^{\mathcal{N}} dt \sqrt{\max(0, -\lambda_n^{min})} \tag{4.43}$$

in order to avoid numerical precision problems given by the smallness of the time step dt.

As for LJ_{38}, the trajectory length and the values for the control parameter α have been chosen in order to ensure an acceptance ratio of 25% and an adequate ergodic sampling of the phase space. For temperatures above $450K$, the presence of a single "smooth"

barrier for A04 separating the two metastable states makes this application simple enough: sampling of reactive trajectories is achieved using 15 α values from the unbiased simulation at $\alpha = 0$ up to $\alpha = 150 \cdot 10^{12}$, with trajectories of 300 steps. For temperatures below $450K$, an ergodic sampling of trajectory space appears more difficult, also due to the double bump. We therefore employed longer trajectories of 500 time steps, as well as larger values of the control parameter, up to $\alpha = 500 \cdot 10^{12}$ to allow the system to escape the initial basin.

Reaction constants for the passage between the two stable states above $450K$ are estimated from correlation functions unbiased with the MBAR algorithm, via Eq. (3.77).

For $T < 450K$, the presence of an intermediate metastable basin has to be taken into account in the evaluation of reaction constants. As recalled in Sec. 3.5.1, the reaction rate expression obtained from Eq. (3.77) holds only for adjacent reactant and products basins. At low temperatures, it is therefore more appropriate to use our algorithm to evaluate the reaction constant for the passage from the initial state to the intermediate basin. To recover afterwards reaction rates for the passage from one stable configuration to the other, we observe that reaction constants for transitions from the intermediate metastable state to either of the two stable states are equal, because of the symmetric shape of the potential surface. [96] Hence, from Eq. (3.93), reaction rate for the passage from one stable configuration to the other is simply one half of the reaction constant from one stable configuration to the intermediate one.

In Fig. 4.1 we compare the reaction rates obtained with Lyapunov biased TPS, those computed inserting in the transition state theory (TST) expression (Eq. (3.78)) the free energy barriers reported in Ref. [89], and reaction constants obtained with a classical Harmonic Approximation (HA). Above the Debye temperature ($470K$), rates obtained with Lyapunov biased TPS fall between TST and harmonic approximation values. To explain this point, we recall that reaction rates we estimate with the method exposed in Sec. 3.4 are derived from Eq. (3.77), hence correspond to the *phenomenological* rate constants. These values are therefore bounded from above by TST values, that overestimate reaction rates [75], as can be seen from Eq. (3.79). Conversely, values obtained with the harmonic approximation neglect anharmonicity effects on the activation barrier, thus giving reaction rates that are lower then the phenomenological rate constants we compute. Our results are then in agreement with the theoretical predictions of the reaction rate theory recalled in Appendix F.

These data can be used as well for the evaluation of the migration entropy mentioned in Eq. (4.39). A fit for the phenomenological rates in Fig. 4.1 with Eq. (4.38), using the ab-initio value for the migration potential energy barrier is presented in Figure 4.2: it gives a prefactor $\Gamma_0 = 12 \cdot 10^{13}$. Assuming an attempt frequency of $\nu_0 = 10^{13}$, this amounts of having a migration entropy for the monovacancy about $3k_B$.

This value can be compared to data available in literature: summed to the formation

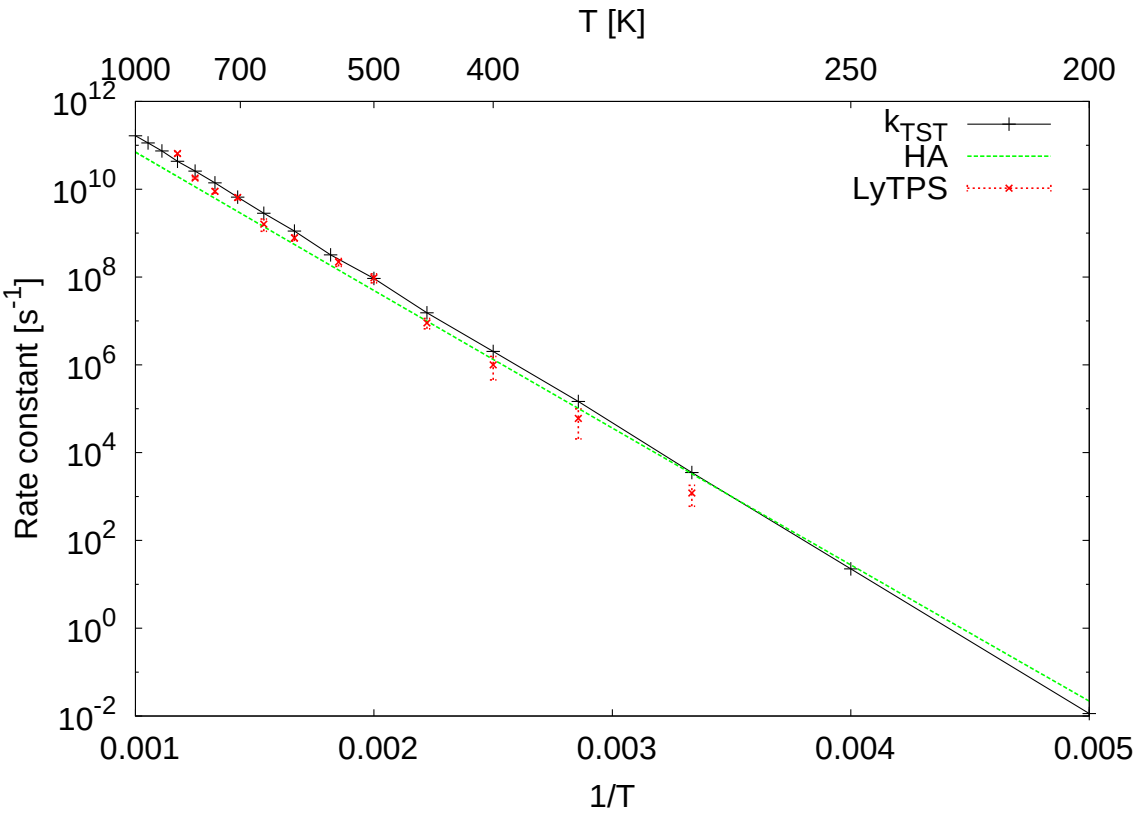

Figure 4.1: Arrhenius plot of reaction constants for migration of monovacancy in α-Iron with EAM potential A04 obtained with LyTPS (red points), compared with rates obtained using in Eq. (3.78) the free energy barriers proposed in Ref. [89] (black line) and using an harmonic approximation (green line).

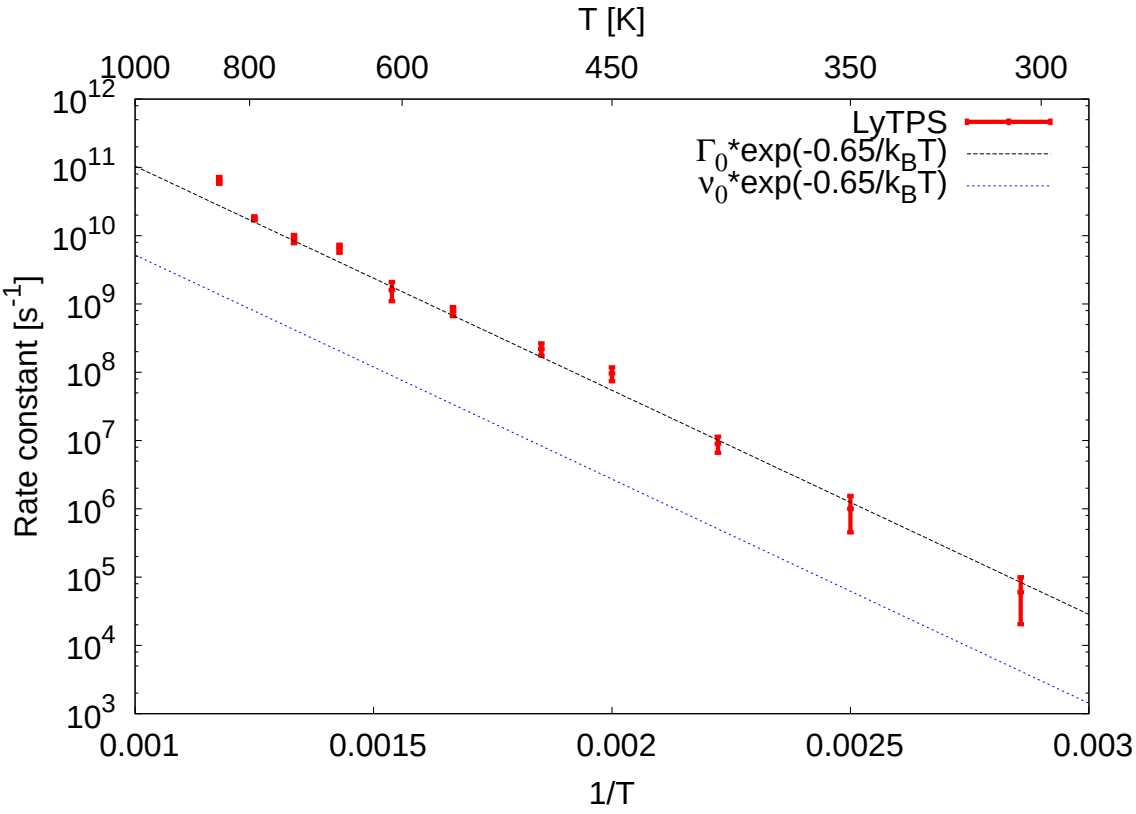

Figure 4.2: Logaritmic plot of migration reaction constants for monovacancy in α-Iron obtained with LyTPS (red points) using EAM potential A04, and fitted with the Arrhenius Eq. (4.38) (black line), taking as potential energy barrier height the value given by the A04 potential. The blue line indicates the theoretical prediction for an Arrhenius plot, with the same slope but neglecting in the prefactor Γ_0 of Eq. (4.39) the migration entropy term: this clearly shows that assuming $\Gamma_0 = \nu_0$ severely underestimates migration rates values.

entropy of 4 k_B computed by Lucas et Schaublin [105] with DFT and already mentioned, this means a total entropy (formation and migration) of $7k_B$. Other calculations of the formation entropy for the A04 and M07 potentials in the harmonic approximation have given values between 3 and 4 k_B. The experimental data for self-diffusion in bcc Iron by Takaki [111] were fitted with Eq. (4.42) assuming a total enthalpy $\Delta H = 2.9$ eV, thus giving a prefactor $D_0^T = 6 \cdot 10^{-4} m^2 s^{-1}$ that indicates (always for an attempt frequency of $\nu_0 = 10^{13} s^{-1}$ an experimental estimate for the total entropy of $7k_B$, in perfect agreement with our results. Note that Seeger [106] proposes a total entropy from the data of Takaki of $5k_B$, but taking a value $\nu_0 = 10^{14} s^{-1}$.

We conclude this section on vacancy migration rates noting that using potential M07 instead of A04 introduce no significative difference in the estimation of reaction constants:

this is shown in Fig. 4.3, where rates for the two potentials are compared, and fitted as in Fig. 4.2.

Potentials A04 and M07 differs mainly on the shape of the potential energy barrier separating the two stable configurations: potential A04 presents the metastable state mentioned above between the two stable states, while M07 has a 'flat' barrier. This different shape of the barriers could have implications in terms of a different migration entropy in the harmonic approximation (due to different values for the vibration eigenfrequencies at the saddle point, see Eq. (4.32)). However, this apparently do not affect significatively the value of migration rates.

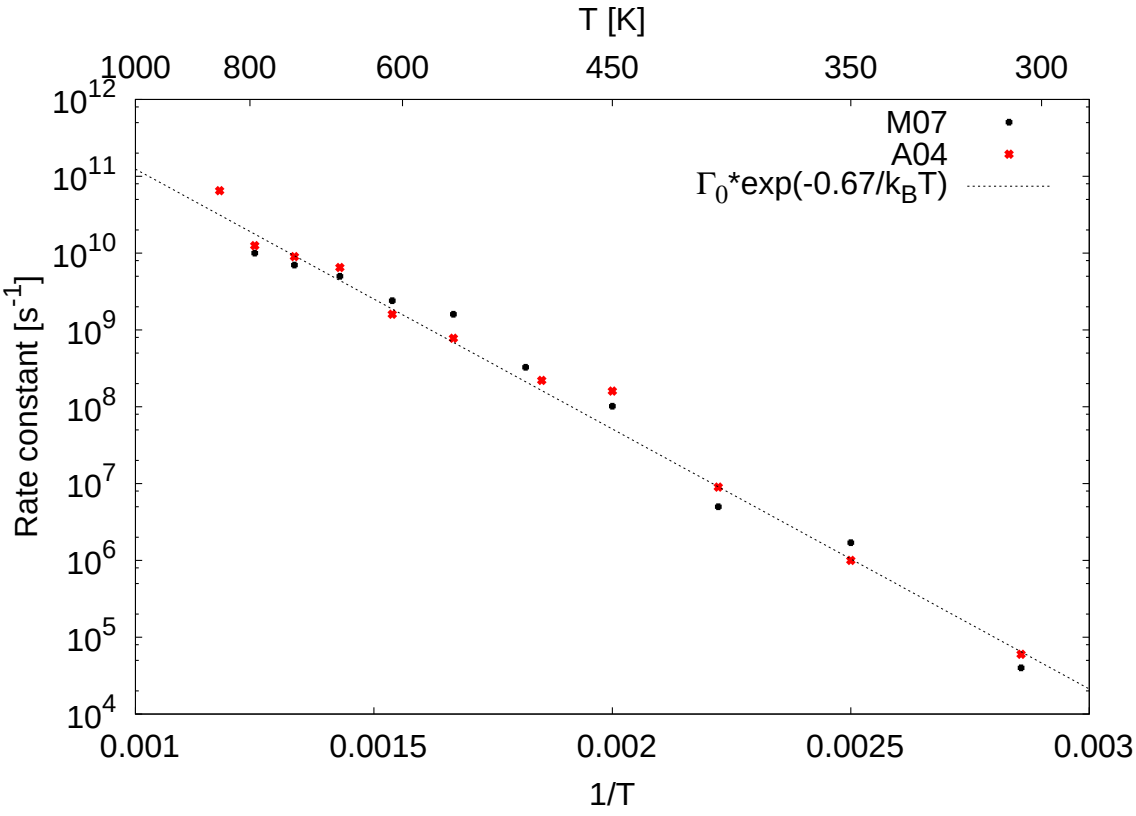

Figure 4.3: Arrhenius plot for reaction constants for migration of monovacancy in α-Iron obtained with LyTPS with potentials A04 (red points) and M07 (black points). The slope is given by the height of the potential energy barrier of M07.

4.4.2 Divacancy migration in α-Iron crystal

The second example of activate processes in nuclear materials we study is the divacancy migration from a first to second neighbour position (see Fig. 4.5). Simulations are done using the EAM potential (see AppendixG), A04 [90]. This potential predicts a 'simple'

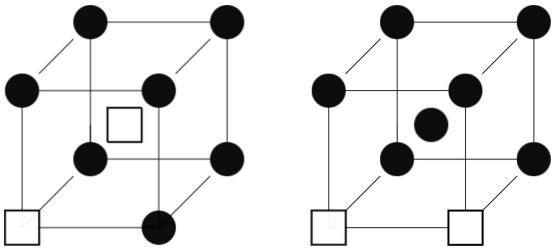

Figure 4.4: **Left**: Divacancy in first-neighbor position **Right**: Divacancy in second-neighbor position

barrier separating the two configuration, hence the study of this structural transition gives again further information on an eventual dependence of LyTPS numerical results on the shape of the potential energy barrier [96]. The crystal structure is body-centered cubic, and the initial unrelaxed cell contains 1022 atoms displayed on 1024 lattice sites, the vacant sites corresponding to the divacancy. The reaction coordinate is given by the distance between the two vacancies, computed again from the distance crossed by the moving atom replacing one of the two vacancies. The initial configuration is given by the two vacancies positioned at a first neighbor distance $a = 2.47$Å, corresponding to a metastable state, while the final state is the same configuration with the vacancies positioned at a second neighbor distance of $a = 2.87$Å, corresponding to the stable state [101] (see Fig. 4.4). The beginning positions for the two vacancies are as first neighbour: this in an unstable configuration that is separated by a potential energy barrier of 0.62 eV from the second neighbor configuration, that has been proven to be the most stable one [102].

There is a single free energy barrier separating these two states, and we assume that a single vacancy jump happens during our simulations. We focused on this transition, although transitions from the first-neighbour to third neighbour position have been observed in our simulations, but very rarely, such that we did not get an sufficient statistics to recover results with MBAR.

As in the Sec. 4.4.1, we performed Lyapunov biased TPS simulations with trajectories of different lengths (see below), with time step $\delta t = 4{\cdot}10^{-15}s$. A preliminary MD simulation is done to equilibrate the system to the required temperature, with a friction parameter $\gamma = 2.5 \cdot 10^{12}s^{-1}$. We explored temperatures ranging from $300K$ to $850K$. The TPS shooting and shifting moves are iterated along a Markov chain of 1500 steps.

The choice of the numerical values for the bias parameter α is the same for the vacancy migration of the previous section; indeed, these values are chosen in function of the Lyapunov indicator L of Eq. (4.43) that depends on the conformation of the potential energy surface. As the EAM potentials used to study the vacancy and divacancy migration are very close, the use the same numerical values for α. For temperatures above $450K$, sam-

pling of reactive trajectories is achieved using 15 α values from the unbiased simulation at $\alpha = 0$ up to $\alpha = 150 \cdot 10^{12}$, with trajectories of 300 steps. For temperatures below $450K$, an ergodic sampling of trajectory space appears more difficult. We therefore employed longer trajectories of 600 time steps, as well as larger values of the control parameter, up to $\alpha = 500 \cdot 10^{12}$ to allow the system to escape the initial basin. We neglect the presence of intermediate metastable configurations between the first- and second-neighbor distance configuration. Reaction constants for the passage between the two stable states are estimated from correlation functions unbiased with the MBAR algorithm, via Eq. (3.77), as in previous applications.

We compare these data in Fig. 4.5 with a fit as in Eq. (4.38) with ν_0 the Debye frequency, given by $10^{13}s^{-1}$, and E_{barr} is the potential energy barrier from the first to the second neighbor configuration given by ab initio calculation, of 0.62 eV (this value is indeed the same given by the A04 potential). The migration entropy can be inferred to be about $5,7k_B$.

As it is possible to see, rates computed with LyTPS are much larger than those computed if taking the approximation $\Gamma_0 = \nu_0$, thus suggesting that using these data for simulating resistivity recovery simulations, described in the next section, will yield results in a better agreement with experimental data. Once again, we stress that these results are more realistic thanks to the fact that we are directly computing *phenomenological* finite temperature rate constants.

4.5 Resistivity recovery experiments

Important informations on the post-irradiation properties of vacancies and vacancy-type defects can be obtained by resistivity recovery experiments, where an irradiated sample recovers its defect-free resistivity as it is annealed at increasing temperatures.

The experimental protocol is the following: metals are first irradiated at very low temperatures (around 4K) with high-energy electrons. Subsequently, the irradiated sample is progressively heated: indeed, when the temperature is raised at a constant rate ("isochronal annealing"), various migration mechanisms are enabled, thanks to the thermal energy that becomes comparable with the height of activation barriers. In this way, observing temperatures at which resistivity changes (or, equivalently, the variation of the population of defects, given by emission peaks) happen, activation barriers can be estimated. The height of this emissions peaks is related to the resistivity per defect, an aspect in which we are not interested in this work.

In the work of Fu et al. [101], abrupt resistivity changes - so-called recovery stages - has been reproduced in numerical simulations observed upon annealing at increasing temperatures after electron irradiation in α-Fe by combining *ab initio* and event-based

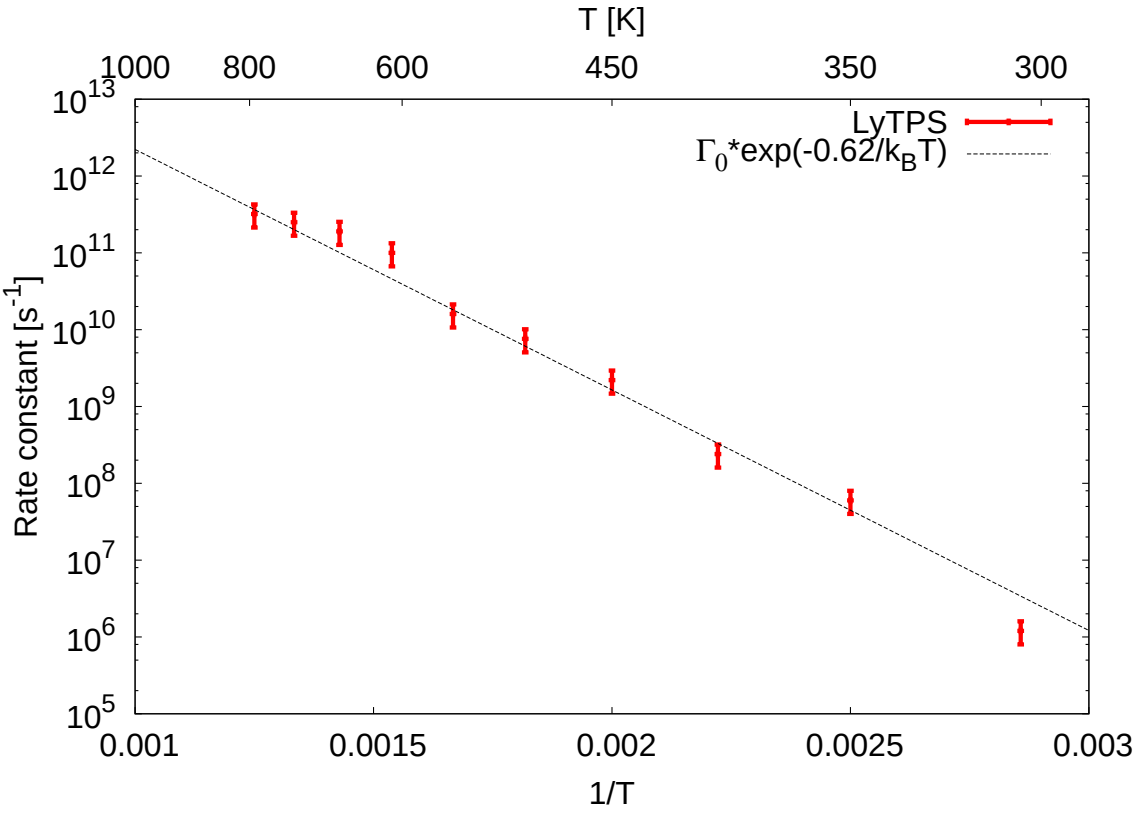

Figure 4.5: Arrhenius plot of reaction constants for migration of divacancy in bcc iron obtained with Lyapunov biased TPS (red points), fitted with Eq. (4.38) taking a potential energy barrier $E_{barr} = 0.62eV$ [96].

kinetic Monte Carlo (KCM) methods.

Ab initio simulations are performed in order to to estimate potential energy migration barriers. Calculations are done in the framework of density functional theory for electronic structure computations, resorting to the SIESTA code. Once activation barriers are estimated, migration rates can be inferred using Eq. (4.38), and then used as input parameters for kinetic Monte Carlo simulations.

Event-based KMC is implemented in the JERK or FPKMC codes, in which defects are considered as objects characterized by their space coordinates, their nature (i.e. distinguishing between interstitials, vacancies, divacancies...), shape (spherical for simple point defects), mobility and dissociation rate. These last data are therefore provided resorting to the aforementioned *ab initio* simulations. When mobile, these objects may migrate and annihilate on their anti-defect (as in the case of recombination of Frenkel pairs) or aggregate to form clusters. KMC allows then to reproduce numerically resistivity recovery experiments.

Reference experiments were made in high-purity electron-irradiated Fe by Takaki *et al.* [111] with irradiation doses in the range $2 \cdot 10^{-6}$ to $200 \cdot 10^{-6}$ displacement per atom (dpa). The derivative of the resistivity recovery plots with respect to temperature shows peaks referred to as recovery stages. For some stages, the change-of-slope technique allows one then to deduce an effective activation energy related to the activation temperature.

We focus on the stage in (220-278 K) that, as reported in [101] is suggested to result from vacancy migration, with an ab-initio potential energy migration value of $E^v_{mig} = 0.67eV$. Also small vacancy clusters, like divacancies, are found to have the well known ground-state configurations [102]. They migrate by successive nearest-neighbor mono-vacancy jumps. This motion may require passing through metastable intermediate states corresponding to first or second neighbor distances, as mentioned in the previous section.

The derivative of the resistivity recovery and the evolution of the defect population with respect to temperature at low ($2 \cdot 10^{-6}$ dpa) and high ($200 \cdot 10^{-6}$ dpa) dose are analyzed. As in the experiment, four distinct stages are obtained, the first two connected to correlated or uncorrelated recombination of Frenkel pairs (interstitials and vacancies), the third given by interstitials migrations, and the last, indicated in the literature with (III), related to vacancy and vacancy clusters migration, which may aggregate with other vacancies or vacancy clusters, or annihilate on interstitials clusters. It is shown as well that divacancies and vacancy clusters contribute to the stages attributed to mono-vacancy migration: they not give rise to peaks disconnected from stage (III), in agreement with experiments, since their migration energies are lower or equal to E^v_{mig}, and they are precisely formed at stage (III) as a result of V migration.

For this stage, numerical results of Ref. [101] show the largest discrepancy with respect to experimental data, as with a peak of vacancy emission for low irradiation doses at 335 K,

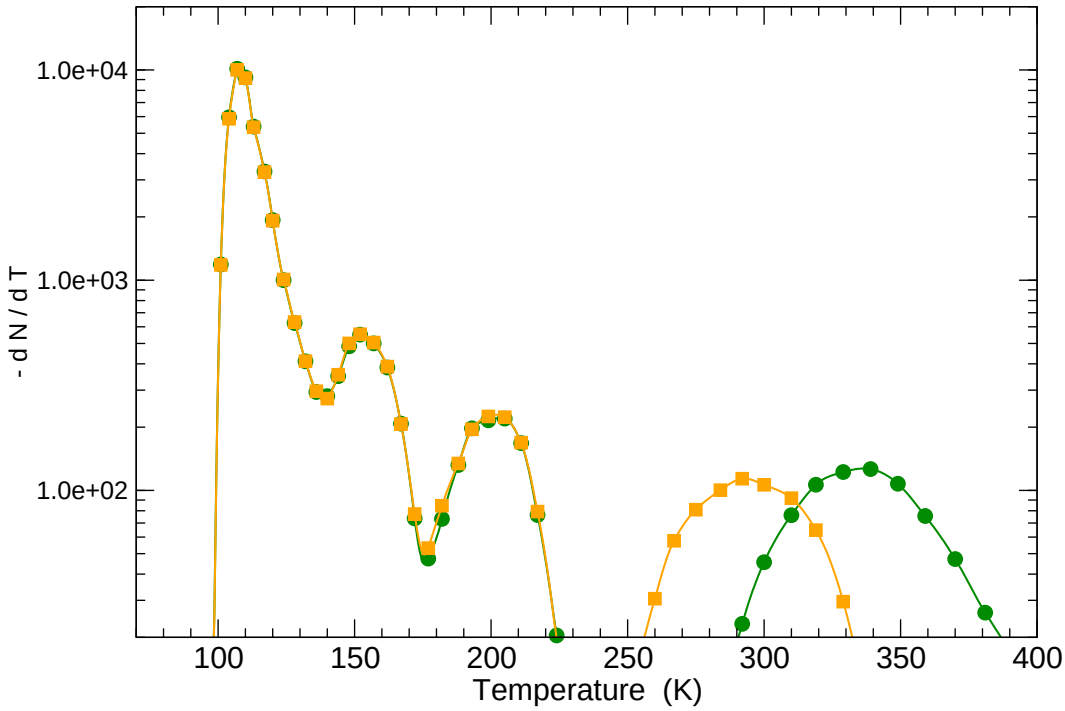

Figure 4.6: Time derivative of the vacancy population in α-Fe as a function of temperature at low irradiation doses ($2 \cdot 10^{-6}$ dpa). The experimental peak is observed at 278 K, and the peak given by using reaction rates of Fig. 4.2 in a FPKMC code is at 289 K (yellow line). The vacancy emission peak mentioned in [101] was at 334K (green line).

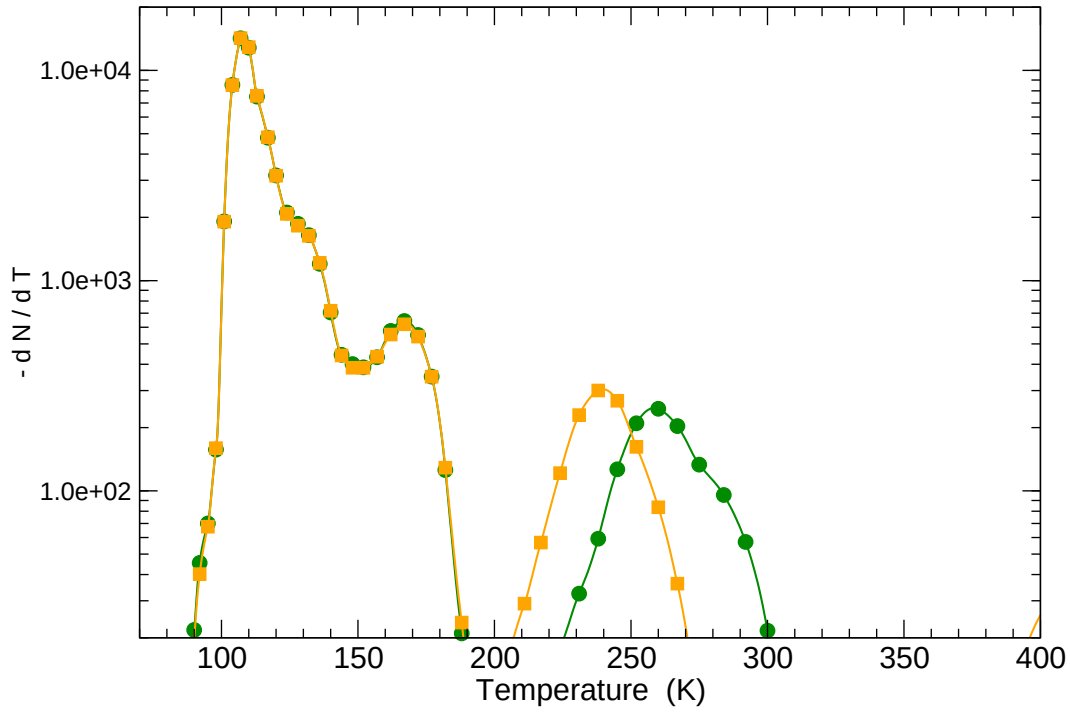

Figure 4.7: Same figure as Fig.4.6 for high irradiation doses ($200 \cdot 10^{-6}$ dpa). The experimental peak is observed at 220K, the peak given by migration rates of Fig. 4.2 at 236 K (yellow line) while the in [101] it was at 256K (green line).

57 K above the experimental position is found. Numerical results for high irradiation doses give a peak at 256 K, while the experimental measures denoted an 'activation temperature' of 220 K. These discrepancy were explained in [101] both by a shift of only 0.1 eV on the values of the migration energies of vacancy-type defects or by to two orders of magnitude in the pre-exponential factors.

Migration rates obtained with LyTPS and reported in Fig. 4.2 show indeed that the second hypothesis is the correct one. The difference with [101] is indeed the use in Eq. (4.38) an Arrhenius fit with a prefactor value Γ_0 given *only* by the Debye frequency ν_0, thus neglecting entropic contributions contained in Eq. (4.39). This was due to the fact that these computations with ab initio method did not estimate migration entropies. By contrast, we repeat that the LyTPS method presented in Chapter 3 gives direct access to phenomenological rate constants, thus allows to correctly compute the value of Γ_0 taking into account entropic effects.

Numerical simulations of [101] were therefore done again, using LyTPS migration rates as input values for a first passage kinetic Monte Carlo (FPKMC) code. Results are shown in Fig. 4.6 and 4.7, and are in a really good agreement with experimental results of Takaki [111].

4.6 Conclusion

In this chapter we have applied LyTPS to a condensed matter problem, the computation of migration rates for vacancy type defects in Iron. The determination of the exact values for physical terms giving these migration rates - namely, the energy (or enthalpy) barrier and the entropy contribution in the prefactor - is a debate still open in the physical metallurgy field, as numerical results have been often interpreted using different formulations of Eqs. (4.38) and (4.39), while experimental data give only access to quantities present in Eq. (4.41). Therefore, the estimation of formation and migration enthalpies and entropies is subjected to several variations in the literature, given by the difference in the choice of the energy (or enthalpy) barrier in the exponential term of the Arrhenius fit, as well as the choice of the prefactor. In particular, as mentioned above, the conventional choice for a prefactor $\Gamma_0 = \nu_0$ led to an attribution of values for the energy barrier that are lower than those predicted by *ab initio* or free energy calculations (see for instance the value of 0.55 eV [103], extrapolated from experiments, compared to 0.67 obtained by *ab initio*)

Migration rates directly computed via LyTPS give indeed a clue to determine the effective values for migration barriers in α-Iron, but do not give a definitive answer: further work is indeed required to correctly establish these results. In particular, it is still necessary to compute the vibrational entropy appearing in Eq. (4.39) with *ab initio* methods: this has not been done in the past, due to the huge computational effort this work requires. These

DFT calculations of the migration entropy will be executed in the harmonic approximation - as it is by now the best method still numerically affordable - and will just have the role of indicating if the reduction of the discrepancy between KMC and experimental resistivity recovery is effectively due to entropy effects or not.

Finally, we believe that LyTPS would be applicable also to compute migration rates of dislocation lines, as well as to study the migration of interstitials. The combination of phenomenological rates computed by LyTPS and event-based KMC would indeed be a powerful tool to predict the complete kinetics of irradiated materials.

Chapter 5

Conclusion and perspectives

This PhD thesis focused on the study of rare events, characterizing reactive paths and computing reaction constants for thermally activated structural transitions in many-body systems.

To this scope, two methods were elaborated; one of them has furthermore been applied to the study of point defect migration in nuclear materials. Methods have been successful in opening new perspectives in the field of importance sampling techniques, while the application yielded important results for nuclear materials science.

These achievements can be described in details as it follows. Concerning the *transition current sampling* method, presented in Chapter 2, we showed how to present this method - previously elaborated as Lyapunov-weighted dynamics - in a purely classical approach, and applied it to a benchmark system. This gave us a much better insight in transition current sampling and in Lyapunov-weighted dynamics as well (both familiarly called the "clones" method), as a simpler description of the underlying theory, coupled with an application to a complex system like LJ_{38}, made us accurately test its potentialities and its drawbacks. In particular, we stress that in its application to LJ_{38}, TCS enabled us not only to localize well-known states and barriers, but even to characterize transition regions that were usually very poorly sampled by other importance sampling methods. The full description of the reaction path for the icosahedral to octahedral structural transition at finite temperature has been obtained, stressing entropic effects beside those linked to the potential energy surface conformation. However, the main drawback resides in the fact that unbiasing this sampling scheme in order to recover reaction rates resulted to be quite difficult, so limiting TCS to being an energy landscape exploration method, more than an algorithm suitable to compute also reaction rates.

For these results, we strongly believe that TCS may be successfully employed in the study of the structural transitions of even larger systems, like proteins - as done in the past by Mossa and Clementi, or in general to systems with a very complex free energy surface, also if not explored yet (i.e. where reaction paths have not been previously identified) as TCS is able to find transition regions without requiring any kind of reaction coordinate. Moreover, we believe that its application to the study of nonequilibrium systems - via an attentive reformulation of some points of its theoretical basis - could give really interesting results. Finally, as a perspective, we point out that an application of the Diffusion Monte

Carlo algorithm exploited in the sampling of transition currents has been interestingly done by J. Kurchan and myself in order to study large deviations connected to the glassy transition in monodisperse Lennad-Jones systems.

The second method we developed, the *Lyapunov biased transition path sampling* (LyTPS) consists in an important development of the transition path sampling technique: indeed, the introduction of a bias based on local Lyapunov numbers enhances significantly the fraction of reactive trajectories observed during simulations. We stress in fact that the transition path sampling in canonical ensemble had been tested before on LJ_{38}, leading to results only resorting to a huge employ of CPU time. By contrast, a TPS in our biased ensemble gave reactive trajectories linking the basins corresponding to the two main crystalline structures. This achievement acquires more importance once we consider that, although this result of sampling reactive paths was obtained as well with TCS, we are able with LyTPS - thanks to the Bennett-Chandler formalism - to compute reaction rate constants. These reaction rates have furthermore the advantageous feature of being phenomenological, i.e. they contains informations about finite temperature and anharmonicity of the activation barrier. Note, however, that in order to compute reaction rates in LyTPS, reaction constant values discriminating the location of states and saddle points in phase space are needed (see the indicator functions used in the transition state theory). Therefore, we suggest a coupled use of TCS - in order to preliminary locate barriers and assign for each barrier a given value to the reaction coordinate - and then of LyTPS, that computes reaction constant once basins are correctly delimited.

Perspectives for future applications of LyTPS are given by all systems where an accurate computation of reaction rates at finite temperature is needed, as in thermally activated processes occurring in physical metallurgy (see below). We recalled in Chapter 3 that LyTPS can be seen as a finite temperature version of ART techniques. As in this algorithm, the main problem we found was to start having reactive trajectories at very low temperatures for smooth potential energy surfaces: in this situation, sampled paths lie indeed at the bottom of the potential well, where hessian spectra are all positive, hence don't contribute to the Lyapunov bias and do not accelerate our sampling. Further work could be spent in the direction of slightly modifying the analytical expression of the Lyapunov indicator for the bias, in order to accelerate the activation of reactive trajectories, by enabling them to find the inflection point on the potential energy surface where the first negative hessian eigenvalues start to appear.

The third achievement of this PhD thesis has been given by the computation of *migration rates of vacancy-type defects in α-Iron* by using LyTPS. This computation has been done with the aim of reproducing numerically, via a KMC code, some resistivity recovery experiments, that were however not correctly simulated by previous works presented in the literature, because reaction rate values given as input parameters to KMC completely

neglected entropy contributions. By contrast, using LyTPS data we were able to estimate the migration entropy related to vacancy type defects, and subsequently we obtained resistivity recovery simulations in a very good agreement with experimental data. This results shows how powerful LyTPS method can be.

We conclude by observing that LyTPS has then a wide range of applications, from the migration of vacancy and interstitials clusters to the motion of dislocation lines, whose evolution is really significant for the study of the structural behavior of nuclear materials. The computation of finite temperature entropic effects on the atomic scale results than to be essential for the understanding of phenomena at much larger scales.

Appendix A

Hamiltonian dynamics

In this Appendix we present some considerations on Hamiltonian dynamics and numerical schemes aimed at simulating it. A concise description can be found for example in the handout of W. Cai [92], that we follow here.

Hamilton equations read (as in Eq. (3.15))

$$\begin{aligned} \dot{\mathbf{q}} &= \frac{\partial H(\mathbf{q},\mathbf{p})}{\partial \mathbf{p}} \\ \dot{\mathbf{p}} &= -\frac{\partial H(\mathbf{q},\mathbf{p})}{\partial \mathbf{q}} \end{aligned} \tag{A.1}$$

For N particle systems, $\mathbf{q}$ is a $3N$-dimensional vector specifying its position and $\mathbf{p}$ is a 3N-dimensional vector specifying its momentum. In terms of $\mathbf{q}$ and $\mathbf{p}$, the equations of motions Eq. A.1 is a set of (coupled) first-order differential equations. The equation can be reduced to an even simpler form if we define a 6N-dimensional vector

$$\eta = (\mathbf{q}, \mathbf{p}) \tag{A.2}$$

and the equation of motion becomes

$$\dot{\eta} = \omega \frac{\partial H(\eta)}{\partial \eta} \tag{A.3}$$

where

$$\omega = \begin{pmatrix} \mathbf{0} & \mathbf{I} \\ -\mathbf{I} & \mathbf{0} \end{pmatrix} \tag{A.4}$$

and $\mathbf{I}$ is the $3N \times 3N$ identity matrix. The $6N$-dimensional space which η belongs to is the phase space. The evolution of system in time can be regarded as the motion of a point η in the $6N$-dimensional phase space following the first-order differential equation.

As the total energy is conserved by Newton's equations of motion, the motion of a point in phase space must be confined to a subspace (or hyperplane) with constant energy. Considering the evolution of a small phase-space element over time, is it possible to show that the area enclosed by this element remains constant, even though the element inevitably undergoes translation and distortion. Let the element at time t be a hypersphere around point η whose area is

$$|d\eta| = |d\mathbf{q}| \cdot |d\mathbf{p}| \tag{A.5}$$

Let ξ ben the position at time $t+\delta t$ of η. We can linearize, for $\delta t \to 0$ its evolution at first order as

$$\xi = \eta + \dot{\eta}\delta t = \eta + \omega \frac{\partial H(\eta)}{\partial \eta}\delta t \tag{A.6}$$

Let $D\mathbf{M}$ be the Jacobian matrix of the transformation from η to ξ, i.e.

$$D\mathbf{M} = 1 + \omega \frac{\partial^2 H(\eta)}{\partial \eta \partial \eta}\delta t \tag{A.7}$$

The area of the element at time $t+\delta t$ is related to the determinant of the Jacobian matrix as

$$|d\xi| = |d\eta| \cdot |detD\mathbf{M}| = |d\eta| \cdot (1 + \mathcal{O}(\delta t^2)) \tag{A.8}$$

As explained in Ref. [92], because the first order term of δt in $detD\mathbf{M}$ vanishes, we can show that the area of the element remains constant for an arbitrary period Δt (see Liouville theorem): if we only divide this time interval into M subintervals, each with $\delta t = \Delta t/M$. The area change per subinterval is of the order of $1/M^2$. The accumulated area change over time period Δt is then of the order of $1/M$, which vanishes as $M \to \infty$. Because the area of any element in phase space always remains constant, the evolution of phase space points is analogous to that in an incompressible fluid.

The Hamiltonian dynamics has even more symmetries. The transpose of $D\mathbf{M}$ is

$$D\mathbf{M}^T = 1 - \omega \frac{\partial^2 H(\eta)}{\partial \eta \partial \eta}\delta t \tag{A.9}$$

and we have

$$D\mathbf{M}\omega D\mathbf{M}^T = \left(1 + \omega \frac{\partial^2 H(\eta)}{\partial \eta \partial \eta}\delta t\right) \omega \left(1 - \omega \frac{\partial^2 H(\eta)}{\partial \eta \partial \eta}\delta t\right) = \tag{A.10}$$

$$= \omega + \mathcal{O}(\delta t^2) \tag{A.11}$$

This is the so called *symplectic* condition, valid up to second order. Again, the symplectic condition is satisfied for an arbitrary period of time. This condition implies as well area conservation, since as $D\mathbf{M}\omega D\mathbf{M}^T = \omega$, $det\omega = det(D\mathbf{M}\omega D\mathbf{M}^T) = det(D\mathbf{M})^2 det(\omega)$ hence $detD\mathbf{M} = \pm 1$.

Newton's equation of motion are simulated by numerical integrators for ordinary differential equations. However, Newton's equation of motion derived from a Hamiltonian are such that given physical quantities, like energy, are conserved: therefore, ODE solver for Molecular Dynamics simulations have to obeys the same conservation laws of a Hamiltonian system. Ideally the numerical integration scheme should be able to satisfy all the symmetries of the true dynamics of the system.

Hamiltonian dynamics is also time reversible: if η evolves to ξ after time t, another phase space point η' with the same $\mathbf{q}$ as ξ but with reversed momentum $\mathbf{p}$ will exactly come

to point η after time t. To summarize, the dynamics of a hamiltonian system conserves total energy, conserves phase space area (incompressible flow in phase space), satisfies symplectic condition and is time reversible.

Ideally, the numerical integrator we choose to simulate Hamiltonian system should satisfy all of these symmetries. For instance, the Verlet integrators (see Eq. (3.20)) are symplectic, and guarantee area conservation and time reversibility.

Since by hypothesis the integration steps using the Verlet algorithm are time reversible, then in principle an entire trajectory of Molecular Dynamics simulation using the Verlet algorithm should be time reversible. In practice, however, one never gets perfect reversibility, because of the combined effect of numerical round off error and the chaotic nature of trajectories of many Hamiltonian systems.

The chaotic nature of many Hamiltonian system has been illustrated in Chapter 3, by considering the evolution of two trajectories starting with very close initial conditions: at large time t, they diverge exponentially at a rate given by the maximum Lyapunov exponent, with a behavior called Lyapunov instability. Since real numbers can be represented in computer simulations only with finite precision, a small (random) perturbation is indeed introduced at every step of the integration. Therefore, as stated in [92], the numerical trajectory deviates at one point from the analytical trajectory significantly. While the analytical trajectory is reversible, the one generated by a computer is not. This is why a maximum number of iterations N, beyond which the original state cannot be recovered by running the simulation backwards. This by itself is not an issue, since one rarely needs to recover the initial condition of the simulation in this way. However, this behavior does mean that we will not be able to follow the "true" trajectory of the original system forever on a computer. Sooner or later, the "true" trajectory and the simulated one will diverge significantly.

We conclude noticing that there is no contradiction between Lyapunov instability and area conservation of Hamiltonian systems. The area conservation property states that an element in the phase space will evolve while keeping its area constant. But the Lyapunov instability says that two points in this phase-space element, also if very close at the beginning of the dynamical evolution, will at one point be separated into great distances. This implies that while the phase-space element maintains its total area, its shape is continuously distorted, stretched and folded, so that any two initially close points in this element will be separated by great distances [92, 68].

Appendix B

Quantum Mechanic analogies

The first theoretical study of the properties of probability currents, on which this work is based, was done resorting to a quantum mechanic formalism to describe probability currents, in order to couple those statistical mechanics concepts with the quantum formalism of SuperSymmetry. This was done by Tanase-Nicola and Kurchan [14] for the Fokker-Planck case, and then further developed by Tailleur *et al.* [13] for the Kramers equation, a statistical mechanical description of Lyapunov exponents [14], and finally applied to some interesting examples like the study of protein folding by Mossa and Clementi [28].

Although one of the main achievements of this PhD work consists in a purely classical derivation of the probability currents theory, we briefly sketch here the main points of the quantum description, in order to clarify the links between the theoretical derivation of the probability current and the computational method of Diffusion Monte Carlo that has been associated to it.

The scope of this section is giving only a short review, hence we restrict here to the Fokker-Planck case. The main advantage of Quantum Mechanic formalism is that it allows, with a very few concepts of quantum mechanics, to trace a clear descriptions of physical phenomena involving a separation of time scales.

B.1 Schrödinger equation and random walk

We first note that the idea of using the formal analogies between quantum mechanics and diffusion theory was attributed to Fermi and first presented by Andersen [50], that proposed a random walk simulation of the Schrödinger equation needed to quantum chemistry computations of electronic orbitals. This reads, for a single particle in one dimension, as

$$-i\hbar\frac{\partial\psi}{\partial t} = \frac{\hbar^2}{2m}\frac{\partial^2\psi}{\partial x^2} - V(x)\psi \tag{B.1}$$

A transformation to imaginary time (Wick rotation) $it/\hbar \to \tau$ transforms Eq. (B.1) in

$$\frac{\partial\psi}{\partial\tau} = \frac{\hbar^2}{2m}\frac{\partial^2\psi}{\partial x^2} - V(x)\psi. \tag{B.2}$$

that can be integrated in imaginary time to large values of τ yielding the spatial part of the wavefunction ψ. Eq. (B.2) is formally identical to a diffusion-reaction equation for a

density $c(x)$ of the form

$$\frac{\partial c}{\partial t} = D_0 \frac{\partial^2 c}{\partial x^2} - D_1 c \tag{B.3}$$

with D_0 the diffusion coefficient and D_1 the reaction rate. Therefore, usual numerical methods aimed to simulate random walk, modeled with Eq. (B.3) can be used to compute quantum mechanics wave functions.

B.2 Quantum mechanic formulation of Fokker Planck equation

Going back to a statistical mechanics framework of stochastic systems, a probability density P can be written in a Dirac $\mathbf{x}$-space representation, as $P(\mathbf{x}) = \langle \mathbf{x}|\psi\rangle$. The Fokker-Plack equation (Eq. (2.11)) is then written as

$$\frac{d}{dt}|\psi\rangle = -H_{FP}|\psi\rangle \tag{B.4}$$

whose solution at finite time reads $|\psi(t)\rangle = e^{-tH_{FP}}|\psi_0\rangle$, where $|\psi_0\rangle$ is a given initial state. Hence, the probability of being in $\mathbf{x}$ at time t is just rewritten as

$$P(\mathbf{x},t) = \left\langle \mathbf{x} \left| e^{-tH_{FP}} \right| \psi_0 \right\rangle \tag{B.5}$$

As in quantum mechanics, the Fokker-Planck hamiltonian can be considered to have a spectrum of eigenvalues λ_a corresponding to given energy states, such that

$$H_{FP}|\psi_a\rangle = \lambda_a |\psi_a\rangle \tag{B.6}$$

Expressing the initial probability function as a linear combination of (right) eigenstates of the hamiltonian,

$$|\psi_0\rangle = \sum_a c_a |\psi_a\rangle\,, \tag{B.7}$$

the probability $P(\mathbf{x},t)$ can be rewritten as

$$P(\mathbf{x},t) = \langle \mathbf{x}|\psi(t)\rangle = \sum_a c_a \langle \mathbf{x}|\psi_a\rangle\, e^{-t\lambda_a} \tag{B.8}$$

The Perron-Frobenius theorem ensures [21] that the real part of these eigenvalues is always nonnegative, hence the system probability distribution is always converging, for long times, to a given steady state.

The formal description of the probability P with a set of eigenvalues furnishes an instructive description of the aforementioned *separation of time scales*. Indeed, in quantum mechanics, due to Heisenberg indetermination principle, energy eigenvalues correspond to

time constants related to the decay time from one state to another: it is possible to write $\lambda_a \sim \tau_a^{-1}$ where τ_a is the escape time from state a.

The spectrum of the Fokker-Planck hamiltonian is composed by different eigenvalues: the zero eigenvalues, corresponding to stable (i.e. ground energy) states, correspond to local minima where the time one has to wait in order to see the system escaping from this state is practically infinite. "Almost-zero" eigenvalues correspond to long (but finite) escape rate: they express the passage time from one metastable basin to another. On the other hand, high eigenvalues, corresponding to short times, represent the relaxation or equilibration time inside the corresponding stable states. It is therefore possible to group these eigenvalues in the following way: $\lambda_0 = 0$ is the ground state, related to the equilibrium Gibbs-Boltzmann distribution $P \sim e^{-\beta H}$; the eigenvalues $\lambda_1, \ldots, \lambda_p$ "almost zero" express the passage times τ_e between the p metastable states of the system. The higher eigenvalues $\lambda_a, a > p$, separated by the other eigenvalues by a 'gap', give the intra-basin relaxation times τ_{rxn}: the separation of time scales arise exactly from these distinctions, such that the rare events theory is valid for times $\tau_{rxn} \ll t < \tau_e$.

B.3 Instanton

We conclude this Appendix sketching here a way to compute the transition probability using the aforementioned quantum mechanics analogies. The transition probability for a quantum mechanical particle tunneling through a potential barrier of a double-well potential $V(x)$can be calculated using an "instanton". In contrast to a classical particle, there is indeed a non-vanishing probability that the QM particle crosses a region of potential energy higher than its own energy. The Schrödinger equation for the particle reads

$$\frac{d^2\psi}{dx^2} = \frac{2m(E - V(x))}{\hbar^2}\psi \tag{B.9}$$

Using path integrals gives a transition amplitude from one minimum of the double-well x_A to the other minimum x_B

$$k_{A\to B} = \langle x_A | \exp\left(-\frac{iHt}{\hbar}\right) | x_B \rangle = \int dx(t) \exp\left(-\frac{iS[x(t)]}{\hbar}\right) \tag{B.10}$$

where $S[x(t)]$ is the action.

Notice now that with a Wick rotation $it \to \tau$, i.e. passing to imaginary times, we get

$$k_{A\to B} = \int dx(t) \exp\left(-\frac{S_e[x(t)]}{\hbar}\right) \tag{B.11}$$

where we have the Euclidean action

$$S_e[x(t)] = \int_{\tau_A}^{\tau_B} \frac{1}{2}\left(\frac{dx}{d\tau'}\right)^2 + V(x)d\tau' \tag{B.12}$$

The potential energy has changed sign under the Wick rotation and the minima transform into maxima, thereby $V(x)$ exhibits two "hills" of maximal energy. Results obtained from the mathematically well-defined Euclidean path integral may be Wick-rotated back and give the same physical results as would be obtained by using real time variable. As can be seen from this example, calculating the transition probability for the particle to tunnel through a classically forbidden region (the barrier of $V(x)$) corresponds to calculating the transition probability to tunnel through a classically allowed region (with potential $V(X)$) in the Wick-rotated path integral: this transition corresponds to a particle rolling from one hill of a well potential to the other hill. This classical solution of the Euclidean equations of motion is often named "kink solution" and is an example of an instanton.

Appendix C

Chaos and importance sampling

As briefly recalled in Chapter 3, several importance sampling methods developed in the last years used the chaotic behavior of dynamical systems in order to achieve an accelerate sampling of phase space, especially in order to have access to transition regions. The main reason comes from the already cited analogies between reactive paths and chaotic trajectories: we can say, in a somehow 'simplistic' way, that both access to regions in phase space characterized by negative eigenvalues of the hessian matrix of the potential energy. We will not investigate further the relations between chaoticity and rare events; we juste give in this appendix a short review of previous works that preceded the development of transition current sampling and Lyapunov biased TPS.

C.1 The "Lyapunov-weighted dynamics"

Transition current sampling is based on the method presented by Tailleur and Kurchan [15] under the name of Lyapunov-weighted dynamics. We herein clarify the meaning of this expression, also with the aim of make clearer the link of the probability current sampling with the following work presented in this PhD thesis.

The theory of Lyapunov exponents, as presented in Chapter 3, shows that these exponents can be evaluated by observing the distance at a given time between two nearby trajectories in phase space, started sufficiently close enough and then evolving separately. The distance between these two trajectories can be written as in Eq. (3.12).

Let us now consider vectors $\mathbf{u}$ mentioned in Chapter 2: we show here that their dynamics, given by Eq. (2.43), is indeed the very same dynamics of the distance between the two trajectories for an hamiltonian system with overdumped Langevin dynamics. The time evolution of the norm of vectors $\mathbf{u}$ reads

$$\frac{d|\mathbf{u}(t)|^2}{dt} = \sum_i 2u_i\dot{u}_i = -2\sum_{i,j} u_i A_{ij} u_j \tag{C.1}$$

where

$$A_{ij} = \frac{\partial^2 V}{\partial q_i \partial q_j} \tag{C.2}$$

and we have used Eq. (2.43) for the dynamics of $\dot{u}_i$.

Introducing the normalized vectors $v_i = \frac{u_i}{|u_i|}$, whose evolution is given by eq. (2.50), one obtains that the stretch of the distance vectors between the two trajectories is

$$\frac{d|\mathbf{u}(t)|^2}{dt} = 2\sum_{i,j} v_i A_{ij} v_j |\mathbf{u}(t)|^2 \tag{C.3}$$

such that the distance at time t can be evaluated as

$$|\mathbf{u}(t)| = |\mathbf{u}(0)| e^{-\sum_{ij}\int v_i A_{ij} v_j dt} \tag{C.4}$$

From Eq. (3.5) we see that the distance $\delta\mathbf{x}(t)$ between diverging trajectories will be determined by the maximum Lyapunov exponent, predominant at long times:

$$\delta\mathbf{x}(t) = \delta\mathbf{x}(0)\exp(\Lambda_{max} t) \tag{C.5}$$

If we now consider that, as mentioned above, $\mathbf{u} = \delta\mathbf{x}$, looking at Eq. (C.4) we can define the maximum Lyapunov exponent as

$$\Lambda_{max} = -\frac{1}{t}\sum_{ij}\int v_i A_{ij} v_j dt \tag{C.6}$$

and the analogy between the evolution of the norm of vectors $\mathbf{u}$ and the distance between diverging trajectories is evident. This explains why monitoring the evolution of vectors having the aforementined dynamics give direct access to the Lyapunov exponents, and the probability weights used in the Diffusion Monte Carlo algorithm to copy or delete clones are related to Lyapunov exponents.

C.2 Lyapunov exponents and Kolmogorov entropy

Here we briefly acknowledge several works that have been made in the past in order to show the underlying relations between Lyapunov exponents and physical properties of very different systems, from phase transitions[81] to sheared fluid viscosity[80]. In particular, a large attention has been reserved to the observation of relations between chaoticity and local conformation of the potential energy landscape for small inert gas (i. e. Lennard-Jones) clusters [58, 59], with the aim of relating Lyapunov exponents spectra to solid-liquid phase transitions [57].

All these works, concerning systems with many degrees of freedom, start from the determination of the eigenvalues spectrum of Lyapunov exponents[82] and then focus on significant physical observables than can be used to explain the dependence of this spectrum on the potential energy of the system. The most important observable for hamiltonian systems is shown to be the Kolmogorov-Sinai entropy K [84, 52, 68], given by the Pesin theorem as the sum of all positive Lyapunov exponents [85]:

$$K = \sum_{\Lambda_i > 0} \Lambda_i \tag{C.7}$$

thus indicating the degree of chaoticity of the system. Of course, as reported above, to have a full determination of the Kolmogorov entropy the asymptotic value of Lyapunov exponents is needed. However, Hinde *et al.* [58] have shown that is indeed possible to estimate with a very good degree of accuracy the K entropy just using local Lyapunov exponents, i.e. finite-time quantities computed from the position of the system at a given time step on the potential energy landscape, really close to what we have presented in Sec. 3.2.4. Starting from a computation of finite-time Lyapunov exponents based on the eigenvalues jacobian matrix of the map, Hinde *et al.* define, for trajectories with a total of L time steps, a Kolmogorov entropy $\langle K^s \rangle$ given by the average on the trajectory of L/s quantites given by of the product of the s jacobian matrix of the hamiltonian map. The main point is however that comparing the global K entropy, obtained computing the positive Lyapunov over long trajectories, to the quantity $\langle K^1 \rangle$ (given simply by the eigenvalues of the jacobian matrix at *each* time step) shows that the latter is indeed very close to K entropy, especially in the case of large clusters. As the procedure followed is actually the same we proposed in Eq. 3.35, we claim that the consistency checks for the method exposed in [58] are a direct confirmation of the validity of our approach, hence we should be allowed to define the method reported in Chapter 3 as a *local Kolmogorov-entropy bias*.

Appendix D

Lanczos diagonalization algorithm

In Chapter 3 we resorted to the eigenvalue of the hessian matrix λ in order to evaluate the maximum Lyapunov number (Eq. (3.28)) needed to bias the transition path sampling scheme. As recalled, the diagonalization of the hessian matrix can be computationally very expensive for systems with a large number of degrees of freedom. The solution we proposed is resorting to the diagonalization algorithm elaborated by Lanczos [62], that gives the value of the lowest eigenvalue by diagonalizing only a submatrix of the whole hessian matrix, thus saving CPU time. We present here the basis of this algorithm, as reported in Appendix A of [53].

Let $\mathbf{H}[\mathbf{q_0}]$ be the Hessian matrix of the system at the phase-space point $\mathbf{q_0}$:

$$\mathbf{H}_{i,j}[\mathbf{q_0}] = \frac{\partial^2 E[\mathbf{q}_0]}{\partial q_i \partial q_j} \tag{D.1}$$

where $E[\mathbf{q}_0]$ is the energy of the system at point $\mathbf{q}_0$. $\mathbf{H}$ is a real and symmetric matrix. For ARTn we need only the lowest eigenvalue, λ_1, and its eigenvector, $\mathbf{v}_1$. The Lanczos algorithm is an efficient way to extract a limited spectrum of eigenvalues and eigenvectors and it doesn't require evaluating the full $3N \times 3N$ matrix $\mathbf{H}$. The diagonalization of the full Hessian matrix is replaced by that of a $l \times l$ trigonal matrix ($l \ll 3N$) and the $\mathbf{H}$ matrix needs to be known only in the l dimensional space of the Lanczos vectors.

In the following we describe how the Lanczos scheme is used to calculate λ_1 and $\mathbf{v}_1$. First of all we must build the Lanczos basis in which the $\mathbf{H}$ matrix is trigonal. Consider $\mathbf{u}_0$ a *random* normalized vector in $\mathcal{R}^{3N}$ space. The result of the application of $\mathbf{H}$ on $\mathbf{u}_0$ can be decomposed as a linear combination of this random vector and a second normalized one, $\mathbf{u}_1$, orthogonal to $\mathbf{u}_0$:

$$\mathbf{H}\mathbf{u}_0 = a_0\mathbf{u}_0 + b_1\mathbf{u}_1 \tag{D.2}$$

The application of the Hessian on $\mathbf{u}_1$ becomes:

$$\mathbf{H}\mathbf{u}_1 = a_1\mathbf{u}_1 + b_1'\mathbf{u}_0 + b_2\mathbf{u}_2 \tag{D.3}$$

where $\mathbf{u}_2$ is a normalized vector which is orthogonal to the first two. Since $\mathbf{H}$ is a symmetric matrix:

$$\mathbf{u}_1 \cdot (\mathbf{H}\mathbf{u}_0) = \mathbf{u}_0 \cdot (\mathbf{H}\mathbf{u}_1) \tag{D.4}$$

and therefore $b_1 = b'_1$. The full recursion scheme becomes:

$$\mathbf{H}\mathbf{u}_k = a_k\mathbf{u}_k + b_k\mathbf{u}_{k-1} + b_{k+1}\mathbf{u}_{k+1} \tag{D.5}$$

for $0 < k < l-1$ and the closure of the recursion for k=l-1:

$$\mathbf{H}\mathbf{u}_{l-1} = a_{l-1}\mathbf{u}_{l-1} + b_{l-1}\mathbf{u}_{l-2}. \tag{D.6}$$

In this l-dimensional basis ($\mathbf{u}_0$, $\mathbf{u_1}$, ..., $\mathbf{u_{l-1}}$) the $\mathbf{H}$ matrix is trigonal:

$$\mathbf{T}_l = \begin{pmatrix} a_0 & b_1 & 0 & \cdots & 0 \\ b_1 & a_1 & b_2 & \cdots & 0 \\ 0 & b_2 & a_2 & \cdots & 0 \\ 0 & \ddots & \ddots & \cdots & 0 \\ 0 & & b_{l-2} & a_{l-2} & b_{l-1} \\ 0 & & 0 & b_{l-1} & a_{l-1} \end{pmatrix} \tag{D.7}$$

The central point of the Lanczos method is that it can be demonstrated that the lowest eigenvalue of the $\mathbf{H}$ matrix, $\lambda_1[\mathbf{H}]$, is the limit of the series $\lambda_1[\mathbf{T}_l]$ with $l \to 3N$. Finally the eigenvector $\mathbf{v}_1[\mathbf{H}]$ corresponding to the lowest eigenvalue $\lambda_1[\mathbf{H}]$ can be approximated by the eigenvector associated to the lowest eigenvalue of the $\mathbf{T}_l$, $\mathbf{v}_1[\mathbf{T}_l]$.

The vectors $\mathbf{H}\left[\mathbf{q}_0\right]\mathbf{u}$ can be calculated by finite difference on the forces by performing a Taylor expansion of the forces around $\mathbf{q}_0 + \delta_L\mathbf{u}$ ($\delta_L \ll 1$), a point in the neighborhood of $\mathbf{q}_0$ in the direction $\mathbf{u}$:

$$\mathbf{H}\left[\mathbf{q}_0\right]\mathbf{u} = -\frac{\mathbf{f}\left(\mathbf{q}_0 + \delta_L\mathbf{u}\right) - \mathbf{f}\left(\mathbf{q}_0\right)}{\delta_L} + \mathcal{O}\left(\delta_L^2\right). \tag{D.8}$$

This expansion can also be made $\mathcal{O}(\delta_L^3)$:

$$\mathbf{H}\left[\mathbf{q}_0\right]\mathbf{u} = -\frac{\mathbf{f}\left(\mathbf{q}_0 + \delta_L\mathbf{u}\right) - \mathbf{f}\left(\mathbf{q}_0 - \delta_L\mathbf{u}\right)}{2\delta_L} + \mathcal{O}\left(\delta_L^3\right). \tag{D.9}$$

It is important to note that using this $\mathcal{O}(\delta_L^3)$ approximation requires two times more force evaluations than Eq. D.8: both $\mathbf{f}\left(\mathbf{q}_0 + \delta_L\mathbf{u}\right)$ and $\mathbf{f}\left(\mathbf{q}_0 - \delta_L\mathbf{u}\right)$ must be evaluated compared to only $\mathbf{f}\left(\mathbf{q}_0 + \delta_L\mathbf{u}\right)$ in the case of Eq. D.8, since $\mathbf{f}\left(\mathbf{q}_0\right)$ is computed anyway at every step for the minimization in the hyperplane orthogonal to $\mathbf{v}_1$ and for the test of convergence to the saddle point.

The parameters which must be optimized for the calculation of the Lanczos coefficients (a_k, b_k) and vectors $\mathbf{u}_k$ from Eqs. D.2, D.5 and D.6 are: the size of the Lanczos basis set, l, and the step of the numerical derivative of forces for the Hessian, δ_L. In [53], authors investigate self interstitials, and use $l = 15$ and $\delta_L = 10^{-3}$ Å with an $\mathcal{O}(\delta_L^2)$ expansion. This choice results from an analysis performed on a test system with 1025 atoms (one

self-interstitial defect in a $8a_0 \times 8a_0 \times 8a_0$ bcc cell). A random deformation is applied to the minimum energy configuration ($\langle 110 \rangle$ orientation of the dumbbell) in order to induce an imaginary frequency. Taking $l = 15$, we have calculated λ_1 using an expansion of order either 2, Eq. D.8, or 3, Eq. D.9, and three different values of $\delta_L = 10^{-2}$, 10^{-3}, and 10^{-4} Å.

The numerical stability of the algorithm is tested by performing an iterative Lanczos diagonalization. Successive iterations of l Lanczos steps are performed, where each new iteration, i, is started by taking for u_0 the last vector of the Lanczos basis set, u_{l-1}, of the previous Lanczos iteration, $i-1$. In both cases $\delta_L = 10^{-4}$ Å shows numerical instabilities as function of number of Lanczos iterations, in particular for the order 2 expansion. For $\delta_L = 10^{-2}$ Å some numerical noise appears only in the case of $\mathcal{O}(\delta_L^2)$ force derivatives. But for $\delta_L = 10^{-3}$ Å the same accuracy is obtained in both cases. In conclusion, the maximum efficiency can be obtained using Eq. D.8 and $\delta_L = 10^{-3}$ Å.

The very same procedure has been carried on to optimize parameters in the case of $LJ_3 8$ in Chapter 3, and vacancy and divacancy migration in Chapter 4.

In a method like ARTn, where successive Hessian matrices of systems which differ by only small displacements must be evaluated, the efficiency of the Lanczos method can be considerably improved by optimizing the choice of the first vector, u_0 in Eq. D.2. As for an iterative diagonalization, the idea is to take for u_0 at every ARTn step, i, the last vector of the Lanczos basis set, u_{l-1}, of the previous ARTn step, $i-1$. If the displacements between ARTn steps are small, the convergence with the size of the Lanczos basis, l, after i ARTn steps is close to that of a basis set of size $i \times l$ using a random u_0 vector. The convergence with the size of the Lanczos basis set is therefore not a problem. In practice $l = 15$ provides a good accuracy after $i \sim 4$ ARTn steps and excellent after 20 steps.

Appendix E

Optimal estimators in MBAR method

We present here the basis on the multistate Bennett acceptance ratio (MBAR) method, used in Chapter 3 to unbias reaction rates obtained from LyTPS simulations.

MBAR is based on the principle of the *extended bridge sampling* [77]: given a set of biased distribution associated with the canonical equilibrium ensemble, unbiased averages of physical observables are recovered from biased ones, provided there is a sufficient overlap between biased and the unbiased distributions. Given a path distribution

$$\rho_\alpha(\mathbf{z}) = \frac{q_\alpha(\mathbf{z})}{Z_\alpha} \tag{E.1}$$

for path weights $q_\alpha(\mathbf{z})$ corresponding to a precise α-ensemble (where $Z_\alpha \equiv \int \mathcal{D}\mathbf{z} q_\alpha(\mathbf{z})$ is the associated partition function taken over all possible paths), the average of a path-dependent observable $\mathcal{O}(\mathbf{z})$ in that α-ensamble reads

$$\langle \mathcal{O} \rangle_\alpha \equiv \int \mathcal{D}\mathbf{z} \mathcal{O}(\mathbf{z}) \rho_\alpha(\mathbf{z}) \tag{E.2}$$

Averages computed in different path ensembles, say for two different bias α and α', are, however, related by the *importance sampling identity*

$$\frac{\langle \mathcal{O} q_{\alpha'} \rangle_\alpha}{\langle \mathcal{O} q_\alpha \rangle_{\alpha'}} = \frac{Z_{\alpha'}}{Z_\alpha} \tag{E.3}$$

as

$$\begin{aligned} Z_\alpha \langle \mathcal{O} q_{\alpha'} \rangle_\alpha &= \left[\int \mathcal{D}\mathbf{z} q_\alpha(\mathbf{z}) \right] \cdot \int \mathcal{D}\mathbf{z} \mathcal{O}(\mathbf{z}) \rho_\alpha(\mathbf{z}) q_{\alpha'}(\mathbf{z}) = \\ &= \left[\int \mathcal{D}\mathbf{z} q_{\alpha'}(\mathbf{z}) \right] \cdot \int \mathcal{D}\mathbf{z} \mathcal{O}(\mathbf{z}) \rho_{\alpha'}(\mathbf{z}) q_\alpha(\mathbf{z}) = \\ &= Z_{\alpha'} \langle \mathcal{O} q_\alpha \rangle_{\alpha'} \end{aligned}$$

Once one knows the unnormalized probability weights q_α for the each α-ensemble, averages of $\langle \mathcal{O} \rangle_{\alpha'}$ for every ensemble $\alpha' \neq \alpha$ can be computed. For a set of K different values of the bias α, a set (namely, a Markov chain) of $\mathcal{M}_\alpha$ trajectories are sampled for

each bias value. Estimating the averages $\langle \mathcal{O} \rangle_\alpha$ as the sample mean

$$\langle \mathcal{O} \rangle_\alpha \approx \mathbb{E}^\alpha_{\mathcal{M}_\alpha}[\mathcal{O}] = \frac{1}{\mathcal{M}_\alpha} \sum_{m=1}^{\mathcal{M}_\alpha} \mathcal{O}(\mathbf{z}^\alpha) \tag{E.4}$$

we rewrite Eq. (E.3) as a set of K importance sampling identities

$$\sum_{\alpha'=1}^{K} \frac{\hat{Z}_\alpha}{\mathcal{M}_\alpha} \sum_{m=1}^{\mathcal{M}_\alpha} \mathcal{O}(\mathbf{z}^\alpha) q_{\alpha'}(\mathbf{z}) = \sum_{\alpha=1}^{K} \frac{\hat{Z}_{\alpha'}}{\mathcal{N}_{\alpha'}} \sum_{m=1}^{\mathcal{M}_{\alpha'}} \mathcal{O}(\mathbf{z}^{\alpha'}) q_\alpha(\mathbf{z}) \tag{E.5}$$

whose unknowns are a family of estimators for the partition function $\hat{Z}_\alpha$, parametrized by the choice of $\mathcal{O}(\mathbf{z}^\alpha)$, all asymptotically consistent, but with different statistical efficiencies. The choice

$$\mathcal{O}(\mathbf{z}^\alpha) = \frac{\mathcal{M}_{\alpha'} \hat{Z}^{-1}_{\alpha'}}{\sum_{k=1}^{K} \mathcal{M}_k \hat{Z}^{-1}_k q_k(\mathbf{z})} \tag{E.6}$$

makes the asymptotic covariance of the partition function ratio in Eq. (E.3) minimal. Using Eq. (E.6), Eq. (E.5) simplifies to the optimal extended bridge sampling estimator,

$$\hat{Z}_\alpha = \sum_{\alpha'=1}^{K} \sum_{m=1}^{\mathcal{M}_\alpha} \left[\sum_{k=1}^{K} \frac{\mathcal{M}_k}{\hat{Z}_k} \frac{q_k(\mathbf{z}^m_{\alpha'})}{q_\alpha(\mathbf{z}^m_{\alpha'})} \right]^{-1} \tag{E.7}$$

In the large sample limit, the error in the ratios $\hat{Z}_\alpha / \hat{Z}_{\alpha'}$ is normally distributed, and the asymptotic covariance matrix $\hat{\mathbf{\Theta}} = cov(\ln \hat{Z}_\alpha, \ln \hat{Z}_{\alpha'})$ for Eq. (E.7) is estimated by

$$\hat{\mathbf{\Theta}} = \mathbf{W}^T (\mathbf{I} - \mathbf{W}\mathbf{M}\mathbf{W}^T)^+ \mathbf{W} \tag{E.8}$$

where $\mathbf{I}$ is the identity matrix of dimension $\mathcal{M} = \sum_{\alpha=1}^{K} \mathcal{M}_\alpha$ equal to the total number of paths sampled, and $\mathbf{M} = diag(\mathcal{M}_\alpha, ..., \mathcal{M}_K)$. The superscript + indicates a Moore-Penrose pseudoinverse, see Ref. [66]. $\mathbf{W}$ is the $\mathcal{M} \times K$ matrix of weights

$$W_{m,\alpha} = \hat{Z}^{-1}_\alpha \frac{q_\alpha(\mathbf{z}^m)}{\sum_{k=1}^{K} \mathcal{M}_k \hat{Z}^{-1}_k q_k(\mathbf{z}^m)} \tag{E.9}$$

In this matrix, the distribution in which path $\mathbf{z}$ are sampled is irrelevant, hence subscripts α are omitted.

Expectation values of any path dependent observable $\mathcal{F}_\alpha$ estimated in each α-biased ensemble can be recovered in this framework defining additional path ensembles with unnormalized densities

$$q_{\mathcal{F}_\alpha}(\mathbf{z}) = \mathcal{F}_\alpha q_\alpha(\mathbf{z}) \tag{E.10}$$

such that $Z_{\mathcal{F}_\alpha} \equiv \int \mathcal{D}\mathbf{z} q_{\mathcal{F}_\alpha}(\mathbf{z})$ is the related path partition function. The matrix $\mathbf{W}$ in Eq. (E.9) is augmented by one column with elements

$$W_{m,\mathcal{F}_\alpha} = \hat{Z}^{-1}_{\mathcal{F}_\alpha} \frac{\mathcal{F}_\alpha q_\alpha(\mathbf{z}^m)}{\sum_{k=1}^{K} \mathcal{M}_k \hat{Z}^{-1}_k q_k(\mathbf{z}^m)} \tag{E.11}$$

and the estimator $\mathbb{E}_{\alpha}^{MBAR}[\mathcal{F}] = \hat{\mathcal{F}}_{\alpha}$ for the path ensemble average can be written in terms of weight matrix elements

$$\hat{\mathcal{F}}_{\alpha} = \sum_{m=1}^{\mathcal{M}_{\alpha}} W_{m,\alpha} \mathcal{F}(\mathbf{z}_{\alpha}^{m}) \tag{E.12}$$

with an uncertainity estimated by

$$\sigma^2(\hat{\mathcal{F}}_{\alpha}) = \hat{\mathcal{F}}_{\alpha}^2 (\hat{\Theta}_{\mathcal{F}_{\alpha}\mathcal{F}_{\alpha}} + \hat{\Theta}_{\alpha\alpha} - 2\hat{\Theta}_{\mathcal{F}_{\alpha}\alpha}). \tag{E.13}$$

In order to compute the expectation values of the observables $\mathcal{F}_{\alpha}$, a self consistent algorithm can be set up. Numerical recipes to obtain these estimations have been furnished by J. Chodera [91].

Appendix F

Reaction rate constants theory

Reaction rate constants are one of the most significative observables for many body system exhibiting thermally activated structural transitions through energy barriers crossing. Their computation is one of the main challenges in a wide range of research sectors belonging to physics, chemistry or biology where rare transitions occur between different stable or metastable states. Several theories have been elaborated in order to investigate analytically and numerically reaction rates, starting from the main work by Kramers in 1940. A very useful and detailed review about Kramers reaction rate theory and its developments has been written by Hänggi *et al.* [17]. We follow this review to write the second part of appendix.

The bottleneck of rate constants computation is that observing reactive trajectories in a finite simulation time is very unusual for systems with high free energy barriers, so that a correct estimation of reaction rates is seldom possible. Different approaches have been developed in the past to bypass this problem, mainly based on the transition state theory (TST), either following a "chemical" macroscopic approach (see for example [2]) or considering microscopic quantities, such as in the Bennett-Chandler method [71]. For applications in physical metallurgy studies, such as the computation of reaction constants to study diffusion coefficients [72], the first seminal result from transition state theory was reelaborated by Vineyard [107], as presented for instance in [51].

We first present here the population correlation function ("macroscopic") approach widely used in chemistry; we then recall the basis of reaction rate theory, mainly following the review [17] presenting the Bennet-Chandler method [77, 75, 71]. Finally, we expose the basis of the transition state theory for reaction constants [17].

F.1 Phenomenological approach

Reaction rates can be computed - from a chemical point of view - counting the number of species of a given system that have undergone a transition from the reactant to the products state. The number of systems components belonging to one of the two states is usually called population, and evolves in time along the reaction. The time correlation function of these populations indicates the time evolution of the system, and can be written

as

$$C(t) = \frac{\langle c_A(0) c_A(t) \rangle}{\langle c_A(0) \rangle} \tag{F.1}$$

indicating the correlation between the population in the A state at time 0 and time t: this traces the evolution of the system from the reactants towards the products. The population correlation function can indeed be understood as a conditional probability of having thesystem at a given time t in state B whereas it was in state A at time $t = 0$. To this aim, we substitute, without any loss of generality, the probability of occupations $p_{A,B}$ of states A and B to the real populations $c_{A,B}$: the correlation function can then be explicitly calculated from the expression of the occupation probabilityof states A (reactant) and B (product). The master equations for such a system can be written as [54, 2]

$$\begin{cases} \dot{p}_A(t) = & -k_{A\to B} p_A(t) + k_{B\to A} p_B(t) \\ \dot{p}_B(t) = & k_{A\to B} p_A(t) - k_{B\to A} p_B(t) \end{cases} \tag{F.2}$$

where $p_{A,B}$ are the occupation probabilities for the two states, and $k_{AB,BA}$ are the reaction rate constants for passages between them. Given the occupation probabilities at time $t = 0$ and the equilibrium condition, through a detailed balance relation

$$k_{A\to B} p_A^{eq} = k_{B\to A} p_B^{eq} \tag{F.3}$$

time dependent solutions are

$$\begin{cases} p_A(t) = p_A^{eq} & -e^{-(k_{A\to B}+k_{B\to A})t} \left[p_B(0) p_A^{eq} - p_A(0) p_B^{eq} \right] \\ p_B(t) = p_B^{eq} & -e^{-(k_{A\to B}+k_{B\to A})t} \left[p_A(0) p_B^{eq} - p_B(0) p_A^{eq} \right] \end{cases} \tag{F.4}$$

Thus, the conditional probability $C_{AB}(t) = p_B(t) \mid p_A(0)$ can be explicitly expressed using the above solutions, giving [1]

$$C(t) \approx p_B^{eq} \left(1 - \exp\left\{-t/\tau_{rxn}\right\}\right) \tag{F.6}$$

[1] Indeed, as

$$p_A(0) = p_A^{eq} \left(\frac{1 - p_B(0)}{1 - p_B^{eq}} \right) \tag{F.5}$$

the conditional probability gives

$$\begin{aligned} C(t) &= \left\{ p_B^{eq} - e^{-(k_{A\to B}+k_{B\to A})t} \left[p_A(0) p_B^{eq} - p_B(0) p_A^{eq} \right] \right\} = \\ &= \left\{ p_B^{eq} - e^{-(k_{A\to B}+k_{B\to A})t} \left[p_A^{eq} \left(\frac{1 - p_B(0)}{1 - p_B^{eq}} \right) p_B^{eq} - p_B(0) p_A^{eq} \right] \right\} \\ &= p_B^{eq} \left\{ 1 - e^{-(k_{A\to B}+k_{B\to A})t} \right\} + p_B(0) e^{-(k_{A\to B}+k_{B\to A})t} \end{aligned}$$

If the system was originally set in the A configuration, $p_B(0) = 0$ and one has simply $C(t) = p_B^{eq} \left\{ 1 - e^{-(k_{A\to B}+k_{B\to A})t} \right\}$.

where the relaxation time is $\tau_{rxn} \equiv (k_{A\to B} + k_{B\to A})^{-1}$. In order to proceed further, it has to be stressed that the basic assumption relying under this populations correlation treatment is the presence of a well separated time scale for processes occurring between 'fast' intra-funnel relaxation of the system, having a typical time constant τ_{mol}, and processes indicating passages *between* funnels, thus needing much longer times: however, at such long times the dynamics can be described using the phenomenology of macroscopic kinetics, thus the asymptotic behavior of this correlation function only depends on the forward and backward reaction rate constants $k_{A\to B}$ and $k_{B\to A}$.

The reactive flux of particles (or probability) flowing from state A towards B per unit time is now defined as $k(t) \equiv \frac{dC(t)}{dt}$. When time scales between the intra-basin relaxation dynamics, having a characteristic time τ_{mol}, and τ_{rxn} is well separated, i.e. $\tau_{mol} \ll \tau_{rxn}$, it is possible to further approximate in the intermediate time regime $\tau_{mol} < t \ll \tau_{rxn}$ the correlation function developing the exponential at the first order, getting

$$\begin{aligned} k(t) &\equiv \frac{dC(t)}{dt} \cong (k_{A\to B} + k_{B\to A}) p_B^{eq} \{1 - (k_{A\to B} + k_{B\to A})t\} = \\ &= k_{A\to B} \{1 - (k_{A\to B} + k_{B\to A})t\} \end{aligned}$$

where in the last line the detailed balance condition $k_{A\to B} p_A^{eq} = k_{B\to A} p_B^{eq}$ has been used to eliminate p_B^{eq}. Finally, in the regime $(k_{A\to B} + k_{B\to A})t \ll 1$, one can linearize the correlation function finding thus the slope of $C(t)$ for this intermediate time regime is the reaction rate we were looking for.

F.1.1 A simple model for systems with two stable basins and a metastable transition state

In many systems the two main states (reactant and product) are not separated by a single barrier, but by a set of intermediate metastable states. Some approximations are therefore necessary to recover the reaction rate values, using the approach reported above. Here we mainly follow the way this problem has been solved by Wales [38, 79].

The master equations for a system with one (or more) intermediate phase space region I are written as

$$\begin{cases} \dot{p}_A(t) = & -k_{A\to B} p_A(t) + k_{I\to A} p_I(t) \\ \dot{p}_I(t) = & k_{A\to I} p_A(t) - (k_{I\to A} + k_{I\to B}) p_I(t) + k_{B\to I} p_B(t) \\ \dot{p}_B(t) = & k_{I\to B} p_I(t) - k_{B\to I} p_B(t) \end{cases} \tag{F.7}$$

where reactions directly happening between the two main basins have been neglected. In general, for I we can indicate one single basin as well as a set of intermediary metastable states. This is the case for systems where the separating barrier between A and B is quite large, or it contains a set of metastable "transition step" minima through which the system passes in the transition from A to B.

Exact solutions to this ordinary derivative equation system are possible, but looks indeed rather complicated. One possible solution is a steady-state approximation for the intermediate metastable state, as they are supposed having a low occupation probability, i.e. $\dot{p}_I \simeq 0$. The above system therefore simplifies in

$$\begin{cases} \dot{p}_A(t) = & -\frac{k_{A\to I}k_{I\to B}}{(k_{I\to A}+k_{I\to B})}p_A(t) + \frac{k_{B\to I}k_{I\to A}}{(k_{I\to A}+k_{I\to B})}p_B(t) \\ \dot{p}_B(t) = & \frac{k_{A\to I}k_{I\to B}}{(k_{I\to A}+k_{I\to B})}p_A(t) - \frac{k_{B\to I}k_{I\to A}}{(k_{I\to A}+k_{I\to B})}p_B(t) \end{cases} \tag{F.8}$$

" and one can reconstruct the reaction constant between states A and B calculating, with the previously exposed method for a two state system, first the reaction constants between one of the main basin and the intermediate one, and then from the intermediate to the second stable state:

$$k_{A\to B} = \frac{k_{A\to I}k_{I\to B}}{(k_{I\to A} + k_{I\to B})} \tag{F.9}$$

Once again, it has however to be stressed that the populations correlation function *method* is valid under *strict* hypothesis of separation of the time regimes, for instance when the passage from one basin to another can be described as a rare event. In the case of high-energy metastable states, if the barriers between the metastable state and the stable states are too low (such that the system spontaneously tend to fall from the I state to A or B), this approximation is no more valid. One should then re-correct the reaction constants obtained for the passage time from the metastable to the stable configurations.

F.2 Transition State Theory

We present here large excerpts from the aforementioned review by Hänggi *et al.* [17]. The very beginning of the study of escape rates from metastable basins as a function of the inverse temperature $\beta = 1/k_B T$ dates back to the Van't Hoff - Arrhenius law,

$$k = \nu \exp\left(-\beta E_{barr}\right) \tag{F.10}$$

where E_{barr} is the energy barrier separating the departure metastable state to the closer stable state, and ν is an unknown -but really important, see below - prefactor. The next major development is due among others chemical physicists to Eyring, who expressed the reaction rate in terms of properties of the underlying potential energy landscape, and accounted for quantum and statistical mechanics concepts like the Planck's constant h and the partition functions Z^{basin} and Z^{saddle}, respectively related to the metastable state and the activated complex (i.e. the system on the saddle point): he wrote the formula

$$k = \kappa \left(\frac{k_B T}{h}\right) \frac{Z^{saddle}}{Z^{basin}} \exp\left(-\beta E_{barr}\right) \tag{F.11}$$

where appears the *transmission coefficient* κ. This last parameter originally was introduced to account for those trajectories in phase space that cross the transition state, but successively come back to the original metastable basin without undergoing a complete transition from the reactants state to the products one. Therefore, one usually has $\kappa \leq 1$, and the true reaction rate k is always *lower* than the *Transition State Theory* reaction constant defined as

$$k_{TST} \equiv \left(\frac{k_B T}{h}\right) \frac{Z^{saddle}}{Z^{basin}} \exp\left(-\beta E_{barr}\right) \tag{F.12}$$

The escape process as a 'noise-assisted' reaction depending on temperature and friction has successively been assessed by Kramers, following the relation between the microscopic Brownian motion and its probabilistic description by a Fokker-Planck equation, as well deeply developing the low- and high-friction limits of such a dynamics.

Transition State Theory (TST) is fundamentally a classical mechanical theory, although some leading quantum corrections are accounted for. The main hypothesis are (i) thermal equilibrium and (ii) a 'no-recrossing' assumption, i.e. any trajectory crossing the saddle points never returns back. It is evident from this last hypothesis why a transmission coefficient has to be accounted for in the calculation of 'true' *phenomenological* reaction constants.

The TST rate is computed from the total flux of classical trajectories passing from reactants to products state, crossing the transition region. This flux is calculated either with a delta-function weighting accounting only for trajectories of a given energy, for microcanonical TST, or with a usual Boltzmann weight for canonical TST. The choice of the transition region, i.e. the dividing surface between reactants and products, is important in order to satisfy hypotesis (ii): indeed, this choice can strongly affects the rate of recrossing, and it has been showed that the probability of correlate recrossings increases with the level of coarse graining of the used reaction coordinate. It has to be stressed however that for any dividing surface, the TST rate always *overestimates* the true reaction rate. Finally, we note that by use of the thermodynamic relation $Z = \exp\left(-\beta F\right)$, the TST rate can be recast in the common form

$$k_{TST} = \left(\frac{k_B T}{h}\right) \exp\left(-\beta \Delta F_{barr}\right) \tag{F.13}$$

where $\Delta F_{barr} = E_{barr} - T\triangle S$ is the free energy barrier between reactants and products.

F.2.1 Separation of time scales

The time scale of escape from a given basin clearly depends on the size of fluctuations

$$f(t) = x(t) - \langle x(t) \rangle \tag{F.14}$$

related to the energy scale of the thermal noise E_{noise}. The escape from basin A will be an infrequent event if $E_{noise} << E_{barr}$, where E_{barr} is the height of the energy barrier

separating state A from B. For system connected to a heath bath at temperature T, the noise is due to thermal fluctuations and the condition reads $\beta E_{barr} >> 1$. The time scale describing the decay within basin A is called relaxation time and reads

$$\tau_{rxn} \approx \left(\frac{d^2 V}{dx^2} \right)^{-1/2} \tag{F.15}$$

where V is the potential energy function. This relaxation time is well separated from the escape time τ_e, as

$$\tau_e \approx \tau_{rxn} \exp(\beta E_{barr}) >> \tau_{rxn} \tag{F.16}$$

All the fast time scales (concerning noise or velocity correlation times, [51]) can be lumped into the intra funnel relaxation time τ_{rxn}, and the escape rate is simply given by

$$k \approx \tau_e^{-1}. \tag{F.17}$$

F.2.2 Reactive flux method

The basic assumptions needed to compute reaction rates between two (or more) equilibrium configurations are the presence of a detailed balance relation between states, and the possibility of resorting to fluctuation-dissipation relation that enables us to write time correlation functions, thanks to the Onsager regression hypothesis. Indeed, the underlying idea of this chemical rate theory is that the spontaneous fluctuations from one state to another at equilibrium are the same as those fluctuation one observes during the relaxation from a non-equilibrium state towards equilibrium. The following description is again mainly taken from Hänggi [17].

For equilibrium systems with simple two-state kinetics, it is possible to derive an approximate but simple expression to calculate reaction constants. Given a many-particle system prepared in state A, the populations of particles in state A (say, the reactant) and state B (say, the product) can be indicated respectively as c_A and c_B, and undergo fluctuations given by the spontaneous transitions between them. The problem of the choice of a dynamical observable, like a *reaction coordinate*, in the definition of the two states will be examined later on.

$$\begin{cases} \dot{c}_A(t) = & -k_{A\to B} c_A(t) + k_{B\to A} c_B(t) \\ \dot{c}_B(t) = & k_{A\to B} c_A(t) - k_{B\to A} c_B(t) \end{cases} \tag{F.18}$$

If the system is prepared in a (large) nonequilibrium initial concentration $c_A(0)$, this concentration will decay exponentially to to the equilibrium value $\bar{c}_A$ as

$$c_A(t) - \bar{c}_A = (c_A(0) - \bar{c}_A) \exp\left[- \left(k_{A\to B} + k_{B\to A} \right) t \right] \tag{F.19}$$

Let a dividing surface be placed between products and reactants basins A and B, and let us introduce a *reaction coordinate* $x(\mathbf{q})$, function of all the configurational degrees of freedom

of the system. By convention, we will assume $x < 0$ in basin A and $x > 0$ in basin B, while the dividing surface is located at $x = 0$. Using an indicator (Heavyside) function $h_{A,B}$, defined for a generic state Ω as

$$h_\Omega(x) = \begin{cases} 1 & x \in \Omega \\ 0 & x \notin \Omega \end{cases} \tag{F.20}$$

one can express the equilibrium population in basin A as $\bar{c}_A = \langle h_A \rangle$.

According to Onsager's regression hypotesis, the exponential decay of the initial nonequilibrium deviation to its equilibrium value has the same dynamic law as the equilibrium correlation function of the fluctuation

$$\delta h_A\left(x(t)\right) = h_A(x(t)) - \langle h_A \rangle \tag{F.21}$$

thus

$$\frac{\langle \delta h_A\left(x(0)\right) \delta h_A\left(x(t)\right) \rangle}{\left\langle \delta h_A^2 \right\rangle} = \exp\left[-\left(k_{A\to B} + k_{B\to A}\right) t\right] \tag{F.22}$$

For intermediates times $\tau_{rxn} < t << \tau_e$, the TST expression can now be recovered using the *reactive flux* method: this flux is given by

$$\begin{aligned} \frac{\left\langle \delta h_A\left(x(0)\right) \delta \dot{h}_A\left(x(t)\right) \right\rangle}{\left\langle \delta h_A^2 \right\rangle} &= -\frac{\langle \delta h_A\left(x(0)\right) \dot{x}(0) \delta h_A\left(x(t)\right) \rangle}{\left\langle \delta h_A^2 \right\rangle} = \\ &= -\left(k_{A\to B} + k_{B\to A}\right) \exp\left[-\left(k_{A\to B} + k_{B\to A}\right) t\right] \end{aligned}$$

and as we are in the regime $t \ll \left(k_{A\to B} + k_{B\to A}\right)^{-1}$, the total escape rate reads

$$k_{A\to B} + k_{B\to A} = \frac{\langle \delta h_A\left(x(0)\right) \dot{x}(0) \delta h_A\left(x(t)\right) \rangle}{\bar{c}_A \bar{c}_B}. \tag{F.23}$$

Equivalently, the forward rate can be obtained as

$$k_{A\to B} = \frac{\langle \delta h_A\left(x(0)\right) \dot{x}(0) \delta h_A\left(x(t)\right) \rangle}{\langle h_A(x) \rangle} \tag{F.24}$$

Note that the last two equation hold equally well for weak or strong friction cases. If we now take the limit $t \to 0^+$, the rate can be expressed as an equilibrium average of a one-way flux at the transition state $x = 0$, we get the TST rate

$$k_{TST} = \frac{\langle \delta\left(x(0)\right) \dot{x}(0) h_A\left(\dot{x}(0)\right) \rangle}{\langle h_A(x) \rangle} \tag{F.25}$$

that always overestimates the true rate [75]

$$k_{TST} \geq k_{A\to B} \tag{F.26}$$

as in TST recrossings of reactive trajectories are neglected, as TST assumes that all trajectories heading toward the product region (with $\dot{x}(0) > 0$) at the dividing surface in $x = 0$ will all end up in the product basin.

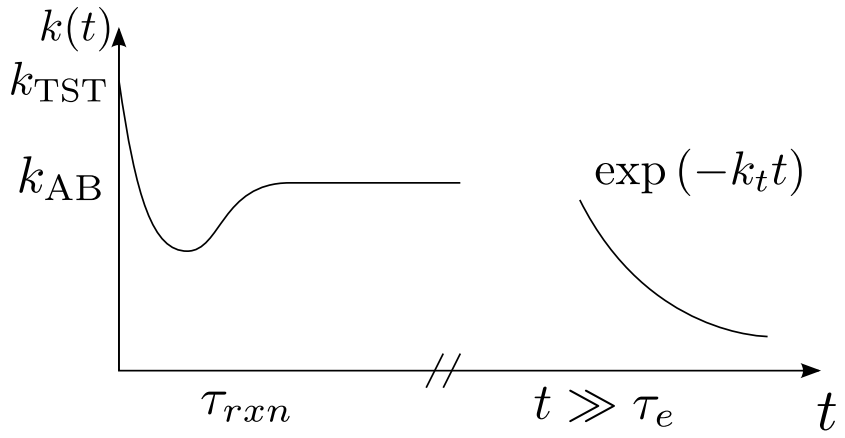

Figure F.1: Reactive flux as a function of time. The upper bound given by TST value; at intermediate times, larger than the intra-funnel relaxation time τ_{rxn}, the reactive flux joins the plateau value $k_{A\to B}$ corresponding to the phenomenological reaction constant. At longer times, comparable to the escape time $\tau_e \approx k_t^{-1}$, the reactive flux decays exponentially.

The transition state is identified as a dividing surface separating reactants from products, or more generally, any two physical states that are separated by a bottleneck in phase space. As already mentioned, the two key assumptions to TST (i) thermodynamic equilibrium for all degrees of freedom (all deviations from the thermal equilibrium distribution, such as the Boltzmann distribution, are neglected), and (ii) any orbit crossing the dividing surface will not recross it. The TST rate is proportional to the total of classical trajectories from reactant to product side of the dividing surface. This is calculated either with the Boltzmann weighting function at a given temperature T (canonical TST) or with a delta-function weighting counting only for the trajectories of a given total energy E (microcanonical TST)

The conventional choice for the dividing surface is a saddle point located between reactants and products is the subspace perpendicular to the unstable mode, determined by normal-mode analysis of small vibrations around the saddle point. From the assumptions in (i) and (ii) it follows that microcanonical TST is exact only if no trajectory of a given energy crosses the transition-state dividing surface more than once; canonical TST is exact if no trajectory, of any energy whatever, recrosses the dividing surface. We stress that for any dividing surface the TST rate is always an upper bound to the true rate.

The number of recrossing events of the reaction coordinate depends strongly on the level of coarse graining in the phase space of the total system. If the reaction is described by all degrees of freedom in the full phase space of the reacting system plus bath, a classical trajectory has generally very little chance of returning to the narrow bottleneck region around the saddle point with activation energy E_{barr}. The probability of correlated recrossings increases for increasing coarse-graining for the reaction coordinate. In other words, simple TST is expected to fail badly in complex systems if the dividing surface is restricted to lie on a low-dimensional subspace. In view of the fact that TST always overestimates the true rate, the dividing surface should be chosen so as to minimize the flux through it.

F.2.3 Kramers rate theory

Transition state theory reduces to the Kramers rate theory, derived from the Fokker-Planck-Kramers equation of Chapter 1, for systems in one dimension. The rate is obtained with a 'flux over population' approach:

$$k_{A\to B} = \frac{j}{c_A} \tag{F.27}$$

where j is the flux of particle going from state A to B, and c_A is the population in state A. The main ansatz made by Kramers is to assume the probability density

$$\rho(x,v) = \xi(x,v)\exp\left\{-\frac{1/2mv^2 + V(x)}{k_BT}\right\} \tag{F.28}$$

where ξ is a function that has to be determined taking into account boundary conditions for the system. As shown in [17], assuming a linearized potential

$$U(x) = U(x_A) + 1/2m\omega_0^2(x - x_A)^2 \tag{F.29}$$

the population in the A basin is

$$c_A = \frac{2\pi k_BT}{m\omega_0} Z^{-1}\exp[-\beta U(x_A)] \tag{F.30}$$

and the flux

$$j = (-\gamma/2 + \sqrt{\omega_s^2 + (\gamma/2)^2})\frac{k_BT}{m\omega_s} Z^{-1}\exp[-\beta U(x_s)] \tag{F.31}$$

thus giving the Kramers formula presented in Eq. (2.65)

$$k_{A\to B} = \frac{\sqrt{\omega_s^2 + (\gamma/2)^2} - \gamma/2}{\omega_s}\frac{\omega_0}{2\pi}\exp[-\beta E_{barr}] \tag{F.32}$$

describing a rate for moderate to strong friction, that further simplifies for $\gamma >> \omega_s$ in the overdumped expression

$$k_{A\to B} = \frac{\omega_s\omega_0}{2\pi\gamma}\exp[-\beta E_{barr}]. \tag{F.33}$$

also called 'space-diffusion limited rate', as the jump happens if the friction allows the particle to join the saddle point.

F.2.4 One-dimensional TST

For a simple one dimensional system with hamiltonian $\mathcal{H}(q,p)$, the reaction coordinate x is the position q and Eq. (F.25) reads

$$k_{TST} = \frac{\int dqdp\delta(q)\dot{q}h_A\dot{q}\exp[-\beta\mathcal{H}(q,p)]}{\int_{q\in A} dqdp\exp -\beta\mathcal{H}(q,p)} \tag{F.34}$$

that becomes

$$k_{TST} = \frac{\beta^{-1}\exp\left[-\beta E_{barr}\right]}{\int_{q\in A} dqdp\exp\left[-\beta\mathcal{H}(q,p)\right]}. \tag{F.35}$$

Rewriting the denominator as the partition function Z_A on state A we have

$$k_{TST} = \frac{k_B T\exp\left[-\beta E_{barr}\right]}{Z_A} \tag{F.36}$$

and taking again an harmonic approximation for the potential around point $x_A$we recover the expression

$$k_{TST} \approx \frac{\omega_A}{2\pi}\exp\left[-\beta E_{barr}\right] \tag{F.37}$$

where $\omega_A/2\pi$ is the oscillation frequency at the bottom of state A.

F.2.5 Multidimensional TST

In order to retur now to the explicit TST expression for a canonical multidimensional system, we define the reaction coordinate $x = x(q_1,...,q_N,p_1,...,p_N)$. In this case, we consider an hypersurface S of dimension $3N-1$ passing across the saddle point. The transition state theory approximation implies that particle cross this hypersurface only once.

Averages $\langle\cdots\rangle$ in Eq. (F.25) are taken over the canonical distribution: this equation can be developed integrating explicitly over momenta in the canonical averages, obtaining first a reaction rate expression depending only on positions,

$$k_{TST} = \frac{1}{\sqrt{2\pi\beta}}\frac{\langle\delta(x)\left|\nabla_q x\right|\rangle_q}{\langle h_A(x)\rangle_q} \tag{F.38}$$

where averages over configurational degrees of freedom are indicated as

$$\langle\cdots\rangle_q = \int dq^N\cdots\exp\left[-\beta U(q_1,\ldots,q_N)\right]. \tag{F.39}$$

This rate expression can now be evaluated with a Gaussian steepest-descent approximation, and further developed up to the second order in the potential $U(q_1,\ldots,q_N)$ [17]. The normal-mode eigenvalues of the Hessian matrix of the potential, evaluated at the bottom of the reactants basin and on the saddle point and written respectively as $\left\{\omega_0^{i\,2}\right\}_{i=0,\ldots,3N}$ and

$\left\{\omega_s^{i\,2}\right\}_{i=1,\dots,3N}$. Note that eigenvalues corresponding to motions restricted to saddle hypersurface do not correspond one-to-one to frequencies in the basin. Indeed, new modes of the system at the saddle point have no counterparts with those of the basin: the transition state theory, being based on the flux over population approach (see Eq. (F.27)), requires to compute a flux of particle j across the $3N-1$ hypersurface S and a configurational integral, corresponding to c_A, in $3N$ dimension over state A. From this dimensionality difference arises the disparity in the number of vibration eigenvalues. One finally writes the well-known expression vineyard

$$k_{TST} = \frac{1}{2\pi}\frac{\prod_{i=0}^{N}\omega_0^i}{\prod_{i=1}^{N}\omega_s^i}\exp\left[-\beta E_{barr}\right] \tag{F.40}$$

and using for the partition function the *harmonic approximation* at the bottom of state A

$$Z_A \equiv \prod_{i=0}^{N}\left(\frac{k_B T}{\hbar\omega_0^i}\right) \tag{F.41}$$

and for the transition state

$$Z_s = \prod_{i=1}^{N}\left(\frac{k_B T}{\hbar\omega_s^i}\right) \tag{F.42}$$

one obtains again

$$k_{TST} = \frac{k_B T}{h}\frac{Z_s}{Z_A}\exp(-\beta E_{barr}) \tag{F.43}$$

with the prefactor $k_B T/h$ having the dimension of a frequency.

In order to rewrite the rate constant using thermodynamic functions such as the Helmholtz free energy

$$F = E - TS \tag{F.44}$$

the prefactor in Eq. (F.40) can be recasted as an entropy term,

$$\frac{1}{2\pi}\frac{\prod_{i=0}^{N}\omega_0^i}{\prod_{i=1}^{N}\omega_s^i} = \frac{k_B T}{h}\exp(\Delta S/k_B) \tag{F.45}$$

where ΔS is the entropy difference between the basin and the saddle point. This is the very same expression used in point defects migration context: indeed, replacing Eq. (F.45) in Eq. (F.40) we find

$$k_{TST} = \frac{k_B T}{h}\exp(-\beta\Delta F_{barr}) \tag{F.46}$$

where ΔF_{barr} is the free energy barrier separating states A and B.

We conclude noting that this theory applies for point defect migration in crystals (see Chapter 4), where the migration rate in the transition state theory approach is usually written as

$$k_{TST} = \Gamma_0\exp(-\beta E_{barr}) \tag{F.47}$$

with prefactor Γ_0 that reduces to the term in Eq. (F.45). The entropy difference is called migration entropy.

Appendix G

Embedded Atom Model potentials

Accurate predictions of the structure and properties of materials and their defects depend on the quality of the description of atomic interactions. The best existing approaches describing atomic interactions in condensed phases are obviously based on a quantum-mechanical approach; unfortunately, first-principles quantum-mechanical descriptions are computationally expensive and, hence, their application is usually limited to systems of a few hundred or less atoms. In addition, first-principles molecular dynamics (MD) simulation times rarely exceed a few picoseconds. As a result, most large-scale and long-time atomistic simulations are performed using empirical or semi-empirical descriptions of atomic interactions. Such descriptions of atomistic interactions represent a compromise between computational efficacy, generality and accuracy.

Empirical potentials are commonly determined by fitting a proposed functional form to available data. These data may be obtained from either experimental measurements or first-principles calculations. Commonly, the input data include such quantities for perfect crystals as lattice parameter, cohesive energy, elastic constants and unrelaxed vacancy formation energy.

The embedded atom model (EAM) potential is an approximation describing the interaction between two atoms. The potential energy is computed as a function of the separation between an atom and its neighbors, and the total potential energy in the EAM is divided into two contributions: a pairwise part and a local term,

$$U = \sum_{i \neq j} V(r_{ij}) + \sum_i F_i \sum_j \phi(r_{ij})$$

where the subscripts i and j label distinct atoms, N is the number of atoms in the system, r_{ij} is the separation between atoms i and j. The function ϕ represents the contribution to the electron charge density from atom j at the location of atom i, and function F is the embedding function that represents the energy required to place atom i into the electron cloud. For $F[x] = \sqrt{x}$ this is the second moment tight binding form of Finnis-Sinclair [98], as the electrons in this model should be tightly bound to the atom to which they belong and have limited interaction with states and potentials on surrounding atoms of the solid. As a result the wave function of the electron will be rather similar to the atomic orbital of the free atom to which it belongs.

Since the electron cloud density is a summation over many atoms, usually limited by a cutoff radius, the EAM potential is a multibody potential. For a single element system of atoms, three scalar functions must be specified: the embedding function, a pair-wise interaction, and an electron cloud contribution function.

To determine the potential proposed A04 by Ackland *et al.* [90] , two procedures were developed to fit interatomic potentials of the embedded atom method (EAM) form and applied to determine a potential which describes crystalline and liquid Iron. While both procedures use perfect crystal and crystal defect data, the first procedure also employs the first-principles (ab initio) forces in a model liquid and the second procedure uses experimental liquid structure factor data. These additional types of information were incorporated to ensure more reasonable descriptions of atomic interactions at small separations than is provided using standard approaches, such as fitting to the universal binding energy relation. This potential is in good agreement with the experimental or first-principles lattice parameter, elastic constants, point-defect energies, bcc-fcc transformation energy, liquid density, liquid structure factor, melting temperature and other properties than other existing EAM iron potentials.

The M07 potential features are described in Appendix A of [96]. It was developed following the same approach as for the A04 potential. The same analytical form was used, namely with an embedding function including a term proportional to the square of the density in addition to the square root term characteristic of tight-binding potentials in the second moment approximation, such as Finnis-Sinclair potentials [98]. Concerning ab initio data, no data from liquid iron were used, instead more configurations were considered for the vacancy formation, and migration energies were added. For the latter, values obtained from density functional theory calculations carried out with the SIESTA code using 250 atom cells were used. The ab initio values of the fcc lattice parameter as well as the fcc-bcc energy difference were also taken into account. Among the tests performed on the obtained potentials, a particular attention was paid to improve, with respect to A04, on the one hand, the thermal expansion and, on the other hand, the vacancy migration barrier, as compared to experiment/ab initio results.

Bibliography

[1] H. Risken, *The Fokker-Planck equation: Methods of Solution and Applications* (Springer, New York 1989)

[2] D. Wales, *Energy landscapes*, Springer, 2003.

[3] C. Dellago, P. Bolhuis, F. Csajka, D. Chandler, J. Chem. Phys. **108** (1998) 1964.

[4] P. Bolhuis, D. Chandler, C. Dellago, P. Geissler, Annu. Rev. Phys. Chem. **53** (2002) 291.

[5] T. Van Erp, P. Bolhuis, J. Comp. Phys. **205** (2005) 157.

[6] See, for example: M Iannuzzi, A Laio, and M Parrinello, Phys. Rev. Lett. **90**, 238302 (2003)

[7] C. Valeriani, R. Allen, M. Morelli, D. Frenkel, P. ten Wolde, J. Chem. Phys. **127** (2007) 114109.

[8] R. Allen, C. Valeriani, P. ten Wolde, J. Phys.: Condens. Matter **21** 463102.

[9] N. Mousseau, G. Barkema, Phys. Rev. E **57** (1998) 2419.

[10] R. Assaraf, M. Caffarel, A. Khelif, Phys. Rev. E **61** (2000) 4566.

[11] L. Munro, D. Wales, Phys. Rev. B **59** (1999) 3969.

[12] G. Henkelman, H. Jónsson, J. Chem. Phys. **111** (1999) 7010.

[13] J. Tailleur, S. Tănase-Nicola, J. Kurchan, J. Stat. Phys. **122** (2006) 557.

[14] S. Tănase-Nicola, J. Kurchan, J. Stat. Phys. **116** (2004) 1201.

[15] J. Tailleur, J. Kurchan, Nature Phys. **3** (2007) 203.

[16] S. Tănase-Nicola, J. Kurchan, Phys. Rev. Lett. **91** (2003) 188302.

[17] P. Hänggi, P. Talkner, M. Borkovec, Rev. Mod. Phys. **62** (1990) 251.

[18] C. Gardiner, Handbook of stochastic methods, Springer Berlin, 1985.

[19] S. Fahy, D. Hamann, Phys. Rev. B **43** (1991) 765-779.

[20] P. Del Moral, *Feynman-Kac formulae: genealogical and interacting particle systems with applications*, Springer Verlag 2004.

[21] J. Kurchan, *Six out of Equilibrium Lectures*, Oxford University Press (2006)

[22] J. Tailleur, PhD Thesis, Paris (2007)

[23] G. Adjanor, M. Athènes, F. Calvo, Eur. Phys. J. B **53** (2006) 47.

[24] M. Athènes, G. Adjanor, J. Chem. Phys. **129** (2008) 024116.

[25] W. Cochran, Sampling techniques, Wiley India Pvt. Ltd., 2007.

[26] J. Doye, M. Miller, D. Wales, J. Chem. Phys. **111** (1999) 8417.

[27] J. Doye, M. Miller, D. Wales, J. Chem. Phys. **110** (1999) 6896.

[28] A. Mossa, C. Clementi, Phys. Rev. E (2007)

[29] I. Shimada, T. Nagashima, Prog. Theor. Phys. **61** (1979) 1605.

[30] J. Neirotti, F. Calvo, D. Freeman, J. Doll, J. Chem. Phys. **112** (2000) 10340.

[31] F. Calvo, J. Neirotti, D. Freeman, J. Doll, J. Chem. Phys. **112** (2000) 10350.

[32] V. Mandelshtam, P. Frantsuzov, J. Chem. Phys. **124** (2006) 204511.

[33] T. Bogdan, D. Wales, F. Calvo, J. Chem. Phys. **124** (2006) 044102.

[34] P. Poulain, F. Calvo, R. Antoine, M. Broyer, P. Dugourd, Phys. Rev. E **73** (2006) 056704.

[35] T. Miller, C. Predescu, J. of Chem. Phys. **126** (2007) 144102.

[36] M. Athènes, M.-C.. Marinica, J. Comput. Phys. **229** (2010) 7129.

[37] D. Wales, Mol. Phys. **100** (2002) 3285.

[38] D. Wales, Mol. Phys. **102** (2004) 891.

[39] D. J. Wales, J. Chem. Phys. **124** (2006) 234110.

[40] H. D. Meyer, J. Chem. Phys. **84** (1986) 3147.

[41] S. Trygubenko, D. Wales, J. Chem. Phys. **124** (2006) 234110.

[42] C. Dellago, P. Bolhuis, D. Chandler, J. Chem. Phys. **108** (1998) 9236.

[43] P. Steinhardt, D. Nelson, M. Ronchetti, Phys. Rev. Lett. **47** (1981) 1297.

[44] P. Steinhardt, D. Nelson, M. Ronchetti, Phys. Rev.B **28** (1983) 784.

[45] L. Zhan, J. Z. Y. Chen, W. Liu, J. Chem. Phys. **127** (2007) 141101.

[46] E. Sanz , C. Valeriani, D. Frenkel, M. Dijkstra, Phys. Rev. Lett. **99** (2007) 055501.

[47] B. Peters, J. Chem. Phys. **131**, 244103 (2009).

[48] P. Geiger, C. Dellago, Chem. Phys. **375** (2010) 309.

[49] P. Grassberger, Comp. Phys. Comm. **147** (2002) 64.

[50] J.B. Anderson, J. Chem. Phys. **63** (1975) 1499.

[51] J.-F. Gouyet, *Defects and Diffusion Forum*, Paris 2001.

[52] Ott, E.,Cambridge Univ. Press (2002)

[53] M.C. Marinica, F. Willaime, N. Mousseau, N., Phys. Rev. B vol.9, **83** (2011) 094119

[54] C. Dellago, P.G. Bolhuis, P.L. Geissler, Wiley Online Library (2002)

[55] G. T. Barkema, N. Mousseau, Phys. Rev. Lett. **77** 4358 (1996)

[56] G. T. Barkema, N. Mousseau, Phys. Rev. E **57** 2419 (1998)

[57] F. Calvo, J. Chem. Phys. **108** 6861 (1998)

[58] R.J. Hinde, R.S. Berry, D.J. Wales, J. Chem. Phys. **96** 1376 (1992)

[59] R.J. Hinde, R.S. Berry, J. Chem. Phys. **99** 2942 (1993)

[60] D. Ruelle, G. Gallavotti, Thermodynamic formalism Addison-Wesley Reading (1978)

[61] Z. Sándor, B. Érdi, A. Széll, B. Funk, Celestial Mechanics and Dynamical Astronomy **90** 127 (2004)

[62] C. Lanczos Applied analysis Prentice Hall (1961)

[63] C. Dellago,P.G. Bolhuis, D. Chandler, J. Chem. Phys. **110** 6617 (1999)

[64] L.R. Pratt, J. Chem. Phys. **85** 5045 (1986)

[65] G. Benettin, L. Galgani, A. Giorgilli, J.M. Strelcyn, Meccanica **15** 9 (1980)

[66] M.R. Shirts, J.D. Chodera, J. Chem. Phys. **129** 124105 (2008)

[67] V.I. Oseledec, Trans. Moscow Math. Soc **19** 197 (1968)

[68] A.J. Lichtenberg, M.A. Lieberman, Regular and chaotic dynamics Springer Verlag (1992)

[69] C. Dellago, W.G. Hoover, H.A.Posch, Phys. Rev. E **65** 056216 (2002)

[70] D. Chandler, Introduction to modern statistical mechanics Oxford Univ. Press (1987)

[71] D. Frenkel, B. Smit, Understanding molecular simulation: from algorithms to applications Academic Press (2002)

[72] A.C.Damask, G.J. Dienes, Point defect in metals Gordon and Breach (1963)

[73] D. Wales, J. Chem. Phys. **130** 204111 (2009)

[74] G.Stoltz, J. Comp. Phys. (2007)

[75] D. Chandler, J. Chem. Phys. **68** 2959 (1978)

[76] D.D.L.Minh,J.D. Chodera, J. Chem. Phys. **131** 134110 (2009)

[77] C.H. Bennett, J. Comp. Phys. **22** 245 (1976)

[78] C. Amitrano, R.S. Berry, Phys. Rev. Lett. **68** 729 (1992)

[79] D.J. Wales, J. Chem. Phys. **130** 204111 (2009)

[80] D.J. Evans, EGD Cohen, G.P. Morriss, Phys. Rev. A **42** 5990 (1990)

[81] P. Butera, G. Caravati, Phys. Rev. A **36** 962 (1987)

[82] G. Paladin, A. Vulpiani, J. Phys. A **19** 1881 (1986)

[83] G. Benettin, L. Galgani, J.M. Strelcyn, Phys. Rev. A **14** 2338 (1976)

[84] A.N. Kolmogorov, Dokl. Acad. Nauk. **124** 754 (1959)

[85] Y.B. Pesin, Russian Mathematical Surveys **32** 55 (1977)

[86] H. D. I. Abarbanel, R. Brown, M.B. Kennel, J. Nonlinear Sci. **2** 343 (1992)

[87] G. Adjanor,M. Athènes, J.M. Rodgers, Arxiv preprint arXiv:1105.3874 (2011)

[88] M. Picciani, M. Athènes, J. Kurchan, J. Tailleur, J. Chem. Phys. **135** 034108 (2011)

[89] Athènes, M. and Marinica, M.C., J. Comp. Phys. **229** 7129 (2010)

[90] G. Ackland, M. Medelev, D. Srolovitz, S. Han, A. Barashev, J. Phys.: Condens. Matter **16** 2629 (2004)

[91] https://simtk.org/home/pymbar

[92] http://micro.stanford.edu/ caiwei

[93] M. El Makrini, B. Jourdain, T. Lelièvre, Mathematical Modelling and Numerical Analysis **41** (2) (2007) 189–213.

[94] J.F. Delmas, B. Jourdain, Arxiv preprint math/0611949 (2006)

[95] J. Kim, J. Rodgers, M. Athenes, B. smit, J. Chem. Theory Comput. (2011)

[96] L. Malerba, M.C. Marinica, N. Anento, C. Bjorkas, H. Nguyen, C. Domain, F. Djurabekova, P. Olsson, K. Nordlund, A. Serra, D. Terentyev, F. Willaime, C.S. Becquart, J. Nucl. Mat. **406** 19 (2010)

[97] M. I. Mendelev, S. Han, D. J. Srolovitz, G. J. Ackland, D. Y. Sun, M. Asta, Phil. Mag. **83** 3977 (2003)

[98] M. W. Finnis, J. E. Sinclair, Phil. Mag. A **50** 45 (1984)

[99] S. Kumar, D. Bouzida, R. H. Swendsen, P. A. Kollman, J. M. Rosenberg, J. Comp. Chem. **13** 1011 (1992)

[100] Z. Tan, J. Am. Stat. Assoc. **99** 1027 (2004)

[101] C.C. Fu, J. Dalla Torre, F. Willaime, A. Barbu, J.L. Bocquet, Nature Mat. (2005)

[102] J. R. Beeler, R. A. Johnson, Phys. Rev. **156** 677-684 (1967)

[103] A. Vehanen, P. Hautojarvi, J. Johansson, J. Yli-Kauppila, P. Moser, Phys. Rev. B **25** 762 (1982)

[104] G. S. Was, *Fundamentals of Radiation Materials Science - Metals and alloys* Springer (2007)

[105] G. Lucas, R. Schäublin, Nucl. Instr. and Methods in Phys. Research B **267** 3009-3012 (2009)

[106] A. Seeger, Phys. Stat. Sol. (a) **167** 289 (1998)

[107] G.H. Vineyard, J. Phys. Chem. Sol. **3** 121 (1957)

[108] A. Da Fano, G. Jacucci, Phys. Rev. Lett. **39** 950 (1977)

[109] C.P. Flynn, *Point Defects and Diffusion*, Clarendon Press, Oxford (1976)

[110] J.L. Bocquet, G. Brebec, Y. Limoge, Diffusion in metals and alloys, in *Physical Metallurgy*, North Holland (1996)

[111] S. Takaki, J. Fuss, H. Kugler, U. Dedek, H. Schultz, Radiat. Eff. **79**, 87-122 (1983).